Title
Cone-Jet and Emission Behavior for Electrospray Thrusters via Computational Analysis

Author
Huh, Henry

Publication Date
2023

Peer reviewed|Thesis/dissertation

UNIVERSITY OF CALIFORNIA
Los Angeles

Cone-Jet and Emission Behavior for Electrospray Thrusters via Computational Analysis

A dissertation submitted in partial satisfaction
of the requirements for the degree
Doctor of Philosophy in Mechanical Engineering

by

Henry Huh

2023

ABSTRACT OF THE DISSERTATION

Cone-Jet and Emission Behavior for Electrospray Thrusters
via Computational Analysis

by

Henry Huh
Doctor of Philosophy in Mechanical Engineering
University of California, Los Angeles, 2023
Professor Richard E. Wirz, Chair

Electrospray (ES) thrusters currently require significant life and performance improvements. To address this challenge, this dissertation uses two-dimensional axisymmetric (2D) and three-dimensional (3D) simulations to investigate the critical physics of low to high-conductivity cone-jet and droplet formation of ES thrusters to provide detailed descriptions of electrospray cone, jet, droplet, and ion formation for life and performance modeling. The leaky-dielectric model is incorporated in the Finite Volume Method (FVM) code, OpenFOAM, to investigate the electrospray emission behavior of low to high-conductivity liquids. This work extends FVM modeling to high conductivities by employing a new interface interpolation scheme devised in the Volume of Fluid (VOF) method to ensure charge conservation for accurate reproduction of charge accumulation and the resulting meniscus shape in the cone-to-jet region and jet breakup.

The 2D modeling results agree well with experiments and scaling laws for droplet diameter and total current for low and moderate conductivity fluids, i.e., heptane and tributyl phosphate (TBP), respectively. The droplet diameter is shown to increase as the dimensionless flow rate increases or the electric Reynolds number decreases. Results are consistent with a parametric investigation

of the meniscus shape, the maximum charge density for key operating conditions (flow rate and extraction potential), and liquid properties (conductivity, surface tension, viscosity, and relative permittivity). These results show that the new interface interpolation scheme provides accurate results for a wide range of conductivities, fluid properties, and operating conditions. The results also provide valuable physical insights for varying liquid conductivity in the electrospray emission process. In particular, a low dimensionless flow rate or high electric Reynolds number leads to the emergence of convex-outward menisci associated with high charge density in the cone-to-jet region, resulting in high jetting velocity and high specific charge droplets.

The propellant temperature can significantly impact the cone-jet droplet emission and ionization process in the droplet breakup and transition region. The energy equation is employed for the governing equation of the finite volume model to accurately predict the energy of the charged droplets over a range of relevant operating conditions. The new interface interpolation scheme devised for the Volume of Fluid (VOF) method is implemented to ensure energy conservation for accurate temperature prediction due to Joule dissipation, i.e., Ohmic heating and viscous dissipation. Increasing temperature is observed after the cone-to-jet region, which is the region where internal and outer electric fields at the liquid surface are highest along the jet. Ohmic dissipation tends to reduce with increasing electrical permittivity where high charge relaxation impedes the electric field.

To investigate steady tilted cone-jet emission, the 2D leaky dielectric EHD model is extended to a 3D EHD model. Modeling results agree well with experiments and scaling laws for jet diameters with respect to electrical Bond numbers. The results from the model show that the tilted cone-jet results from the asymmetric tangential electrostatic forces at the dilated surface with a higher radius of curvature of the tilted cone above the critical electrical Bond number. Increasing electrical permittivity leads to a lower critical electrical Bond number tilting the cone, though a higher charge relaxation results in a larger jet radius.

The dissertation of Henry Huh is approved.

David Bilyeu

Kunihiko Taira

Tim S. Fisher

Jeff D. Eldredge

Richard E. Wirz, Committee Chair

University of California, Los Angeles

2023

To my family, for their unconditional love and support

TABLE OF CONTENTS

List of Figures

List of Tables

ACKNOWLEDGMENTS

I would first like to thank my advisor Prof.Richard Wirz for providing me with valuable guidance and opportunities to succeed throughout my years at UCLA. I can never forget your words of encouragement when I was overly nervous about my first long talk. You have not only taught and trained me academically but also have helped me become proficient in delivering my ideas and results, which I know would greatly benefit me as a researcher.

I am honored and grateful to have Prof.Eldredge, Prof.Fisher, Prof.Taira, and Dr.Bilyeu as my committee members. It is one of my greatest fortunes to have attended a university with such supportive and respectable faculty. Thank you all for your insightful feedback and support. Throughout my future endeavors as an aerospace engineer, I will not forget the lessons I learned from you.

I owe a great deal of gratitude to John Ziemer and Colleen Marrese-Reading at NASA JPL for their mentorship. I am privileged to have participated in the LISA project. Learning the fundamentals of EP and sharing my findings with the group made my grad school years truly enjoyable and inspiring. I am deeply indebted to David Bilyeu and Dan Eckhardt for their years of invaluable guidance. Without your support, I would not have been able to reach this milestone in my career as an aerospace engineer. I deeply thank Samuel Jun Araki and Cesar Huerta for your enlightening discussions on EP modeling. The time I spent at AFRL in 2019 was an amazing experience, and I look forward to our next journey.

I am grateful to the Plasma & Space Propulsion Lab members. I greatly owe Adam Collins for his academic guidance and mental support. You would give me the knowledgeable and warm advice I needed whenever I had difficulties, either research-wise or personally. This endeavor would not have been possible without my colleagues, Gary Li, Stephen Samples, Ani Thuppul, Nolan Uchizono, Peter Wright, McKenna Davis-Breddan, Angelica Ottaviano, Mary Konopliv, Nicolas Rongione, Shehan Parmar, Patrick Crandall, Graeme Sabiston, and Gary Wan, for our glorious days in the lab and cubicles. Words cannot express my gratitude to you guys, so thank

you all in my heart. I can't forget our most memorable times at many conferences. Especially in Vienna, they were the most special days and nights preparing our first talks at Airbnb. Thank you all for the in-depth discussions during the meetings, for putting up with me, and for giving me the best support during our time at UCLA.

My sincerest gratitude goes to Grace Chung, who has been my utmost supporter. Thank you for putting up with my rants when my model did not work properly, feeding me while I wrote papers, and rejoicing with me over my accomplishments. Hopefully, our next chapter would be slightly better than how they were in the last few years. Also, I am beyond grateful to the Chung family for your love and emotional support. I am thankful that I always feel at home with your warm welcome and thoughtful care.

For the last, I dedicate this work to my family, who have been my greatest and lifelong supporters. I would not be here without your unconditional love and inspiration. My father, Kangyul Huh, Just a sentence is enough, I am so proud to be your son. My mother, Yangsun Cho, I was able to do this because of you, and thank you for all your support and sacrifice in every stage of my life. Love you, Mom. My brother, Sungchul Huh, you are a third parent to me. I deeply thank you for your support and love. My sister-in-law, Sungeun Lee, I greatly appreciate your emotional support. My lovely two-year-old nephew Junwoo Huh, I am sure you will become a great aerospace scientist one day with that NASA onesies I brought from JPL. Keep up your good work, eating and playing. Love you all.

The research conducted in this dissertation was supported by a grant from NASA's Jet Propulsion Laboratory, California Institute of Technology to support the LISA CMT development plan (NASA/JPL Award No. 1580267), the Air Force Research Lab at Edwards AFB, CA (Award No. 16-EPA-RQ-09), and Air Force Office of Scientific Research (AFOSR) (Award No. FA9550-21-1-0067).

VITA

2009 - 2015 B.S. in Mechanical Engineering, Sogang University.

2014 - 2015 Research Intern, Computer-Aided Engineering Team, Samsung Advanced Institute of Technology.

2015 - 2016 Research Intern, Combustion Laboratory, Pohang University of Science and Technology.

2017 - 2017 Teaching Assistant, MAE 166C Design of Composite Materials, UCLA.

2017 M.S. in Mechanical Engineering, UCLA.

2018 - 2021 Teaching Assistant, MAE 250C Compressible Flow, UCLA.

2019 - 2020 Computational Scientist, DOD High-Performance Computing Internship Program, Air Force Research Laboratory, Edwards Air Force Base.

2019 - 2021 Teaching Assistant, MAE 161B Introduction To Space Technology, UCLA.

2018 - 2023 Ph.D. student in Mechanical and Aerospace Engineering, Plasma and Space Propulsion Laboratory, UCLA.

PUBLICATIONS

Simulation of electrospray emission processes for low to moderate conductivity liquids. Henry Huh and R. E. Wirz, Physics of Fluids (2022)

Numerical simulation of cone-jet and emission processes for electrospray thrusters. Henry Huh and R.E. Wirz, Proceedings of the 37th International Electric Propulsion Conference, MA, USA, (2022)

Three-dimensional microscopy and analysis of the emission cone meniscus for electrospray thrusters. A. L. Collins, N. M. Uchizono, Henry Huh, and R. E. Wirz, Proceedings of the 37th International Electric Propulsion Conference, MA, USA, (2022)

Electrohydrodynamic simulation of electrospray thruster extraction. Henry Huh and R.E. Wirz, AIAA SciTech 2022 Forum, (2022)

Simulation of electrospray thruster emission processes for highly conductive liquids. Henry Huh and R.E. Wirz, Proceedings of the 36th International Electric Propulsion Conference, Austria, (2021)

A novel variable mode emitter for electrospray thrusters. Peter L. Wright and Henry Huh, Proceedings of the 36th International Electric Propulsion Conference, Austria, (2019)

Numerical simulation of electrospray extraction for highly conductive propellants Henry Huh and R.E. Wirz, Proceedings of the 36th International Electric Propulsion Conference, Austria, (2019)

(In prep.) Asymmetric Tilted Cone-Jet Emission Analysis via Simulation. Henry Huh and R.E. Wirz (2023)

(In prep.) Temperature and the Joule heating effect on electrospray performances for high conductivity liquid. Henry Huh and R.E. Wirz (2023)

CHAPTER 1

Introduction and Motivation

1.1 Electric Propulsion (EP)

The number of NanoSat and CubeSat launches has rapidly increased over the past decade, reaching more than 2000 as of 2023[1] in Figure 1.1. CubeSat's small and standardized platform can help reduce the costs of technical developments and scientific investigations. The propulsion systems used on CubeSats usually provide a thrust of up to 1 mN, with the consumed power of up to 100 W and the unit mass of several kg[25]. Since 2013, the flight heritage for small spacecraft has increased by over 30% and has become the primary source to space access for commercial, government, private, and academic institutions. The total number of spacecraft launched in the past ten years is 5681, and 45% of those had a mass less than 200 kg. In 2021, among the total 1849 spacecraft launched, 94% were small spacecraft with an overall mass under 600 kg, and 40% were under 200 kg, and 11% were NanoSats[26]. Cubesat was first developed by California Polytechnic State University (Cal Poly) and Stanford University designed for space exploration and research for academic purposes in 1999. The lowered barrier to entry has significantly increased access to space, leading to an exponential growth in the popularity of CubeSats since its inception. Although CubeSats or NanoSats are not capable of orbit transition or deep space missions due to their limited weight and volume, they can provide an order of greater total impulse than chemical systems. High total impulse and low thrust requirements, such as station keeping, are of significant interest for electric propulsion applications. Recently, the "ChipSat" concept was proposed with the aim of exploring near-Earth orbit using extremely miniaturized spacecraft such as Pico- or Femtosatellite[27] (~ 0.1 kg) in Figure 1.2.

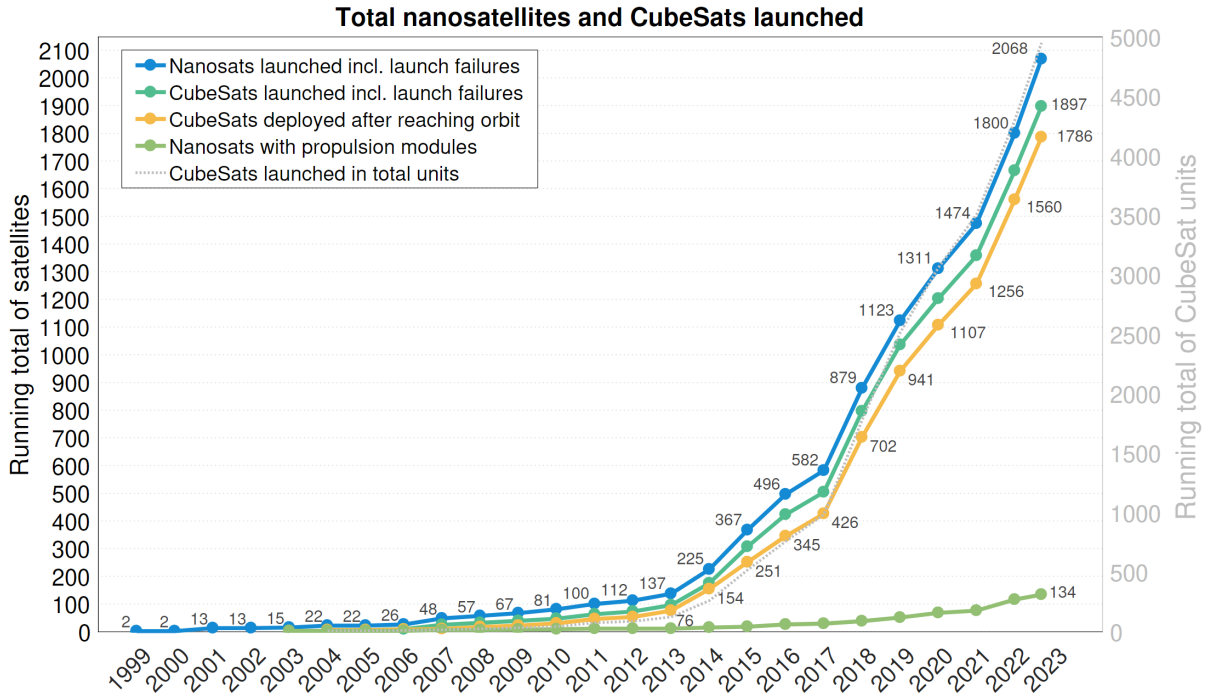

Figure 1.1: Total nanosatellites and cubesatellites launched[1].

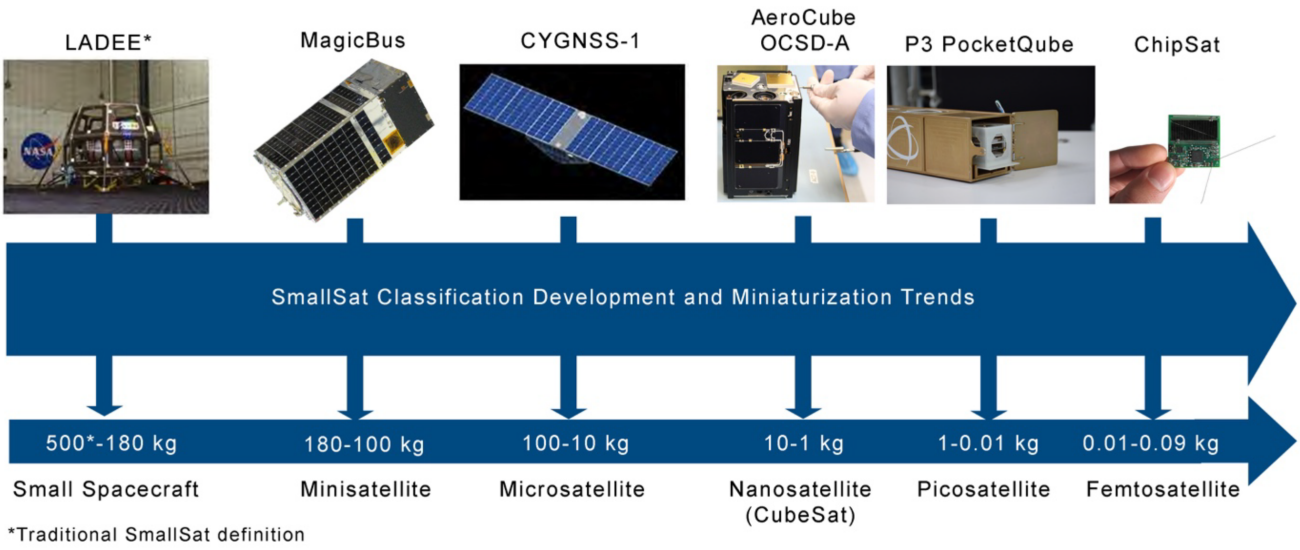

Figure 1.2: Overview of small spacecraft categories. Figure credit from NASA, SpaceX, Redwire Space, and Alba Orbital[2].

The very first to imagine the acceleration of charged particles for propulsion was Tsiolkovsky and Goddard. Rocket equation was derived by Tisolkovsky, and Goddard patented the first electrostatic ion accelerator for propulsion. According to Jahn's definition of EP as 'the acceleration of gases for propulsion by electrical heating and/or by electric and magnetic body forces'[28], EP technologies can be broadly classified as electrothermal, electrostatic, and electromagnetic propulsion. Electrothermal propulsion uses the thermal expansion of the hot neutral or ionized gases going through the nozzle to convert the heat energy into kinetic energy. Electrothermal thrusters feature a relatively low specific impulse, although they are the simplest systems among EP devices. Electrostatic propulsion uses the ionized propellant that is accelerated by the electric field applied by the electrodes. For example, gridded ion thrusters ionize the propellant in a magnetized chamber and accelerate by high voltage grids to provide thrust. Hall thrusters ionize the propellant in the annular channel and accelerate by crossed electric and magnetic fields where the magnetic field is high enough to confine electrons and low enough to avoid affecting the ion trajectories. For electromagnetic propulsion such as magnetoplasmadynamic (MPD) thruster, the propellant is accelerated in the form of quasi-neutral plasma where the thrusters are not limited to space charge.

Various EP systems are shown in Figure 1.3 with thrust-to-power ratio as a function of specific impulse. The lines define the thruster efficiency in Eqs. 2.8. The high thrust-to-mass ratio allows faster transfer time and is important for time-critical missions and high specific impulse for high mass efficiency. Typical EP systems provide $\sim 50\,\%$ of thrust efficiency. The future of electric propulsion thrusters includes several research areas[29]: (1) Higher thrust efficiency produced by higher-power, expanded lifetime thrusters to support manned missions or cargo missions to celestial objects. It requires developing high-power ion, hall thrusters, or magnetoplasmadynamic thrusters to provide high power and high specific impulse. (2) High precision in controlling the thrust with low noise for highly sensitive space astronomical observatories and fine satellite controls within constellations. (3) Highly compact EP thrusters for small satellites to achieve active maneuvering or orbital changes. (4) Alternative power sources, such as nuclear fusion energy. This study focuses on the electrospray thrusters (colloid/FEEP) that are advantageous for precise

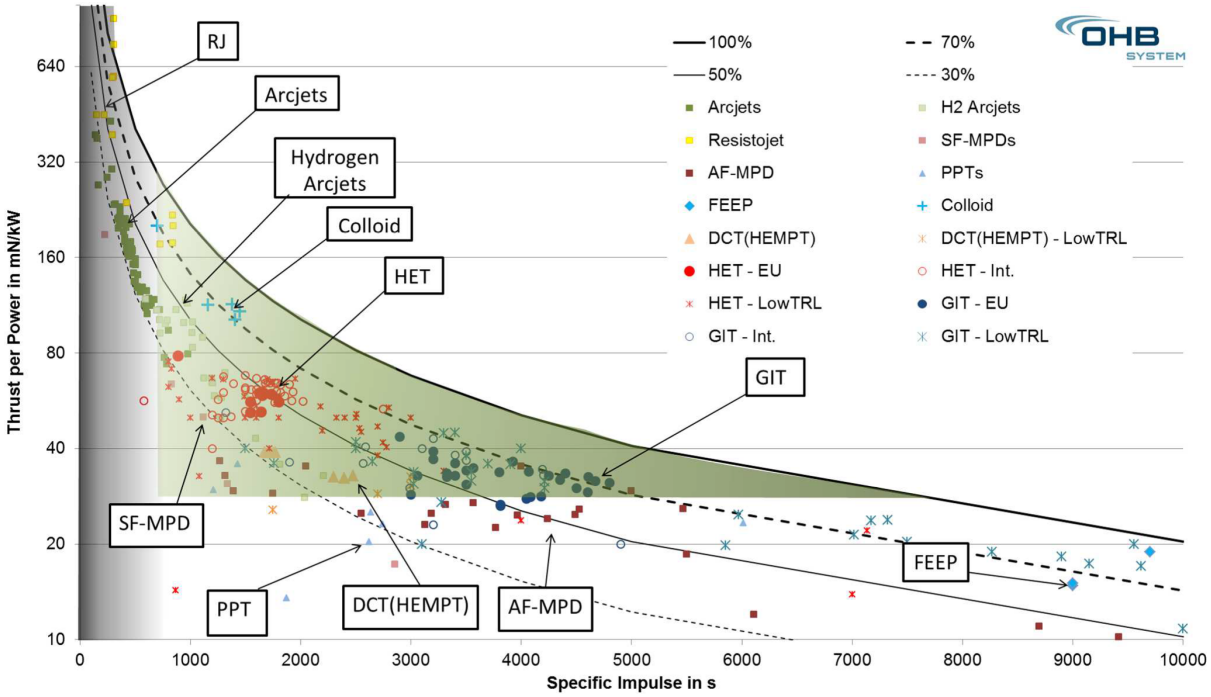

Figure 1.3: Thrust-to-power ratio with respect to the specific impulse for various EP systems. The green area describes the required performance for station keeping. Figure credit from OHB system[3].

attitude, orbit control, thermal stability, and efficient propulsion systems. Compared to the other EP systems, the ability to miniaturize the propulsion system can assist in improving efficiency due to their low mass. Although electrospray thruster exhibits low thrust levels of several μN, miniaturized spacecraft can achieve future missions such as de-orbiting, orbit maintenance, and attitude control.

1.2 Electrospray Thrusters

Electrospray thrusters can achieve high thrust precision and a wide range of specific impulse ranges, the thrust range of 10 μN to 1 mN and the specific impulse of 225 s to 5000 s. The electrospray thrusters are categorized into two specific applications according to the propellant used. Ionic Liquid Ion Source (ILIS) or colloid thruster breaks the propellant into tiny charged droplets that

use ionic liquids as the propellant, such as 1-ethyl-3-methylimidazolium tetrafluoroborate (EMI-BF4) and bis(trifluoromethyl sulfonyl)imide (EMI-Im). Ionic liquids are possible candidates for ILIS not only due to their ionic nature but also their negligible vapor pressure and high electrical conductivity[30]. On the other hand, Field Emission Electric Propulsion (FEEP) commonly uses low melting point liquid metals as the propellant, such as indium and cesium, and typically emit ions that offer high thrust precision but low thruster forces. The colloidal engines work with efficiency of 65% with high specific impulse range of around 1000 s that operate with voltages of 15 to 25 kV. Higher specific impulse implies less propellant required to complete a certain mission, further contributing to the suitability of electrospray thrusters as propulsion systems for CubeSats and other small satellite missions where available mass and volume are significantly restricted. The system is perfectly suitable for micro-propulsion that requires high ΔV at a decent thrust-to-power ratio in Figure 1.3. Furthermore, electrospray thrusters can operate in either droplet or ion mode, where they show moderate or high specific impulses, respectively[11]. Electrospray in the purely-ionic regime (PIR) has a potential for high efficiency and specific impulse with minimal mass and power requirement, but the investigation is limited due to manufacturing such as laser ablation or multi-step electrochemical etching[31]. On the other hand, a high thrust-to-power ratio can be achieved in exchange for the low specific impulse by operating in the droplet mode. The droplet mode thrusters are the most mature systems, given the success of the LISA Pathfinder mission[15, 16]. The thrusters successfully demonstrated 3478 h of test flight establishing pointing capabilities and thrust-precision using EMI-Im but encountered one of the emitters failed before reaching 2500 h[16]. The primary mechanism that limited the lifetime of the operation of electrospray droplet modes was overspray, which leads to mass flux impingement on the extraction and acceleration grids, resulting in shorting and power processing unit (PPU) failure[14]. When operated in ion mode, operational thruster modes, and jet instabilities can result in droplet emission during ion mode that degrades the specific impulse and thrust efficiency.

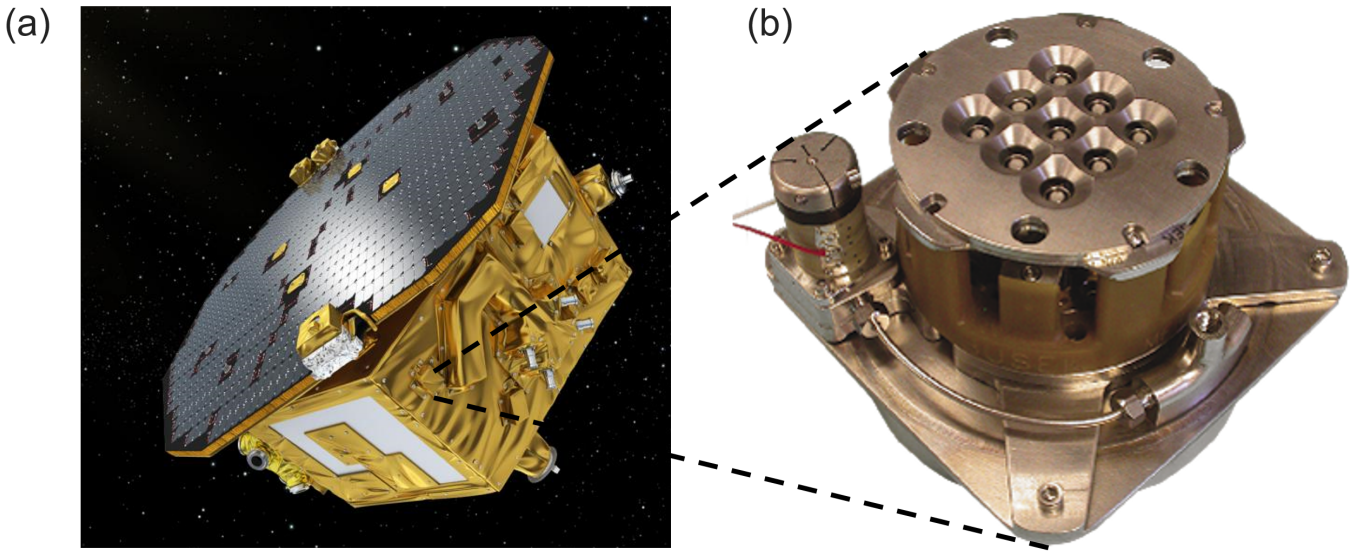

Figure 1.4: (a) LISA Pathfinder Space Mission and (b) BUSEK Colloid Micronewton Thruster (CMNT). Figure credit from ESA (European Space Agency) and BUSEK.inc.

1.3 The Leaky Dielectric Model

Formation of a conical shape from a sessile drop in the vicinity of a charged rod was the first experiment to observe the EHD behavior[32]. A conical meniscus was developed by surface tension and electrostatic forces balanced on the interface in the cone-jet mode. Zeleny (1914) first observed different modes of electrosprays, including the steady cone-jet mode, which has been of significant interest for the stable emission of droplets [33]. Cloupeau & Prunet-Foch (1994) examined various cone-jet structures and operating modes in a range of operating conditions and physical properties of low to moderate conductivity liquids[34] ($2 \times 10^{-8}\,\mathrm{S\,m^{-1}}$ to $1 \times 10^{-4}\,\mathrm{S\,m^{-1}}$). Taylor (1964) applied electrostatic analysis for perfectly conductive liquid up to the location where a jet begins to develop from the cone[32]; the half cone-angle at the apex was shown to be 49.3°.

The Ohmic, leaky-dielectric model of Melcher & Taylor supplements Taylor's analysis by introducing tangential electrostatic force due to free charge accumulated on the liquid surface, unlike in perfect conductors and dielectrics involving only perpendicular electrical stress[35]. For a perfect conductor, infinite conductivity causes the free charge to redistribute until the electric field

in the conductor becomes zero. High enough conductivity involves Ohmic conduction as the only agent causing charge transport. In this limit, the free charge migrates instantaneously from bulk liquid to the interface screening the electric field completely from the interior of the liquid. The equipotential interface results in negligible tangential stress with almost no electric polarization. Similarly, perfect dielectrics are free of charge at the interface with no ions or free electrons in the bulk fluid where polarization effects remain. If the polarization effects are homogeneous, electrical forces appear only at the liquid surface, where unbalanced dipoles result in the normal stress component. Apolar liquids such as benzene are considered dielectric fluids, whereas most liquids involve impurities dissolved to create ionic pairs and may hardly be considered as perfect dielectric fluid. The fluids must be considered as conducting fluid to some extent.

Important scaling relationships have been developed to correlate the output parameters of interest under different assumptions[6, 36, 8]. Although they provide valuable physical insight, the scaling laws cannot describe the physical mechanism during evolution of a cone-jet and subsequent droplet breakup. Several numerical models have been developed to describe the process of cone-jet formation and electrospray emission. The boundary element/integral method (BEM) is computationally cost-efficient and allows accurate analysis under the given constraints[37, 38, 39]. Higuera investigated the surface charge density with varying flow rates and permittivities with far-field boundary conditions given from electrostatic solution[32] in the restricted cone-to-jet region[38]. Herrada and Montanero applied the Newton-Raphson method to solve the nonlinear discrete equations and observed nonlinear dynamics of a liquid bridge at the minimum volume stability limit[40]. Ponce-Torres *et al.* applied the boundary fitted method to calculate the base flow and the corresponding eigenmodes to determine linear global modes of the system[41]. Gamero-Castaño & Magnani went further to obtain a solution in an extended cone-to-jet region[39], concluding the surface position of TBP largely invariant to physical properties and flow rates for dielectric constants of 8.91 and 64.9. The current Boundary Element/Fitted Methods cannot make predictions of emitted droplets or internal flow in bulk liquid, which are important observable parameters in electric propulsion.

The Finite Volume Method (FVM) allows robust handling of nonlinear conservation equations as a more flexible approach than the BEM. The FVM can reproduce not only the cone-jet structure but also downstream breakup and emitted droplets in an electrospray[42, 43]. Several EHD models have been developed on the basis of the FVM. L′opez-Herrera *et al.* and Herrada *et al.* used the Volume-of-Fluid method to track interface in a multiphase problem by Gerris[44, 45, 46]. Roghair *et al.* developed an EHD solver in OpenFOAM based on the work of L′opez-Herrera *et al.*, which was extended by Dastourani *et al.* for electrosprays of low conductivity ($\sim 1 \times 10^{-8}\,\mathrm{S\,m^{-1}}$ to $\sim 1 \times 10^{-6}\,\mathrm{S\,m^{-1}}$) liquid[42, 44, 43]. Complex emitter geometry such as porous emitter was effectively modeled by the CVFEM (Control Volume Finite Element Method) for high conductivity liquid where self-heating can be significant[47, 48, 49]. More recently, Guan *et al.* applied OpenFOAM for modeling pulsating electrospray emission with no droplet breakup in a steady cone-jet mode at low electric Bond numbers.

1.4 Research Motivation

Electrospray thrusters were first operated in space in 2015 as a technology demonstration of the Colloid MicroNewton Thrusters (CMNTs), developed by Busek Co., Inc and NASA Jet Propulsion Laboratory (JPL) for the European Space Agency (ESA) Laser Interferometer Space Antenna (LISA) Pathfinder mission in Figure 3.5. The CMNTs demonstrated key mission capabilities such as micro-newton thrust precision and low thrust noise. Seven of the eight CMNTs operated in space for over 2,400 hours, and a ground-based test ended after 3,400 hours without failure[15, 16]. The LISA mission requires nearly 40,000 hours of an operational lifetime and 60,000 hours for the extended mission. Therefore, understanding life-limiting mechanisms in electrospray thrusters is crucial to improve their viability for LISA and other future missions. The LISA Colloid Microthruster Technology (CMT) development plan, described by Ziemer et al., uses lessons learned, trade studies, and physics-based modeling to predict the performance and lifetime of the LISA CMT and guide system design[50, 15, 4].

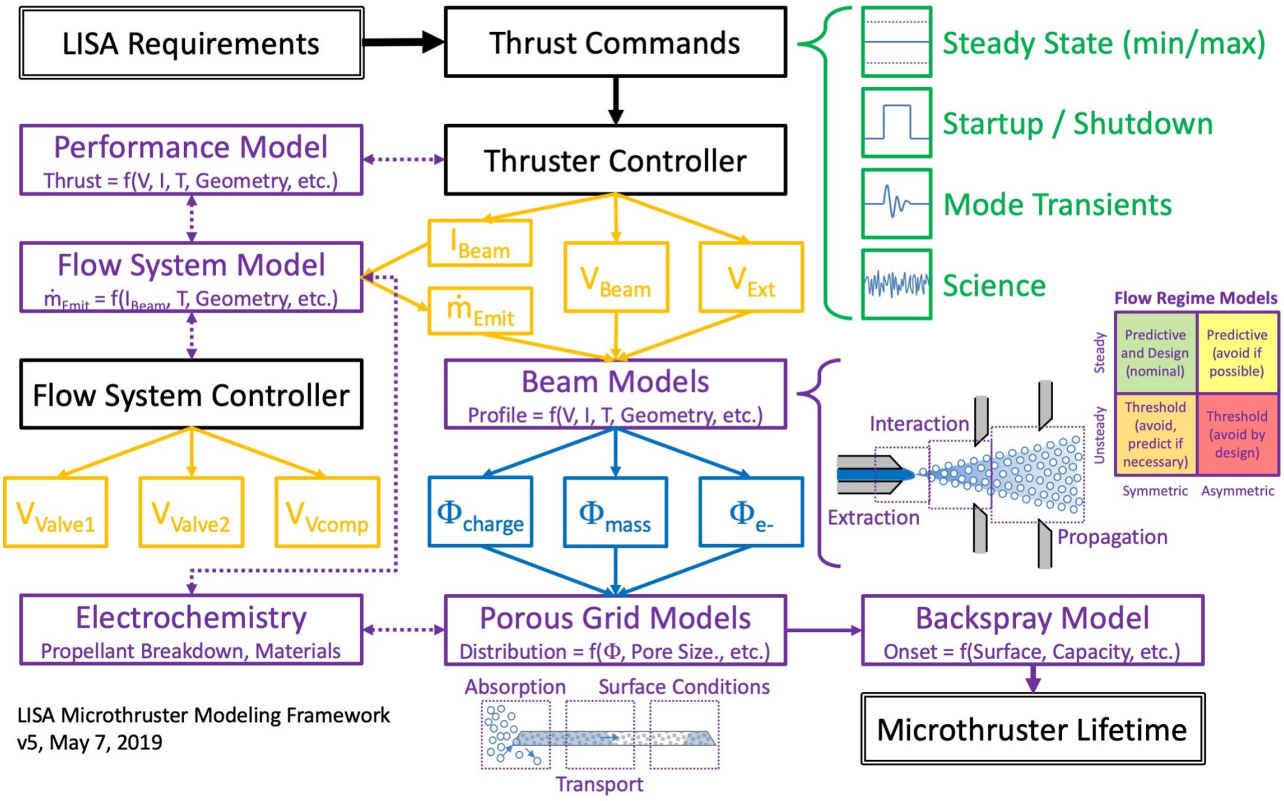

Figure 1.5: Development Plan for LISA CMT[4].

As part of the Beam Models in Figure 1.5, the extraction region takes into account the electrohydrodynamics physics where a potential difference of hundreds to several thousand volts is typically applied between the emitter and the extraction electrode, producing a cone-shaped meniscus that can lead to a liquid jet, droplets, and ions in the operation of an electrospray. In recent decades, considerable study has been undertaken to understand the underlying physics of electrohydrodynamics (EHD) in an electrospray. Computational modeling is essential to understand the electrospray emission and plume evolution for steady and transient operating conditions. It is necessary to develop modeling capabilities that resolve unsteady and time-dependent effects to capture the life-limiting effects such as grid impingement.

Modeling of extraction regions in electrospray devices has been widely investigated. Taylor, Melcher, and Saville first developed the leaky dielectric model, where the tangential stress plays an

important role, unlike in the perfect dielectric and perfect-conductive models[32, 35, 51]. Lastow *et al.* employed commercial CFD software (ANSYS-CFX) to simulate the leaky dielectric model with Laplace's equation[52]. Lopez-Herrera *et al.* developed an EHD solver with the Volume of Fluid method in Gerris[44]. In the present study, the open-source CFD tool, OpenFOAM, is used. There are several advantages of OpenFOAM over other commercial software for electrospray modeling. Due to the complexity of two-phase fluid flow coupled with electrostatic effects, it was difficult to model the complete physics with commercial software. Access to the source code in OpenFOAM enables direct implementation of the governing equations best fit for EHD modeling of electrospray emitters. The perfect dielectric and conductive models have no tangential electric stress acting on the liquid interface. Consequently, cone-jet formation and droplet breakup were not observed. The leaky dielectric model was able to capture cone-jet formation but no droplet breakup. The presented EHD code uses the full charge conservation equation with no other simplification, allowing it to capture not only cone-jet formation but also droplet breakup. This is possible due to the consideration of both conduction and convection of electric charges. Furthermore, this model allows us to capture instabilities and unsteady behavior during extraction.

1.5 Dissertation Overview

The objective of this study is to develop a high-fidelity EHD model that can provide a detailed emission mechanism for electrospray devices in a wide range of operating conditions and fluid properties. A new interface interpolation scheme is developed and shown to suppress charge loss effectively and to simulate jet breakup, thus extending the modeling capabilities up to moderate ($\sim 10^{-4}\,\mathrm{S\,m^{-1}}$) and high ($\sim 10^{-2}\,\mathrm{S\,m^{-1}}$) conductivity while still providing accurate results for lower conductivity ($\sim 10^{-7}\,\mathrm{S\,m^{-1}}$). We will validate the suggested models against experimental observation and scaling relationships. In particular, we applied the model across operating conditions and fluid properties critical in defining the steady cone-jet mode. We will show how the charge distribution varies along the interface and how the competing electrostatic and surface ten-

sion forces on the interface determine the meniscus shape. The energy equation is implemented to investigate the temperature analysis and joule heating or Ohmic heating effect, specifically at the cone-to-jet region where the charge relaxation effects govern the most on emission behavior. The newly developed interface interpolation scheme is applied to the thermal conductivity to suppress energy loss and conserve the temperature at the liquid boundary. We will perform a sensitivity analysis with respect to the relative electrical permittivity to reduce the Joule heating effect. The two-dimensional axisymmetric EHD model will be extended to a three-dimensional model to study the tilted-cone jet emission behaviors. We will validate the extended model against experimental observations and scaling relationships. The Electric Bond number sensitivity study will show how the cone tilt phenomenon occurs at the cone-to-jet region and how nonuniformly distributed charges affect the cone meniscus. Electrical permittivity is varied to show how the charge and electric field at the meniscus change. Whipping emissions and the toroidal motion of the horizontal cross-section further downstream of the jet will be discussed. The theoretical background is provided in Section 2 and the model formulations in Section 3. The modeling results for axisymmetric cone jet emissions at various conductivities are provided in Section 4. Energy analysis and Joule heating effects are in Section 5, and asymmetric tilted-cone jet emission is in Section 6. The concluding remarks are provided in Section 7.

CHAPTER 2

Theoretical Background

2.1 Electric Propulsion (EP)

The rocket equation describes the relationship between the spacecraft's velocity and the mass of the system given as

$$T = -\frac{d}{dt}\left(m_p \boldsymbol{v}_{ex}\right) = -\dot{m}_p \boldsymbol{v}_{ex} = M\frac{d\boldsymbol{v}}{dt}, \tag{2.1}$$

where the thrust of the spacecraft equals the time rate of change of the momentum of the propellant. T, M, $\boldsymbol{v}$, m_p, and $\boldsymbol{v_e}$ denote the thrust, mass, velocity of the vehicle, propellant mass, and exhaust velocity of the propellant relative to the vehicle. Note the time rate of the changes of the total mass equals that of the propellant, and the total mass, M, is the sum of dry mass, m_d. Integrating the motion in a straight line from the initial velocity, v_i, to the final velocity, v_f gives

$$\Delta v = v_f - v_i = v_e \ln\left(\frac{M}{m_f}\right) = v_{ex} \ln\left(1 + \frac{m_p}{m_f}\right), \tag{2.2}$$

assuming the exhaust velocity, v_{ex}, is constant. M, and m_f refer to the initial, final mass. The final mass of a spacecraft delivered after a given amount of propellant has been used to achieve the specified $\Delta\boldsymbol{v}$ is

$$m_d = (m_d + m_p)\exp\left(\frac{-\Delta v}{v_{ex}}\right). \tag{2.3}$$

The total impulse $\boldsymbol{I}$ is defined as the time integral of the force, $\boldsymbol{F}(t)$, delivered by a thruster during the operational time interval, t_p, given as

$$\boldsymbol{I} = \int_0^{t_p} \boldsymbol{F}(t)\, dt = \int_0^{t_p} \dot{m}_p \boldsymbol{v}_{ex} dt = m_p \boldsymbol{v}_{ex}, \tag{2.4}$$

where the total impulse measures the change in momentum of the spacecraft. The specific impulse is a measure of thrust efficiency and is defined as the ratio of thrust to the rate of propellant consumption. Specific impulse, I_{sp}, for constant thrust, T, and propellant flow rate is given as

$$I_{sp} = \frac{T}{\dot{m}_p g} = \frac{v_{ex}}{g}. \tag{2.5}$$

The change in velocity of the spacecraft is then

$$\Delta v = (I_{sp} g) \ln\left(\frac{m_d + m_p}{m_d}\right) \tag{2.6}$$

where g is the gravity acceleration at sea level.

The utilization efficiency, η_m, is the proportion of emitted ions to the amount of propellant admitted, $\dot{m}_p$, as the thrust is mainly generated by the number of exhausted ions, $\dot{m}_i$,

$$\eta_m = \frac{\dot{m}_i}{\dot{m}_p}, \tag{2.7}$$

describes the fraction of the input propellant mass that is converted into ions and accelerated in the electric propulsion.

The electrical efficiency is defined as the beam power, P_b, to the total input power, P_T, ratio given as

$$\eta_e = \frac{P_b}{P_T}. \tag{2.8}$$

The total efficiency of an electrically powered thruster is defined as the jet power, P_{jet}, divided by the total electrical power, P_{in}, of the thruster as

$$\eta_T = \frac{P_{jet}}{P_{in}} = \frac{T^2}{2\dot{m}_p P_{in}}, \tag{2.9}$$

where the kinetic thrust power beam, i.e., jet power, is defined as $P_{jet} = \frac{1}{2}\dot{m}_p v_{ex}^2$. The total efficiency can be calculated with the measurements of the input electrical power, input mass flow rate, and thrust.

2.2 Electrohydrodynamics (EHD)

2.2.1 Leaky Dielectric Model

Gauss's law is given for perfect conductors, and perfect dielectrics as,

$$\nabla \cdot (\varepsilon E) = 0, \tag{2.10}$$

where ε and E denote electrical permittivity and electric field. The charge density is zero due to instantaneous charge migration. This leads to the charge conservation equation given as

$$\nabla \cdot (\sigma E) = 0, \tag{2.11}$$

where σ is electrical conductivity. The electrostatic force is given as

$$F_E = -\frac{1}{2} E^2 \nabla \varepsilon. \tag{2.12}$$

The governing equations for perfect conductors and perfect dielectrics are identical, as they share the same physics. Leaky dielectrics, on the other hand, show different EHD characteristics. In practice, all materials have some conductivity at the poorly conducting interface that exhibits

the characteristics of both perfect conductors and perfect dielectrics. Finite conductivity enables electrical charge accumulation at the droplet interface, allowing the tangential electric stress, which sets the fluid in motion until the viscous stress balances.

Gauss's law for leaky-dielectrics reads as,

$$\nabla \cdot (\varepsilon E) = \rho_E. \tag{2.13}$$

where ρ_E is volumetric charge density. Magnetic effects can be ignored as the electric characteristic time (τ_e) is much larger than the magnetic time scale (τ_m). τ_e is given as the charge relaxation time, $\tau_e = \frac{\varepsilon_0 \varepsilon_r}{\sigma}$, where ε_0, ε_r are vacuum permittivity and relative permittivity. τ_m is given as $\tau_m = \mu_{m,r}\mu_{m,0}\sigma l^2$, where $\mu_{m,r}$, $\mu_{m,0}$, and l are relative, vacuum magnetic permeability, and the characteristic length. With $\tau_e \gg \tau_m$, electrical phenomena can be described by

$$\nabla \times E = 0. \tag{2.14}$$

Note that the hydrodynamic and electrostatic differential equations are coupled through the Maxwell stress tensor. The Coulombic force density reads,

$$\begin{aligned} \boldsymbol{F_C} &= \rho_E \boldsymbol{E} && (2.15)\\ &= (\nabla \cdot \varepsilon_0 \boldsymbol{E})\boldsymbol{E} && (2.16)\\ &= \nabla \cdot \left(\varepsilon_0 \boldsymbol{E}\boldsymbol{E} - \frac{1}{2}\varepsilon_0 E^2 \boldsymbol{I} \right) && (2.17)\\ &= \nabla \cdot \mathbb{T}_{\mathbb{E}} && (2.18) \end{aligned}$$

where $\boldsymbol{I}$ and $\mathbb{T}_{\mathbb{E}}$ are identity matrix and Maxwell stress tensor. For the Maxwell stress tensor, Kelvin or Korteweg-Helmholtz's approach can be used to obtain the electrostatic force[35]. The Kelvin approach is applicable to microscopic electromechanics, whereas Korteweg-Helmholtz is

applicable to electromechanical coupling as follows[53]

$$\boldsymbol{F_K} = \rho_E \boldsymbol{E} + \boldsymbol{P} \cdot \nabla \boldsymbol{E} \tag{2.19}$$

$$= (\nabla \cdot \varepsilon \boldsymbol{E}) \boldsymbol{E} + (\varepsilon - \varepsilon_0) \boldsymbol{E} \cdot \nabla \boldsymbol{E} \tag{2.20}$$

$$= \nabla \cdot \left(\varepsilon \boldsymbol{E} \boldsymbol{E} - \frac{1}{2} \varepsilon_0 E^2 \boldsymbol{I} \right) \tag{2.21}$$

$$= \nabla \cdot \mathbb{T}_{\mathbb{K}} \tag{2.22}$$

where P and $\mathbb{T}_{\mathbb{K}}$ are polarization density and Maxwell stress tensor in the Kelvin approach. For an electrically linear medium with polarization-dependent density and temperature, the Korteweg-Helmholtz force density is given as

$$\boldsymbol{F}_{KH} = \rho_E \boldsymbol{E} - \frac{1}{2} E^2 \nabla \varepsilon + \nabla \left[\frac{1}{2} \rho \left(\frac{\partial \varepsilon}{\partial \rho} \right)_T E^2 \right] \tag{2.23}$$

$$= \nabla \cdot \left[\varepsilon \boldsymbol{E} \boldsymbol{E} - \frac{1}{2} \varepsilon E^2 \boldsymbol{I} + \frac{1}{2} \rho \left(\frac{\partial \varepsilon}{\partial \rho} \right)_T E^2 \boldsymbol{I} \right] \tag{2.24}$$

$$= \nabla \cdot \mathbb{T}_{\mathbb{KH}}, \tag{2.25}$$

For electrically linear, incompressible dielectric medium, it holds that

$$\boldsymbol{F_E} = \rho_E \boldsymbol{E} - \frac{1}{2} E^2 \nabla \varepsilon \tag{2.26}$$

$$= \nabla \cdot \left(\varepsilon \boldsymbol{E} \boldsymbol{E} - \frac{1}{2} \varepsilon E^2 \boldsymbol{I} \right) \tag{2.27}$$

$$= \nabla \cdot \mathbb{T}_{\mathbb{E}}. \tag{2.28}$$

Pantano *et al*. (1994) solved the zeroth-order electrostatic equations from Taylor (1964) to observe the effect of charge accumulation on cone-jet formation[37, 32]. They acquired for the

first time the meniscus shape with a conical tip, assuming the vertex angle of 49.3°. Charge accumulation at the tip of the meniscus allowed the electrostatic force high enough to dominate the surface tension force in the cone-to-jet region. Furthermore, a concave-outward meniscus transitions to a convex meniscus with decreasing Taylor's number, $\frac{\varepsilon_0 \phi_0^2}{2\gamma D_e}$ where ε_0, ϕ_0, γ, and D_e are respectively vacuum permittivity, potential relative to the ground electrode, surface tension coefficient and outer diameter of the electrode[37].

2.3 Finite Volume Method (FVM)

2.3.1 Volume-of-Fluid (VOF)

The VOF method developed by Hirt and Nichols is now widely used for multiphase flow simulations[54]. In the conventional VOF method, the transport equations for two-phase volume fractions are solved together with the continuity and momentum equations given as,

$$\nabla \cdot \boldsymbol{u} = 0, \tag{2.29}$$

$$\frac{\partial \alpha}{\partial t} + \nabla \cdot (\boldsymbol{u}\alpha) = 0, \tag{2.30}$$

$$\frac{\partial (\rho \boldsymbol{u})}{\partial t} + \nabla \cdot (\rho \boldsymbol{u}\boldsymbol{u}) = -\nabla p + \nabla \cdot \mathbb{T}_\mu + \rho \boldsymbol{F_b}, \tag{2.31}$$

where $\boldsymbol{u}$, α, p, ρ, and $\boldsymbol{F_b}$ represent velocity, volume fraction, pressure, density, and body force per unit mass. In VOF simulation, the body force includes gravity and surface tension force at the interface. $\mathbb{T}_\mu$ is the deviatoric viscous stress tensor that reads,

$$\mathbb{T}_\mu = 2\mu\mathbb{S} - \frac{2}{3}\mu(\nabla \cdot \boldsymbol{u}\mathbb{I}), \tag{2.32}$$

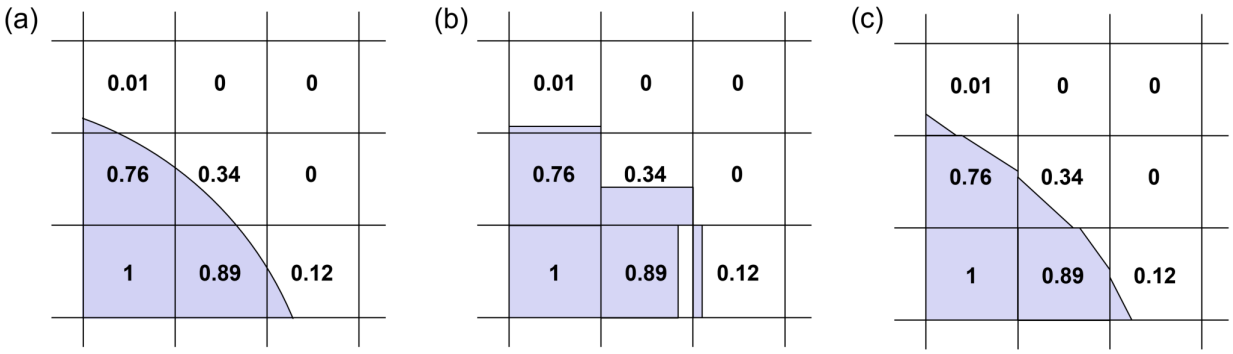

Figure 2.1: (a) True liquid interface, (b) Simple line interface construction (SLIC), and (c) Piece-wise linear interface construction (PLIC).

$$\mathbb{S} = \frac{1}{2}\left[\nabla \boldsymbol{u} + (\nabla \boldsymbol{u})^T\right], \tag{2.33}$$

where μ, $\mathbb{S}$, and $\mathbb{I}$ are dynamic viscosity, mean rate of the strain tensor, and unit tensor. The VOF method captures the interface between liquid and vacuum by employing the Heaviside function for liquid volume fraction, α_{liq}[55]. Each computational cell is represented as $\alpha_{liq} = 0$ within gas or vacuum, $\alpha_{liq} = 1$ within liquid, and $0 < \alpha_{liq} < 1$ at the interface. The method solves the volume fraction in two steps: the advection of the volume fraction and the reconstruction of the interface from the calculated volume fraction. The First-order simple line interface construction (SLIC) algorithm reconstructs the volume fraction based on the local advection of the cell boundary, whereas Piece-wise linear interface construction (PLIC) reconstructs the surface by oblique of piecewise linear line segments (or plane segments in 3D) in Figure 2.1. In the EHD problem, important parameters such as electrical conductivity and electrical permittivity are determined by the Weighted Arithmetic Mean (WAM) at the two-phase interface, as shown in Figure 2.2.

The equation for the volume fraction is discretized by the second-order accurate Crank-Nicolson method given as,

$$\left({\alpha_P}^{t+\delta t} - {\alpha_P}^{t}\right) V_p = -\sum_{f=1}^{n} \frac{1}{2}\left(\left(\alpha_f F_f\right)^t + \left(\alpha_f F_f\right)^{t+\delta t}\right)\delta t, \tag{2.34}$$

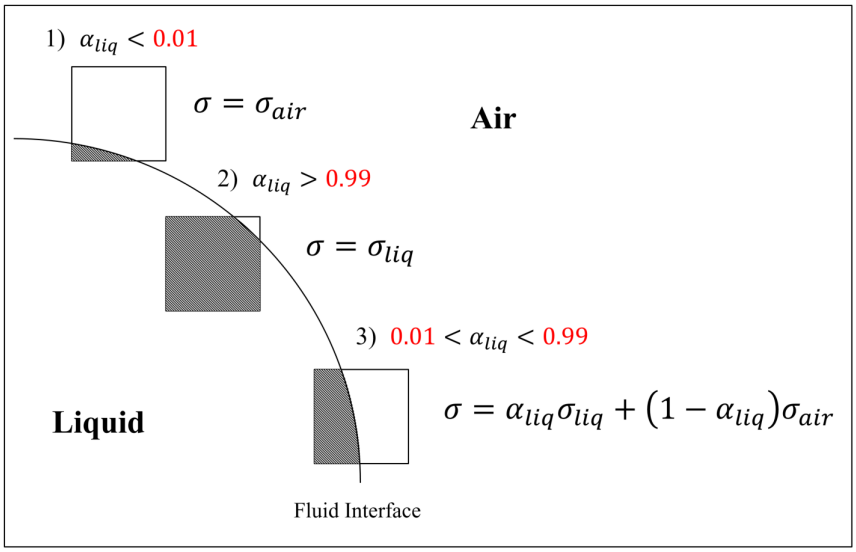

Figure 2.2: Liquid interface and averaged electric conductivities at the interface.

$$F_f = \boldsymbol{A}_f \cdot \boldsymbol{u}_f, \tag{2.35}$$

where subscripts, p and f, denote the center of the control volume and the centroid of the cell face. F_f and $\boldsymbol{A}_f$ are volumetric flux and the outward-pointing area vector normal to the surface.

CHAPTER 3

Model Formulations

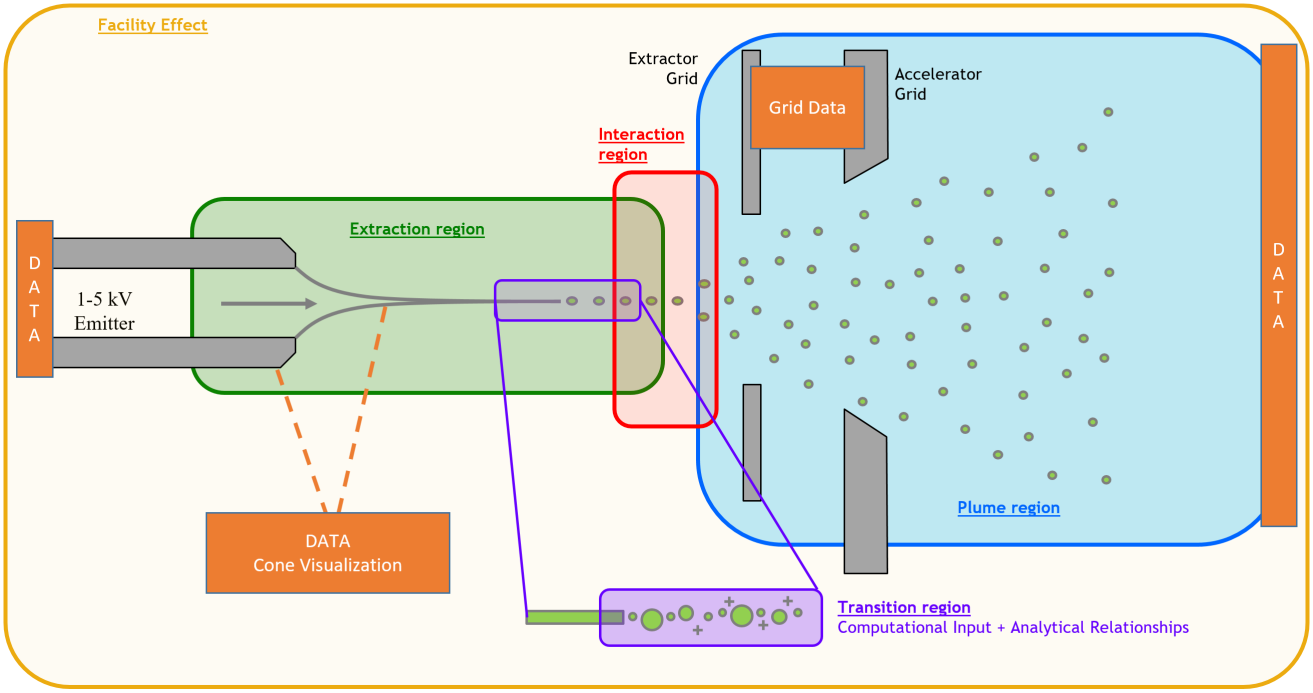

Figure 3.1: Overview of UCLA electrospray multiscale, multiphysics modeling.

To capture the wide range of physical mechanisms in the development of an electrospray plume, UCLA has divided the computational domain into several different regions in Figure 3.1. The descriptions of multiscale/multiphysics modeling regions are as follows:

- **Extraction region**: The electrostatic force overcomes the fluid surface tension and viscous force to form a cone-jet and generate droplets. The plasma, Energy and Space Propulsion Laboratory-Electrohydrodynamic (PESPL-EHD) model performs Computational Fluid Dy-

namic (CFD) analysis under incompressible and axisymmetric assumptions[56]. Note this dissertation focuses on investigating the Extraction region.

- **Transition Region**: Coulombic fission and ion evaporation may cause off-axis behavior of droplets.

- **Interaction region**: Droplet breakup and inter-particle Coulombic interactions cause the plume to expand. N-body simulations of polydisperse species are performed to produce plume shapes[57].

- **Plume region**: Coulombic interaction no longer dominates the particle dynamics. The Propagation of Electrospray Plume Particles in the Exhaust Region (PEPPER) model is a Bayesian Inference approach to determine the trajectories of plumes from the results of the interaction region[58].

- **Facility effect**: Predict the impingement currents from the plume distribution results from PEPPER, where secondary electron emission (SEE) is important. Electrospray SEE Control-volume Analysis for Resolving Ground Operation of Thrusters (ESCARGOT) model describes the emission and transport of SEE throughout the vacuum facility[59].

Huh and Wirz has developed an EHD solver in OpenFOAM (PESPL-EHD) to understand the physics of a cone-jet and droplet formation in an electrospray thruster[56]. The code requires no simplification of the charge conservation laws and includes improvements to handle the uniquely challenging properties of highly conductive propellants. Gauss's law and the charge conservation equation are solved along with the Navier-Stokes equation for the flow field and charge distribution. The full charge conservation equation is applied to consider the limits of both perfect dielectrics and perfect conductors in this work.

3.1 Hydrodynamics

Electrohydrodynamic fluid flow is governed by incompressible continuity and momentum equations given as,

$$\nabla \cdot \boldsymbol{u} = 0, \tag{3.1}$$

$$\rho\left[\frac{\partial \boldsymbol{u}}{\partial t} + \boldsymbol{u}\cdot\nabla\boldsymbol{u}\right] = -\nabla \boldsymbol{P} + \nabla\cdot(\mathbb{T}_{\mu} + \mathbb{T}_{\mathbb{E}}) + \rho\boldsymbol{g} + \boldsymbol{F}_{ST}, \tag{3.2}$$

$$\mathbb{T}_{\mu} = \mu(\nabla\boldsymbol{u} + \nabla\boldsymbol{u}^{\boldsymbol{T}}), \tag{3.3}$$

where $\mathbb{T}_{\mu}$, $\mathbb{T}_{\mathbb{E}}$, $\boldsymbol{u}$, t, ρ, $\boldsymbol{P}$, and μ represent viscous stress tensor, Maxwell stress tensor, velocity, time, density, pressure, and dynamic viscosity. Here $\boldsymbol{F}_{ST}$ is given as

$$\boldsymbol{F}_{ST} = \gamma\kappa\nabla\alpha = \gamma(-\nabla\cdot\hat{\boldsymbol{n}})\nabla\alpha, \tag{3.4}$$

$$\hat{\boldsymbol{n}} = \frac{\nabla\alpha}{|\nabla\alpha| + \delta'}, \tag{3.5}$$

where the surface tension term is reformulated according to the continuum surface force (CSF) model by Brackbill *et al.*[60] γ is the surface tension coefficient, κ is the interface curvature, and $\hat{n}$ is the unit normal vector. δ' is a small number relative to $|\nabla\alpha|$ to ensure a non-zero denominator in Eq. 3.5.

The Volume-Of-Fluid (VOF) method captures the interface between liquid and vacuum by using the Heaviside function for liquid volume fraction[55], α_{liq}. Each computational cell is represented as $\alpha_{liq} = 0$ within gas or vacuum, $\alpha_{liq} = 1$ within liquid and $0 < \alpha_{liq} < 1$ at the interface. The liquid volume fraction is calculated by solving the transport equation,

$$\frac{\partial \alpha_{liq}}{\partial t} + \nabla \cdot (\boldsymbol{u}\alpha_{liq}) + \nabla \cdot (\alpha_{liq}(1-\alpha_{liq})\boldsymbol{u_r}) = 0, \tag{3.6}$$

$$\boldsymbol{u_r} = C_{alpha}\left|\frac{\phi_a}{|S_a|}\right|\hat{\boldsymbol{n}}, \tag{3.7}$$

where $\boldsymbol{u_r}$ is an artificial compression term for sharpness of the interface[61]. ϕ_a, S_a, and C_{alpha} are velocity flux, face surface area, and an adjustable compression factor. C_{alpha} is set to unity here, whereas it is between 0 to 4 in most practical cases[62, 63]. Large C_{alpha} allows a sharp interface but increases the magnitude of possible spurious current[62, 63]. In the conventional VOF method, a cell-averaged property, ψ, such as density, viscosity, electrical conductivity, or permittivity, is calculated as

$$\psi = \psi_1\alpha_{liq} + \psi_2(1-\alpha_{liq}) \quad \text{for} \quad \psi \in [\rho, \nu, \sigma, \varepsilon] \tag{3.8}$$

where ψ_1 and ψ_2 are the properties of liquid and vacuum, respectively. The interface is reconstructed according to the liquid volume fraction, α_{liq}, and the solution of the transport equations for relevant cell-averaged properties.

3.2 Electrostatics

The volumetric electrostatic force, $\boldsymbol{F}_E$, is described by Maxwell's equations which are reduced to the electrostatic equation with negligible magnetic effect in Eq. 3.9. Gauss's law is given in Eq. 3.10 as

$$\nabla \times \boldsymbol{E} = 0; \tag{3.9}$$

$$\nabla \cdot (\varepsilon \boldsymbol{E}) = \rho_E, \tag{3.10}$$

where $\boldsymbol{E}$ is the electric field vector, ε is electrical permittivity. The charge conservation equation,

$$\frac{\partial \rho_E}{\partial t} + \nabla \cdot \boldsymbol{J} = 0, \tag{3.11}$$

is converted to Eq. 3.12 by substituting the current density, $\boldsymbol{J}$, with the sum of Ohmic conduction and charge convection as $\boldsymbol{J} = \sigma \boldsymbol{E} + \rho_E \boldsymbol{u}$.

$$\frac{\partial \rho_E}{\partial t} + \nabla \cdot (\rho_E \boldsymbol{u}) = -\nabla \cdot (\sigma \boldsymbol{E}) \tag{3.12}$$

The volumetric electrostatic force, F_E, is derived from the electrostatic Maxwell's stress tensor as

$$\mathbb{T}_{\mathbb{E}} = \varepsilon(\boldsymbol{E}\boldsymbol{E} - \frac{1}{2}E^2\boldsymbol{I}) \tag{3.13}$$

$$\boldsymbol{F}_E = \nabla \cdot \mathbb{T}_{\mathbb{E}} = \rho_E \boldsymbol{E} - \frac{1}{2}\boldsymbol{E}^2 \nabla \varepsilon \tag{3.14}$$

which is given as the sum of Coulombic and polarization forces and acts on the electric charge accumulated on the surface of an electrospray. In the two-phase flow model for immiscible fluids, boundary conditions at the liquid interface in a normal and tangential direction are given as

$$\|\varepsilon E_n\| = \rho_E, \tag{3.15}$$

$$\|E_t\| = 0, \tag{3.16}$$

where $\|\|$ denotes a jump condition across the interface. Stress balance equations in the normal and tangential directions are given as

$$\|\mathbb{P}\| + \hat{n} \cdot (\|\mathbb{T}_{\mu}\| + \|\mathbb{T}_{\mathbb{E}}\|) \cdot \hat{n} = \gamma(-\nabla \cdot \hat{n}). \tag{3.17}$$

$$\hat{t} \cdot (\|\mathbb{T}_{\mu}\| + \|\mathbb{T}_{\mathbb{E}}\|) \cdot \hat{n} = 0. \tag{3.18}$$

Important dimensionless parameters are defined as follows; the dimensionless flow rate, δ, in Eq. 3.19, the electric Reynolds number, Re_E, in Eq. 3.20, the electric Bond number, B_E, in Eq. 3.21, and the capillary number, Ca, in Eq. 3.22 where Q is the flow rate, ε_0 is the vacuum permittivity, V_0 is the emitter voltage, and R_0 is the outer radius of the emitter.

$$\delta = \frac{\rho \sigma Q}{\gamma \varepsilon_0}, \tag{3.19}$$

$$Re_E = \left(\frac{\rho \varepsilon_0 \gamma^2}{\mu^3 \sigma} \right)^{\frac{1}{3}}, \tag{3.20}$$

$$B_E = \frac{\varepsilon_0 V_0^2}{R_0 \gamma}, \tag{3.21}$$

$$Ca = \frac{\mu \boldsymbol{u}}{\gamma}. \tag{3.22}$$

3.3 Numerical Methods

The open source, OpenFOAM, is based on the FVM to obtain linearized relationships among neighboring cell-averaged variables of the governing equations[64]. The 2^{nd}-order accurate linear upwind scheme is employed to suppress false diffusion due to the discretized convection term[65, 66]. As the velocity boundary condition, a fixed uniform value is applied at the inlet, the zero-gradient condition at the outlet and the wall, the symmetry condition on the axis, and the

cyclic boundary condition at the front and the back of the wedge-shaped three-dimensional domain. Similarly, as the pressure boundary condition, the zero-gradient is applied at the inlet and zero total pressure at the outlet and the wall to maintain a vacuum in the domain.

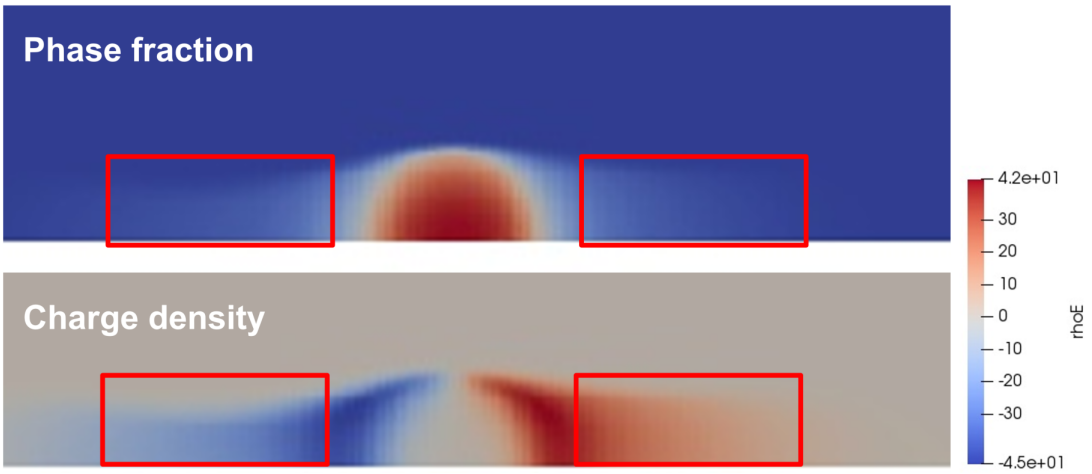

Figure 3.2: Phase fraction and charge density contour of a liquid droplet by the weighted arithmetic mean (WAM).

The VOF method is employed to reconstruct the interface to capture interfacial forces on the jet and the cone meniscus[54, 67]. Preliminary results showed the importance of avoiding false leakage of mass and electric charge through appropriate treatment of the cell-averaged quantities at the liquid-vacuum interface. Tomar *et al.* (2007); L′opez-Herrera *et al.* (2011) used the weighted arithmetic mean (WAM) for two-phase σ and ε based on the linear weighted averages in terms of the liquid volume fraction[68, 44]. In our simulation, the WAM led to significant numerical diffusion with no droplet breakup occurring, especially for moderate to high-conductivity liquids. For better validation, droplet dynamics under an applied static electric field are shown in Figure 3.3. 1000 V and 0 V are applied at the left and right sides of the domain to provide a lateral electric field. Numerical results with WAM resulted in significant numerical diffusion in volume fraction and associated charge density along the leaked fraction. L′opez-Herrera *et al.* (2011) investigated the interpolation schemes, weighted arithmetic mean (WAM), and weighted harmonic mean (WHM), concluding that the WHM does not provide any better accuracy for moderately-conductive dielectric-conducting liquid[44]. The WHM essentially assigns zero conductivity to

all cells involving a liquid-vacuum interface, resulting in code failure due to abrupt changes in the physical properties between neighboring cells. In this study, we devised a new interpolation scheme in Eqs. 3.23 and 3.24 to determine the cell-averaged conductivity and permittivity in every two-phase cell involving the interface. Note that Eq. 3.23 and 3.24 reduce to the WAM for $f = 1$ and to the WHM for $f = -1$.

$$\sigma_{cell} = \left(\alpha_{liq} \sigma_{liq}^{1/f} + (1 - \alpha_{liq}) \sigma_{vac}^{1/f} \right)^f, \tag{3.23}$$

$$\varepsilon_{cell} = \left(\alpha_{liq} \varepsilon_{liq}^{1/f} + (1 - \alpha_{liq}) \varepsilon_{vac}^{1/f} \right)^f. \tag{3.24}$$

σ_{cell} and ε_{cell} are the cell averaged quantities, while the subscripts, liq and vac, represent liquid and vacuum, respectively. Here σ_{vac} is equal to zero and ε_{vac} is equal to the vacuum permittivity, ε_0. The liquid volume fraction and the corresponding charge density are shown for $f = 1$(WAM) and $f = 20$ in Figure 3.4. Linear interpolation for the WAM results in smoothly varying σ and ε with significant false diffusion and leakage through the interface. Note the erroneous results by the WAM showing excessive droplet size and failure in charge conservation for heptane in Figure 3.4. Note that charge is well conserved to result in a converged droplet diameter showing no further dependence on f for $f > 20$ in Figure 3.5(b). It was a compromise between smooth resolution without code failure and a sharp interface with suppressed numerical diffusion. A large f better reproduces sharp variation of σ and ε with less false diffusion leading to a finer jet and smaller droplets. The maximum charge density is $\rho_E, max = 430\,\mathrm{C/m^3}$ for $f = 20$ and $\rho_E, max = 60\,\mathrm{C/m^3}$ for $f = 1$ in Figure 3.4. Finer grids will be required for better accuracy and numerical stability for electrosprays of high-conductivity liquids.

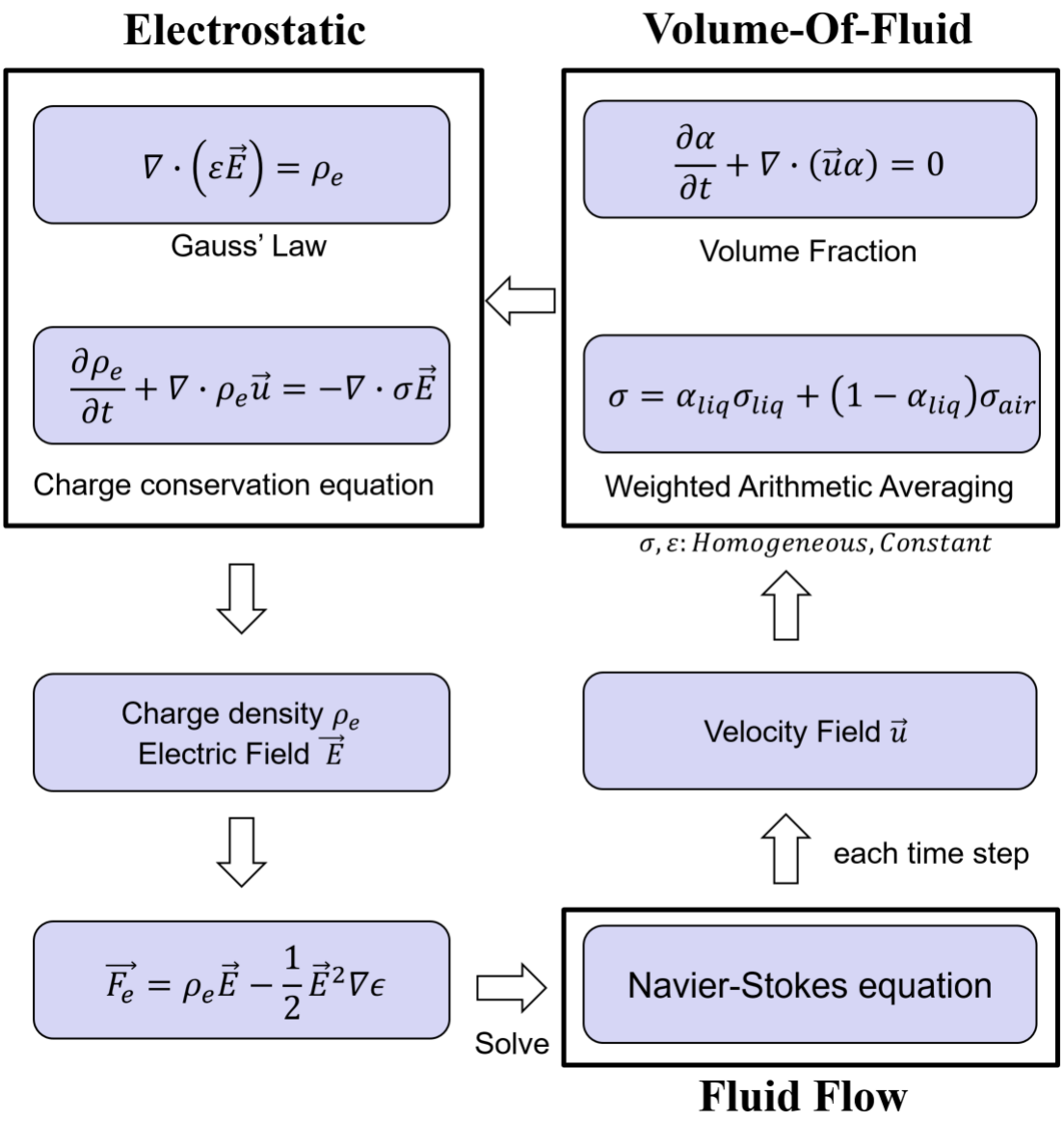

Figure 3.3: Flow chart of the electrohydrodynamics model in OpenFOAM

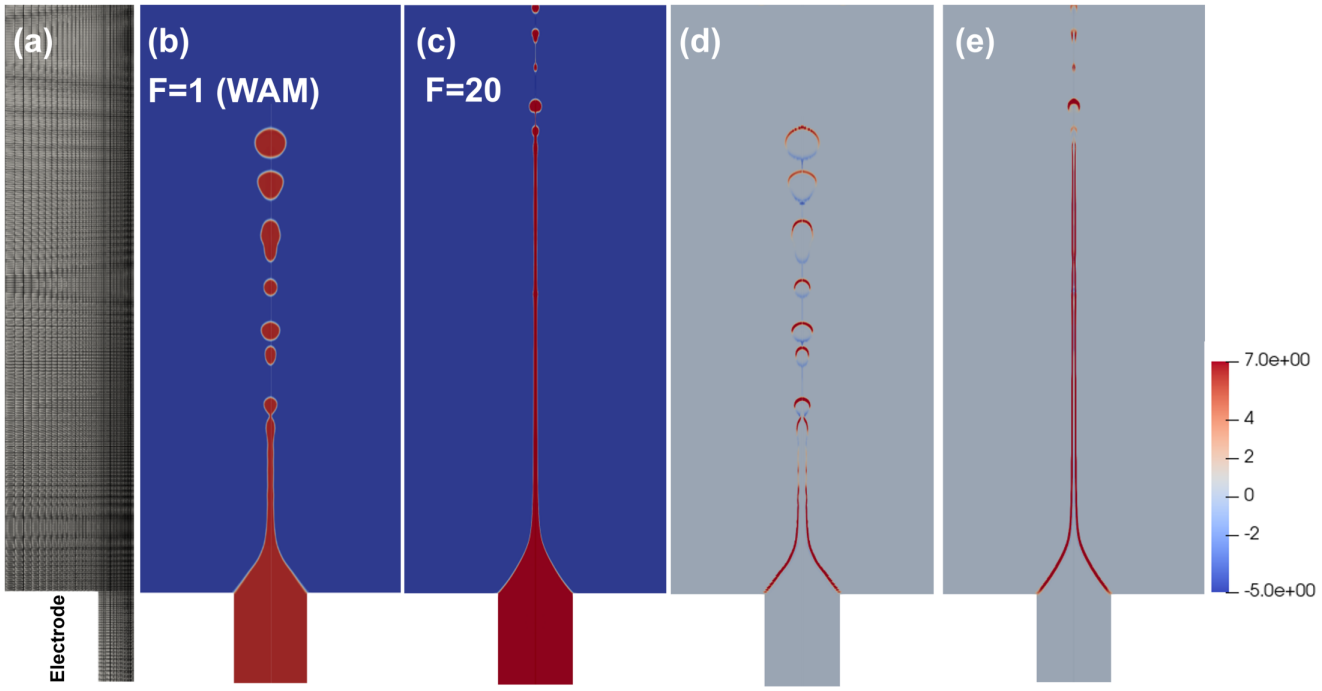

Figure 3.4: Comparison of the WAM and the new interpolation scheme for heptane, (a) computational domain, (b) liquid volume fraction for $f = 1$(WAM), (c) liquid volume fraction of $f = 20$, (d) charge density for $f = 1$, and (e) charge density for $f = 20$.

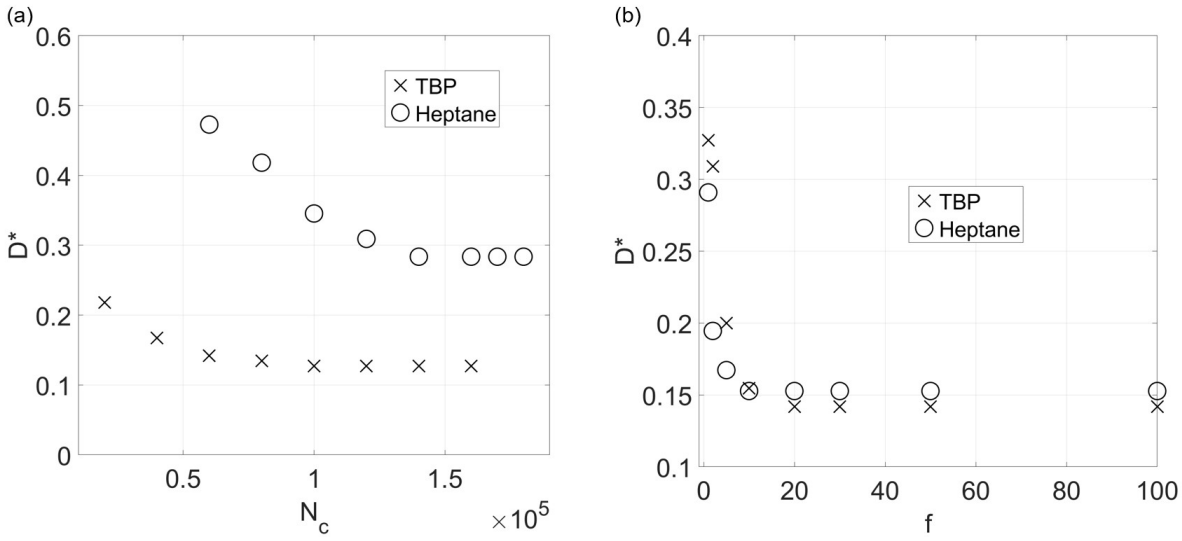

Figure 3.5: Sensitivity analysis for the dimensionless droplet diameter, D^*, with respect to (a) the number of cells, N_c, and (b) the parameter f.

CHAPTER 4

Axisymmetric Cone Jet Emission

4.1 Low conductivity liquid

The electrospray emission behaviors were reported to be in the steady cone jet mode for heptane and tributyl phosphate in this study[5, 7]. Measurements have shown the flow axisymmetric below the threshold of jet whipping at a high electric Reynolds number or a low non-dimensional flow rate[41, 10]. We limit the scope of our study to the steady cone-jet mode, where axisymmetric modes are dominant at moderate electric Reynolds numbers. A sensitivity study is performed to determine the total number of mesh cells, N_c, large enough to show no further dependence of computed results on the grid size. N_c is set equal to $138,800$ for the low conductivity case and $98,990$ for the moderate conductivity case, where the droplet diameter converges to $15.6\,\mu m$ for heptane and $6\,\mu m$ for TBP in Figure 3.5(a). Note minimum cell sizes near the axis are $0.48\,\mu m$ and $0.23\,\mu m$ for low and moderate conductivity, respectively. The average computational time step for each iteration is about $2.3 \times 10^{-8}\,s$ and $5.7 \times 10^{-9}\,s$ for heptane and TBP, respectively. The final residual of velocities, U_x, U_y, and U_z are $9.6 \times 10^{-11}\,m\,s^{-1}$, $9.0 \times 10^{-11}\,m\,s^{-1}$, and $9.8 \times 10^{-11}\,m\,s^{-1}$, and the residual for pressure is $1.5 \times 10^{-6}\,kg/ms^2$. We applied adaptive time stepping based on the maximum allowed CFL number of 0.5 for both heptane and tributyl phosphate.

4.1.1 Validation and Verification

The computational domain covers the region from emitter to extractor both in Tang & Gomez (1996) (Section 4.1) and Gamero-Castaño & Hruby (2002) (Section 4.2)[5, 7]. Simulation is based

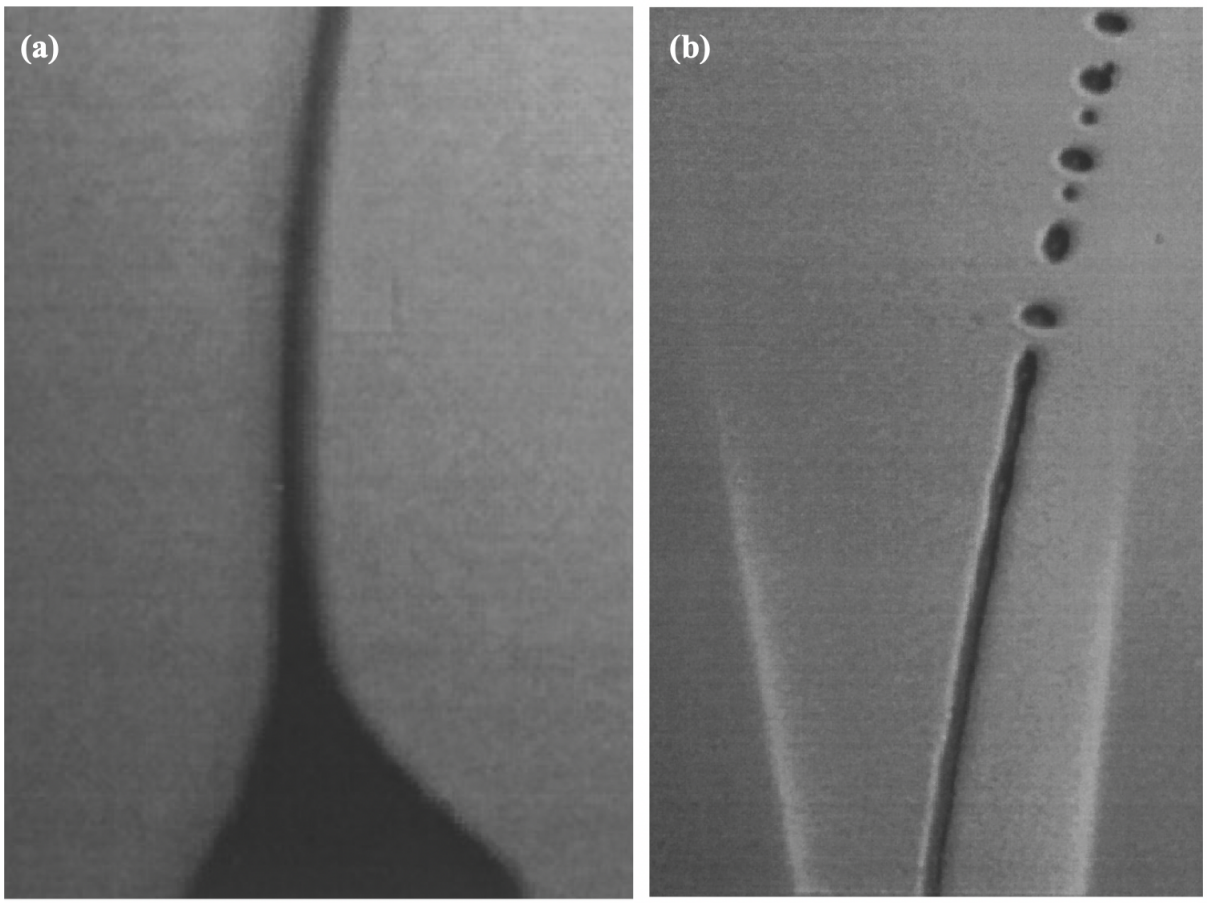

Figure 4.1: Photographs of (a) cone-jet formation and (b) emitted droplets for heptane of low conductivity[5] ($\sigma = 6.26 \times 10^{-7}\,\mathrm{S\,m^{-1}}$). Reproduced with permission from J. Colloid Interface Sci. 184, 500-511 (1996). Copyright 1996 Elsevier.

Liquid	$\rho(kg/m^3)$	$\sigma(S/m)$	$\gamma(N/m)$	$\varepsilon(F/m)$	$\nu(m^2/s)$
Heptane	684	6.26×10^{-7}	0.0186	1.91	4.28×10^{-4}
TBP	976	2.3×10^{-4}	0.028	8.91	3.59×10^{-3}

Table 4.1: Liquid properties of heptane and tributyl phosphate (TBP)[5, 7]

on the published experimental setups with the given physical properties and operating conditions, including flow rate and voltage. Photographs in Figure 4.1 show the experimentally observed cone-jet formation and emitted droplets for heptane of low conductivity. Relevant physical properties are listed for heptane and TBP in Table 6.1.

The total current, I, in an electrospray includes the two contributions by charge conduction and convection to be given as

$$I_{total} = \int_S (\sigma \boldsymbol{E} + \rho_E \boldsymbol{u}) \, \mathrm{d}\boldsymbol{S}, \tag{4.1}$$

where $\boldsymbol{S}$ is the cross-sectional surface of the cone-jet. We define the cone-to-jet length, L_{cj}, as the region where the convective current changes from 5 % to 95 % of its final value. It corresponds to the transition region in Gamero-Castaño & Magnani (2019) and the charge relaxation region in De La Mora & Loscertales (1994)[39, 8]. The charge relaxation time is defined as $\tau_e = \dfrac{\varepsilon}{\sigma}$.

Figure 4.1 shows experimental observations of cone-jet formation and droplet breakup of heptane[5]. Figure 4.2(a,b) shows the computational domain and grid for the experimental setup in Tang & Gomez (1996)[5]. The nozzle and outer diameters are 120 µm and 450 µm, the orifice diameter is 12 mm and the distance between emitter and extractor is 29.8 mm. Figure 4.2(c,d) shows the computed distributions of liquid volume fraction and contour and magnitude of the electric field on a 2-D plane through the axis. Note the concave-outward meniscus in qualitative agreement with the experimental observations in Figure 4.1(a,b). Note the maximum electric field at the cone-to-jet region well below the minimum threshold for ion emission[69] ($\sim 1\times10^9\,\mathrm{V\,m^{-1}}$). Scaling relationships by Gañán Calvo (2004) are given for the dimensionless droplet diameter and the total currents[6] in Eq. 4.2 and Eq. 4.3. Another scaling relationship by De La Mora &

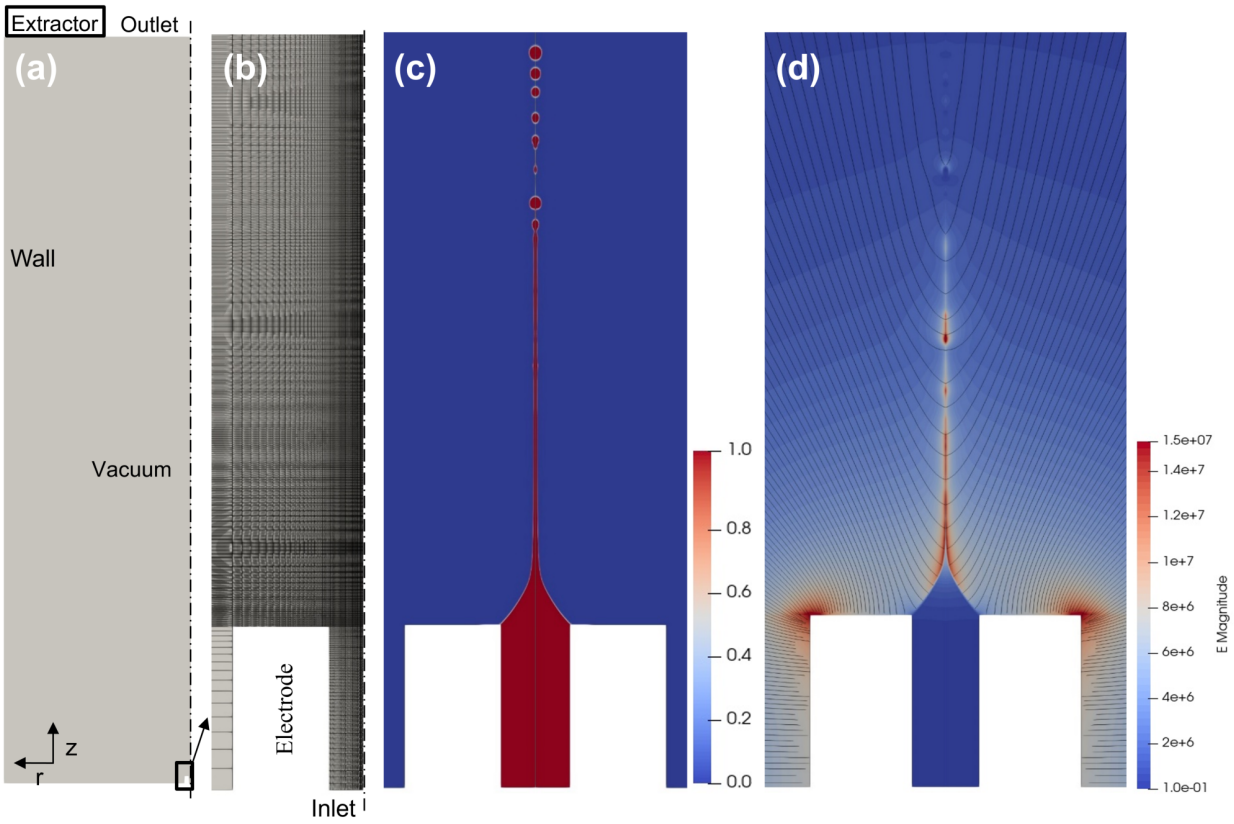

Figure 4.2: Computation for heptane of low conductivity in steady cone-jet operation; (a) axisymmetric domain with 138,800 cells, (b) magnified emission region, (c) liquid volume fraction, and (d) magnitude and contour of the electric field.

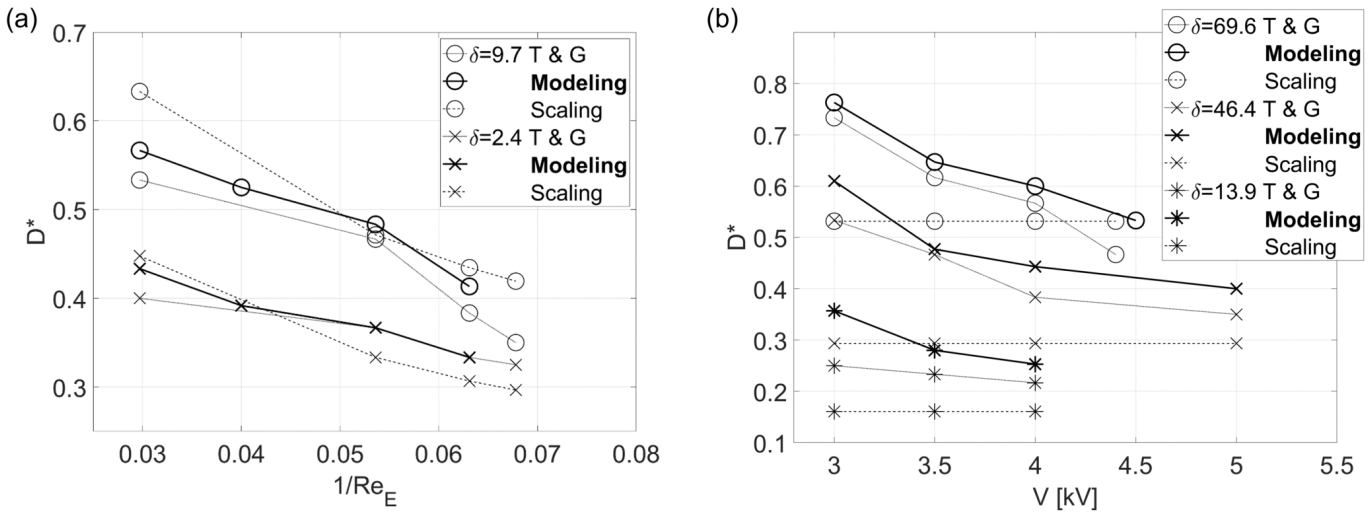

Figure 4.3: Comparison of the dimensionless droplet diameters, D^*, by experiment[5] (T & G), modeling and scaling[6] for heptane at different δ's with respect to (a) $1/Re_E$ and (b) B_E.

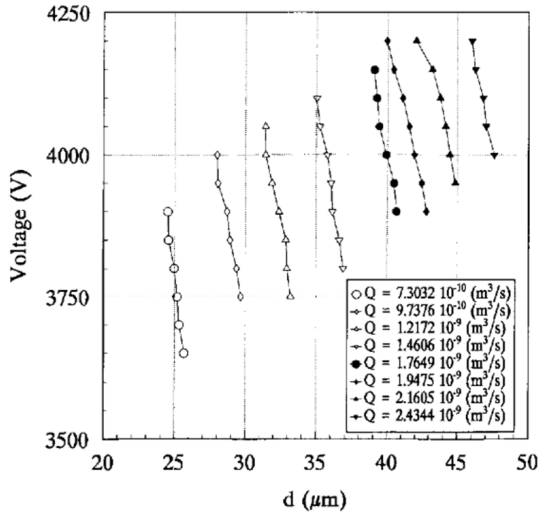

Figure 4.4: Measured droplet diameters as a function of voltage at different flow rates. Figure credit from Tang and Gomez[5].

Loscertales (1994) is given for the dimensionless droplet diameter[8] in Eq. 4.4. ε_r is the relative permittivity. These scaling relationships apply only to the steady cone-jet mode.

$$D_G = \left(\frac{\rho \varepsilon_0 Q^3}{\sigma \gamma} \right)^{\frac{1}{6}}, \tag{4.2}$$

$$I = (\gamma \sigma Q)^{\frac{1}{2}}, \tag{4.3}$$

and

$$D_D = \left(\frac{\varepsilon_r \varepsilon_0 Q}{\sigma} \right)^{\frac{1}{3}}. \tag{4.4}$$

D^* in Figure 4.3 and 4.12 is the mean droplet diameter normalized by the inner diameter of the emitter. In Figure 4.3(a) $1/Re_E$ ranges from 0.03 to 0.068 for the dimensionless flow rate varying between $\delta = 2.4$ and $\delta = 9.7$. In Figure 4.3(b) the electric Bond number is varied from 71 to 198 for the dimensionless flow rates of 13.9, 46.4, and 69.6 for $\gamma = 0.0186$ $\mathrm{N\,m^{-1}}$ according to Tang & Gomez (1996). Reasonable agreement is shown with proper trends of variation of D^* for model predictions, scaling laws, and experimental observations in Figure 4.3. The mean droplet diameter is compared with the universal scaling law in the steady cone-jet mode in Eq. 4.2 and the experimental results in Tang & Gomez (1996). The droplet size was reported to decrease with decreasing Re_E, decreasing flow rate, and increasing B_E as previously discussed in literature [6, 36, 5, 43, 8, 7]. In Figure 4.3(b), although Eq. 4.2 and Eq. 4.4 are given as functions of the flow rate and physical properties only, the measured and computed droplet diameters show a strong dependence on the emitter voltage with the increasing flow rate. The computed modeling results show the droplet diameter reduced by about 30% with the increase of the B_E from 71 to 127 at the lowest flow rate,$\delta = 13.9$, in Figure 4.3(b).

4.1.2 Sensitivity Analyses with respect to Relevant Parameters

Figure 4.5 shows distributions of the cone radius, R, and the charge density, ρ_E^*, along the meniscus for varying operating conditions and liquid properties about the reference condition, $Q = 0.5\,\mathrm{mm}^3/\mathrm{s}$, $V = 4\,\mathrm{kV}$. ρ_E^* is the volumetric charge density nondimensionalized by $\frac{(\gamma\sigma Q)^{\frac{1}{2}}}{\pi d_1^2 v_s}$, where $v_s = \frac{Q}{\pi d^2}$ is the scaling parameter for jet velocity[36, 7]. In Figure 4.5(a), the flow rate decreasing from $Q = 2.5\,\mathrm{mm}^3/\mathrm{s}$ to $Q = 0.5\,\mathrm{mm}^3/\mathrm{s}$ results in a steeper meniscus induced by increasing tangential electric field and increasing charge density according to the Gauss's law. Note the electric field magnitude increases exponentially as the flow rate decreases, as given in Gamero-Castaño (2002)[70]. A high charge density leads to a high F_E, resulting in a fine jet and small droplets with a short L_{cj}. Increasing viscosity in the range between $6.3 \times 10^{-7}\,\mathrm{m}^2/\mathrm{s}$ and $5.0 \times 10^{-5}\,\mathrm{m}^2/\mathrm{s}$ results in a jet elongated up to the location, $z = 2\,\mu\mathrm{m}$ in Figure 4.5(b). Note although the menisci are largely invariant with respect to the kinematic viscosity, ν, ρ_E^* increased, varying about 3% within the tested range of the kinematic viscosity. The increase in γ from $0.01\,\mathrm{N\,m}^{-1}$ to $0.05\,\mathrm{N\,m}^{-1}$ results in the transition from a concave to a flattened meniscus in Figure 4.5(c). Note the largest ρ_E^* and the shortest L_{cj} at the largest γ of $0.05\,\mathrm{N\,m}^{-1}$. The shown trend is opposite to the varying flow rates in (a), where the flattened meniscus has a higher charge density. At a given voltage, higher surface tension then leads to shorter cone-to-jet lengths and larger droplet sizes. In Figure 4.5(d), the tangential force increases with the increasing voltage up to 4.0 kV to result in a steeper meniscus leading to a finer jet and smaller droplet diameters. As the electric field lines emit radially from the emitter tip, further increasing the voltage of the emitter allows a higher tangential electric field leading to a higher cone angle at $\delta = 2.4$ and $Re_E = 31.3$ in Figure 4.7. The relative permittivity, ε_r, in Figure 4.5(e) shows a different trend from those for varying δ, γ, V, and ν in Figure 4.5(a) to (d). High permittivity leads to a steep meniscus induced by the high polarization force, $-\frac{1}{2}\boldsymbol{E}^2\nabla\varepsilon$, increasing with ε_r, which is dominated by the effect of the low electrostatic force due to ρ_E^* lower by 64% for $\varepsilon_r = 50$ than that for $\varepsilon_r = 10$ in Figure 4.5(e). It is due to a large charge relaxation time leading to decelerated charge transport and low ρ_E^* for the high permittivity case. In Figure 4.6, flow fields at different electrical permittivities are shown. Recirculation flow only

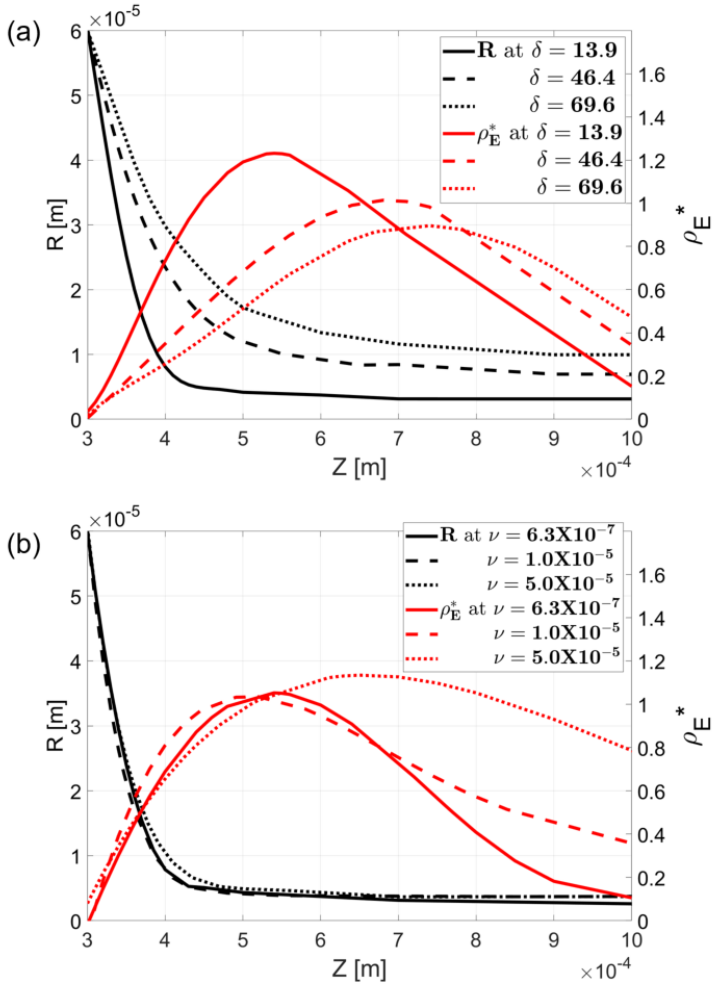
(a)
×10^-5
R [m]
Z [m]
×10^-4
ρ*E
R at δ = 13.9
δ = 46.4
δ = 69.6
ρ*E at δ = 13.9
δ = 46.4
δ = 69.6
(b)
×10^-5
R [m]
Z [m]
×10^-4
ρ*E
R at ν = 6.3X10^-7
ν = 1.0X10^-5
ν = 5.0X10^-5
ρ*E at ν = 6.3X10^-7
ν = 1.0X10^-5
ν = 5.0X10^-5

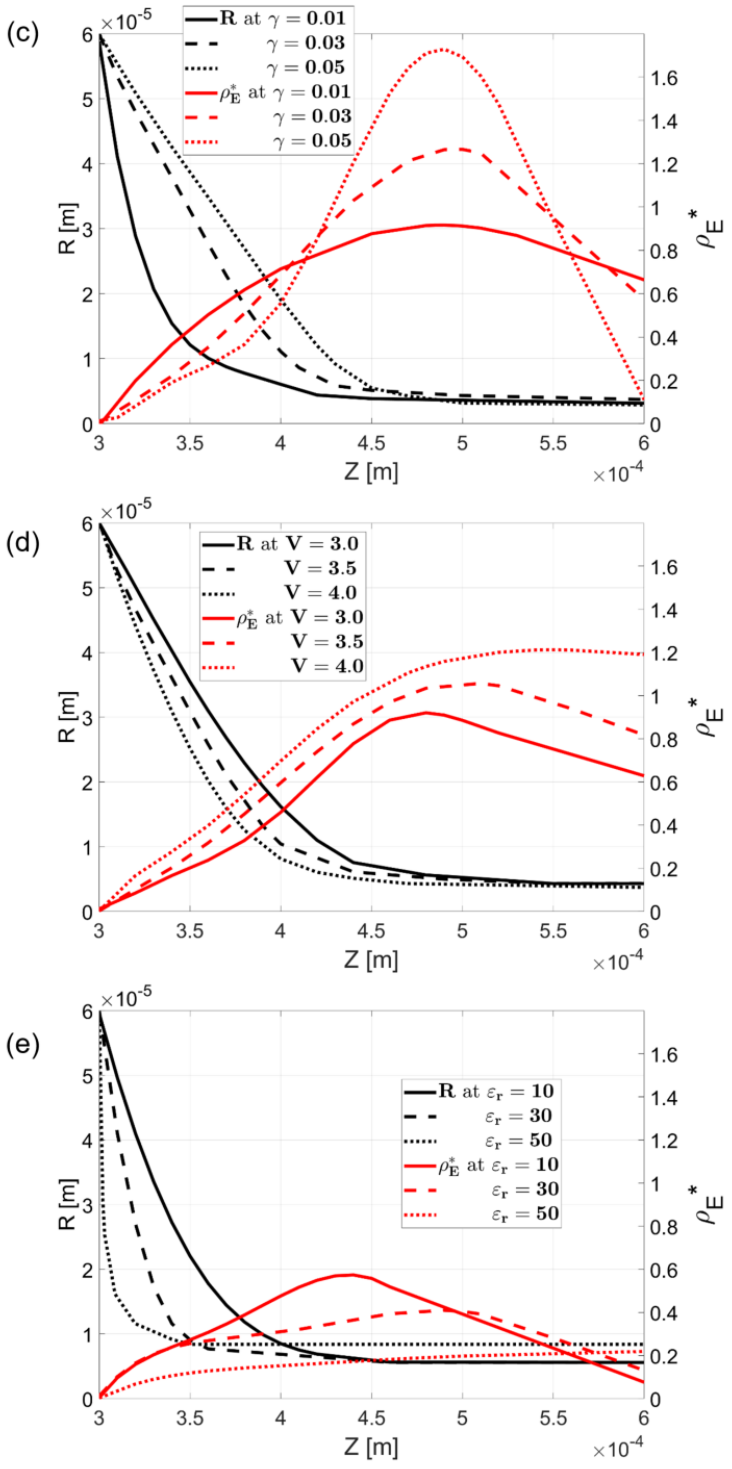

Figure 4.5: Predicted distributions of cone-jet radius and charge density along the meniscus for heptane at varying (a) flow rates Q [mm^3/s], (b) kinematic viscosities, $\nu(=\mu/\rho)$ [m^2/s], (c) surface tension coefficients, γ [N m^{-1}], (d) voltages, V [kV], and (e) relative permittivities, ε_r.

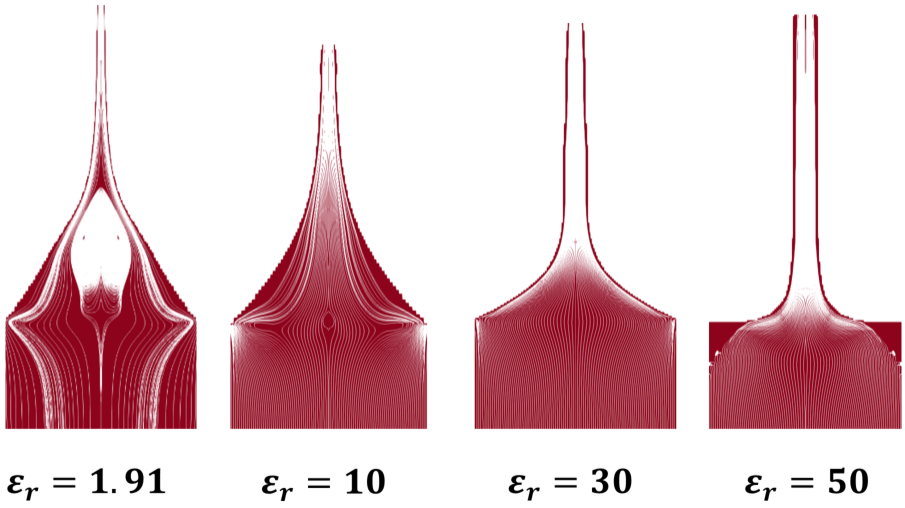

Figure 4.6: Flow fields at various electrical permittivity, (a) $\varepsilon_r = 1.91$, (b) $\varepsilon_r = 10$, (c) $\varepsilon_r = 30$, and (d) $\varepsilon_r = 50$ for steady cone-jet emission.

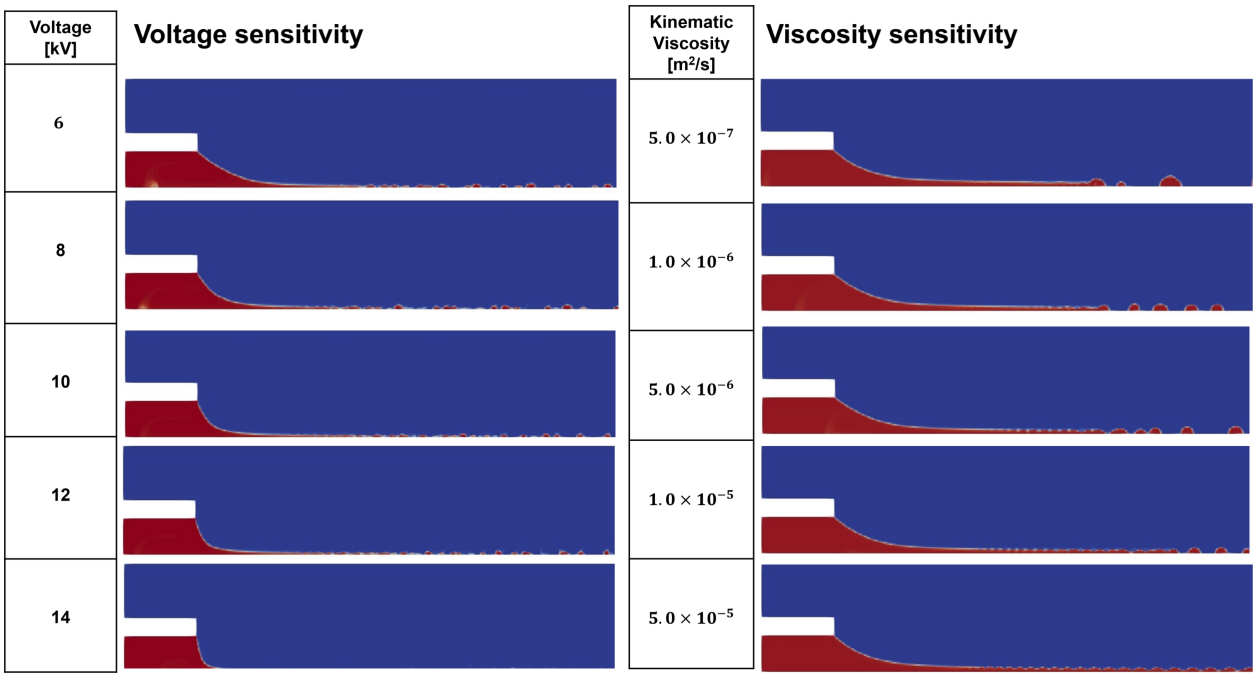

Figure 4.7: (a) Voltage sensitivity at $\delta = 2.4$ and $Re_E = 31.3$, (b) viscosity sensitivity at $\delta = 2.4$ and $B_E = 47.6$ for volume fraction.

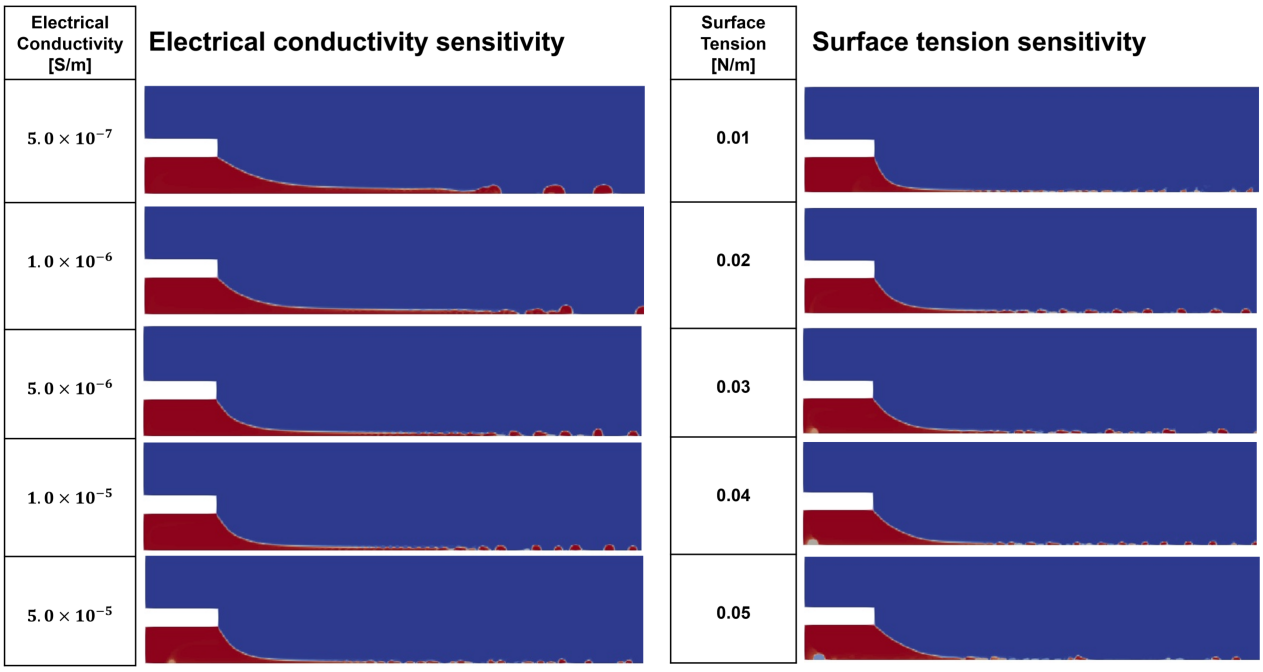

Figure 4.8: (a) Electrical conductivity sensitivity at $B_E = 47.6$, (b) surface tension sensitivity at $\frac{\delta}{B_E} = 0.05$ for volume fraction.

appears at $\varepsilon_r = 1.91$, where the tangential electrostatic force is the highest due to the low charge relaxation. Note the sensitivity analyses on varying voltage and viscosity are shown in Figure 4.7, and electrical conductivity and surface tension are shown in Figure 4.8. Increasing conductivity at $B_E = 47.6$ allows higher tangential electrostatic stress where it shows a similar effect as increasing the voltage leading to the steeper meniscus and the finer jet in Figure 4.8.

The transient evolution of the recirculation cell is described at various flow rates in Figure 4.9. The recirculation cells are generated at the cone tip at 0.3 ms in all three cases. At a low flow rate, (a) $\delta = 4.3$, the recirculation dominates inside the bulk liquid due to the high tangential electrostatic force at the liquid meniscus, whereas a higher flow rate at (b) $\delta = 8.6$, leads to the propagation of the recirculation only affecting the downstream of the cone-jet. Higher flow rate results in the transition of absolute to convective flow instability. At (c) $\delta = 17.3$, the highest flow rate leads to the recirculation cell convection toward the downstream jet, resulting in a flow without recirculation. In Figure 4.10, flow fields are shown at increasing Capillary numbers. At

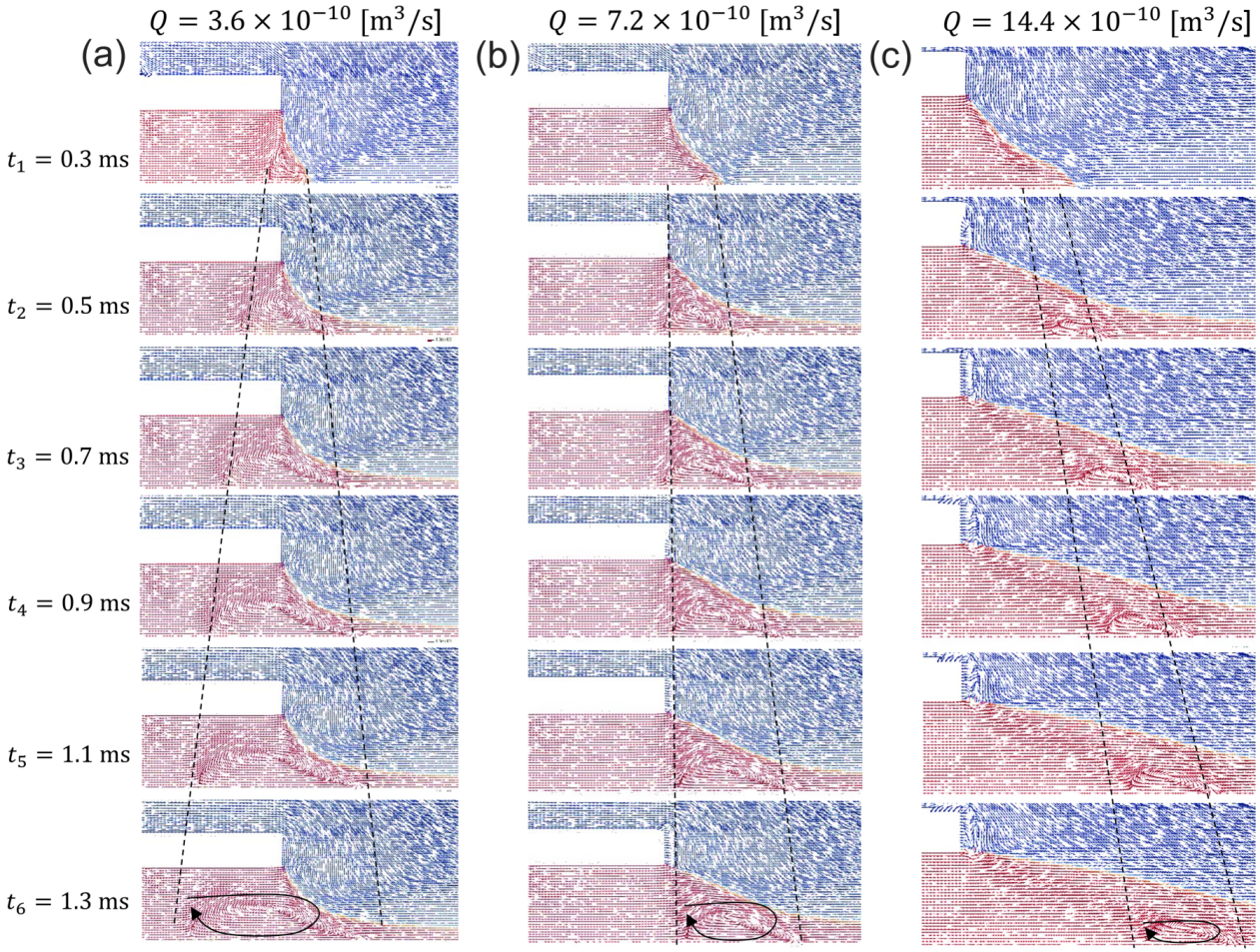

Figure 4.9: Transient evolution of the recirculation cell at different flow rates, (a) $\delta = 4.3$, (b) $\delta = 8.6$, and (c) $\delta = 17.3$ for heptane.

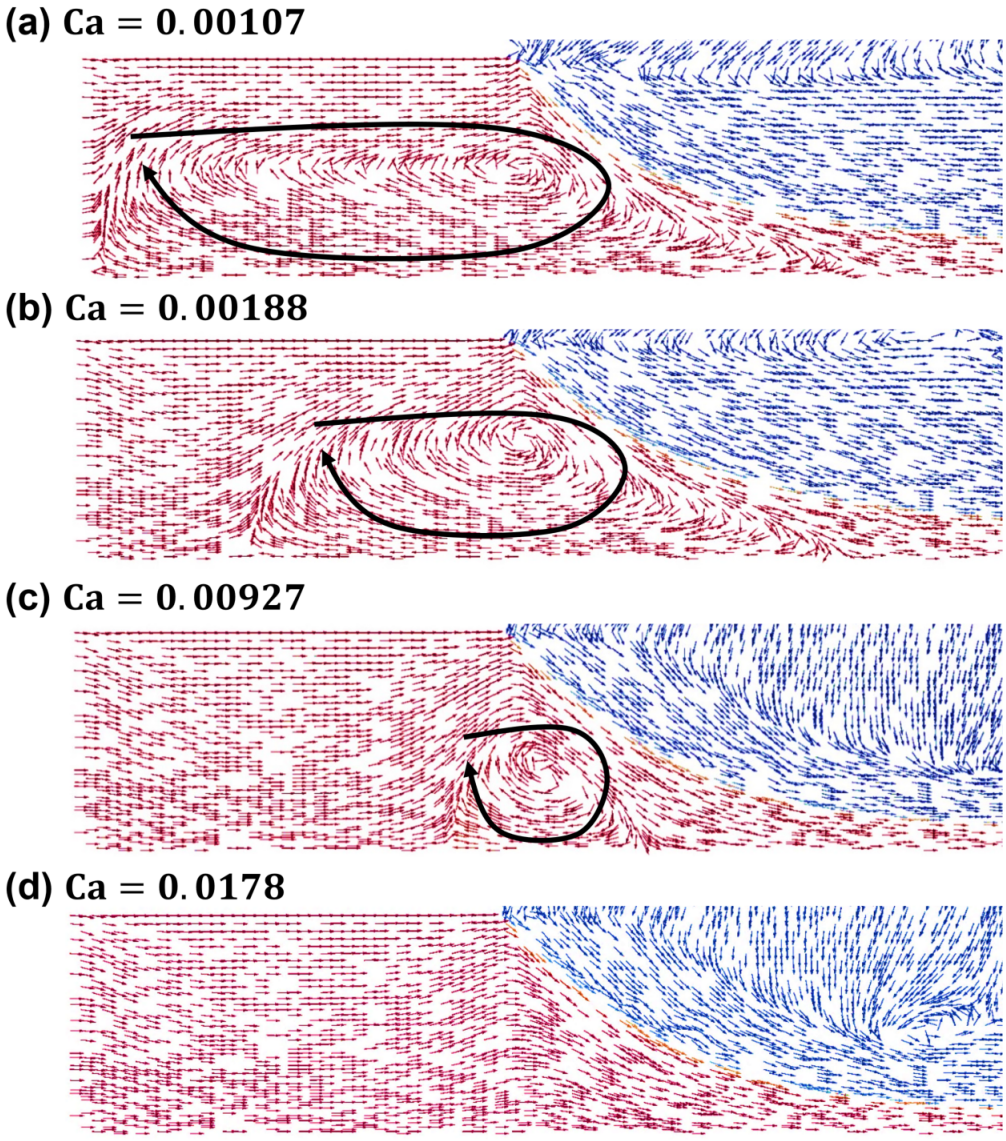

Figure 4.10: Flow fields and recirculation flows at varying Capillary number, Ca, from 0.001 07 to 0.0178.

$Ca = 0.00107$, the recirculation flow dominates the bulk fluid, where the surface tension force governs the emission behavior over the viscous force. As the Capillary number increases, the size of the recirculation cell is reduced due to the increased internal friction of viscous fluid stabilizing the flow. Note all the results in the steady state.

4.2 Moderate conductivity liquid

4.2.1 Validation of Droplet Diameter and Total Current

Figure 4.11 shows the setup and computed results of the liquid volume fraction and the electric field for TBP of moderate conductivity in Gamero-Castaño & Hruby[7]. It involves the nozzle inner and outer diameters of 110 µm and 230 µm, the diameter of the extractor orifice of 0.8 mm, and the distance between emitter and extractor equal to 2.5 mm. Note the maximum electric field of about 9.1×10^7 V m^{-1} at the cone-to-jet region, which is well below the minimum electric field of $\sim 10^9$ V m^{-1} required for ion emission[69].

Figure 4.11 shows the meniscus shape and the magnitude of the electric field in the steady cone-jet mode. Note the smaller jet diameter and smaller droplets with smaller cone-to-jet length due to higher charge density and stronger electric field than those for heptane in Figure 4.2.

Figure 4.12 shows reasonable qualitative agreement of droplet diameters and total currents by experiment, modeling, and scaling laws in Eqs. 4.2, 4.3, and 4.4. Deviation of the droplet diameters by modeling may indicate numerical uncertainty or underpredicted electrostatic force due to ignored viscous self-heating and temperature-dependent conductivity at a relatively low Reynolds number[71, 72]. In the experiment, droplets could fragment or undergo downstream influence such that droplets reaching the detector may not be those emitted off the jet[14, 73]. Note in Figure 4.12(b) the total current by modeling lying between those by experiment[7] and scaling law proportional to a half-power of the flow rate in Eq. 4.3.

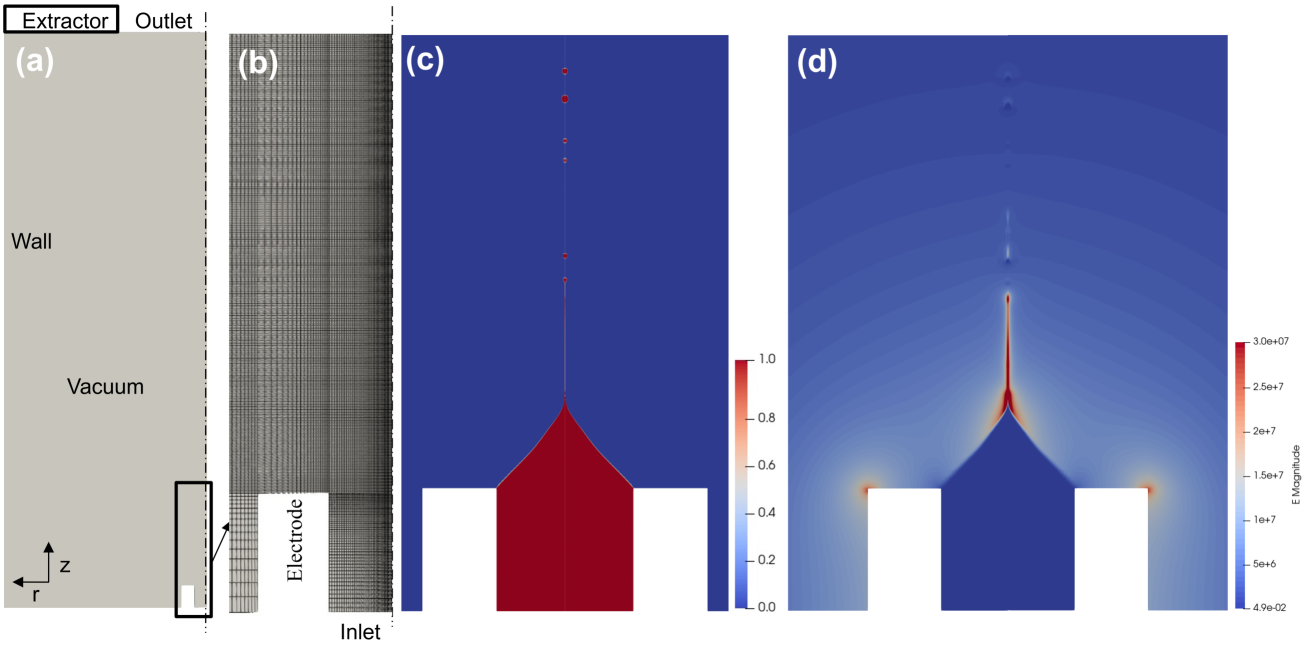

Figure 4.11: Computation for TBP in steady cone-jet operation; (a) axisymmetric domain with 98,990 cells, (b) magnified emission region, (c) liquid volume fraction, and (d) magnitude and contour of the electric field.

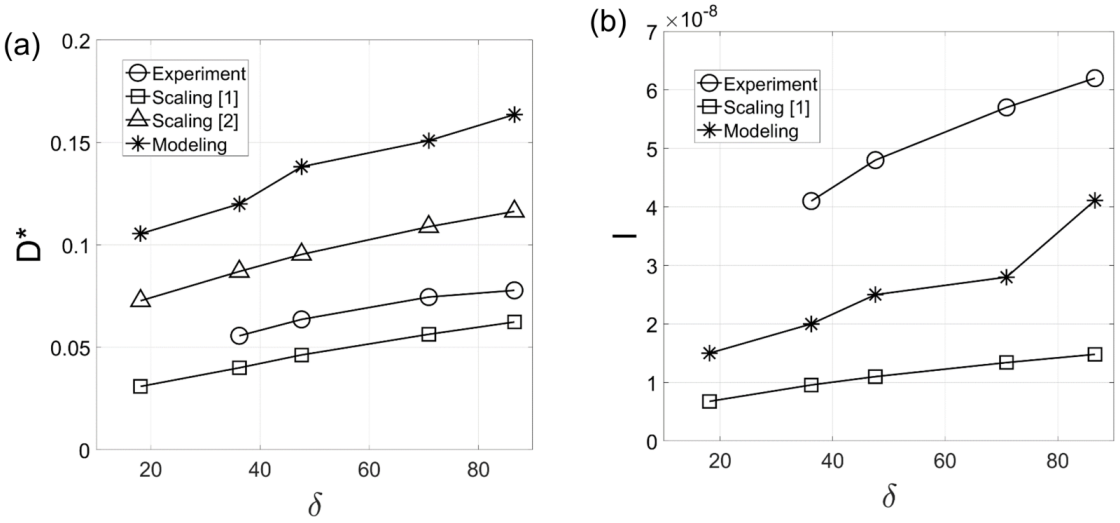

Figure 4.12: Comparison of (a) dimensionless droplet diameters D^*, and (b) total currents I [A], by experiment[7], simulation and scaling by Gañán Calvo (2004)[1], De La Mora & Loscertales (1994)[2] with respect to varying δ for TBP ($\sigma = 2.3 \times 10^{-4}\,\mathrm{S\,m^{-1}}$)[6, 8].

4.2.2 Sensitivity Analyses with respect to Relevant Parameters

Figure 4.13 shows the cone radius and the charge density along the meniscus for varying δ, γ, and ε_r about the reference condition, $Q = 0.04\,\mathrm{mm}^3/\mathrm{s}$, $V = 1.7\,\mathrm{kV}$. Note a lower δ resulting in higher charge density so that the lowest $Q = 0.04\,\mathrm{mm}^3/\mathrm{s}$ presents the highest ρ_E^* and the shortest L_{cj} in Figure 4.13(a). At a lower flow rate, the jet may develop into an unstable whipping mode due to excessive electrostatic force, as experimentally observed in Uchizono *et al.* (2020)[10]. Similarly, γ increasing from $0.01\,\mathrm{N\,m^{-1}}$ to $0.04\,\mathrm{N\,m^{-1}}$ results in increasing charge density with the transition of the meniscus from concave to convex toward the vacuum.

A scaling equation for the surface charge density, q_s, was derived from a quasi-one-dimensional analytical model as[74]

$$q_s = \varepsilon_0 E_0 = 0.62\left(\varepsilon_0 \gamma^2 \rho \sigma^2\right)^{\frac{1}{6}}, \tag{4.5}$$

which supports surface charge density increasing with increasing surface tension in Figure 4.13(b). The change in ρ_E^* is associated with transition of the meniscus from convex ($\frac{\partial^2 R}{\partial Z^2} < 0$) to concave-outward ($\frac{\partial^2 R}{\partial Z^2} > 0$). Note the maximum ρ_E^* for $Q = 0.04\,\mathrm{mm}^3/\mathrm{s}$ or $\rho_E^* = 2.5$ for $\gamma = 0.04\,\mathrm{N\,m^{-1}}$ nearly doubled as compared with the maximum ρ_E^* without such transition of the meniscus for higher δ's or lower γ's. The rapid increase of ρ_E^* with a short L_{cj} beyond the inflection point suggests that charge accumulation takes place mostly in the concave region where the electrostatic force dominates the surface tension and the viscous forces for moderate to high conductivity liquids. Low δ or high γ results in high charge density associated with high electrostatic force, leading to steeper menisci and smaller droplets. It is due to the geometrical constraint associated with the transition of the meniscus from concave to convex according to the sign of the second-order derivative along the axis.

Note that ε_r varying from 8.91 to 30 shows a relatively constant meniscus in Figure 4.13(c) unlike those for the low conductivity cases in Figure 4.5(e). The Coulombic force proportional to the charge density dominates the polarization force to determine the meniscus shape for moderate

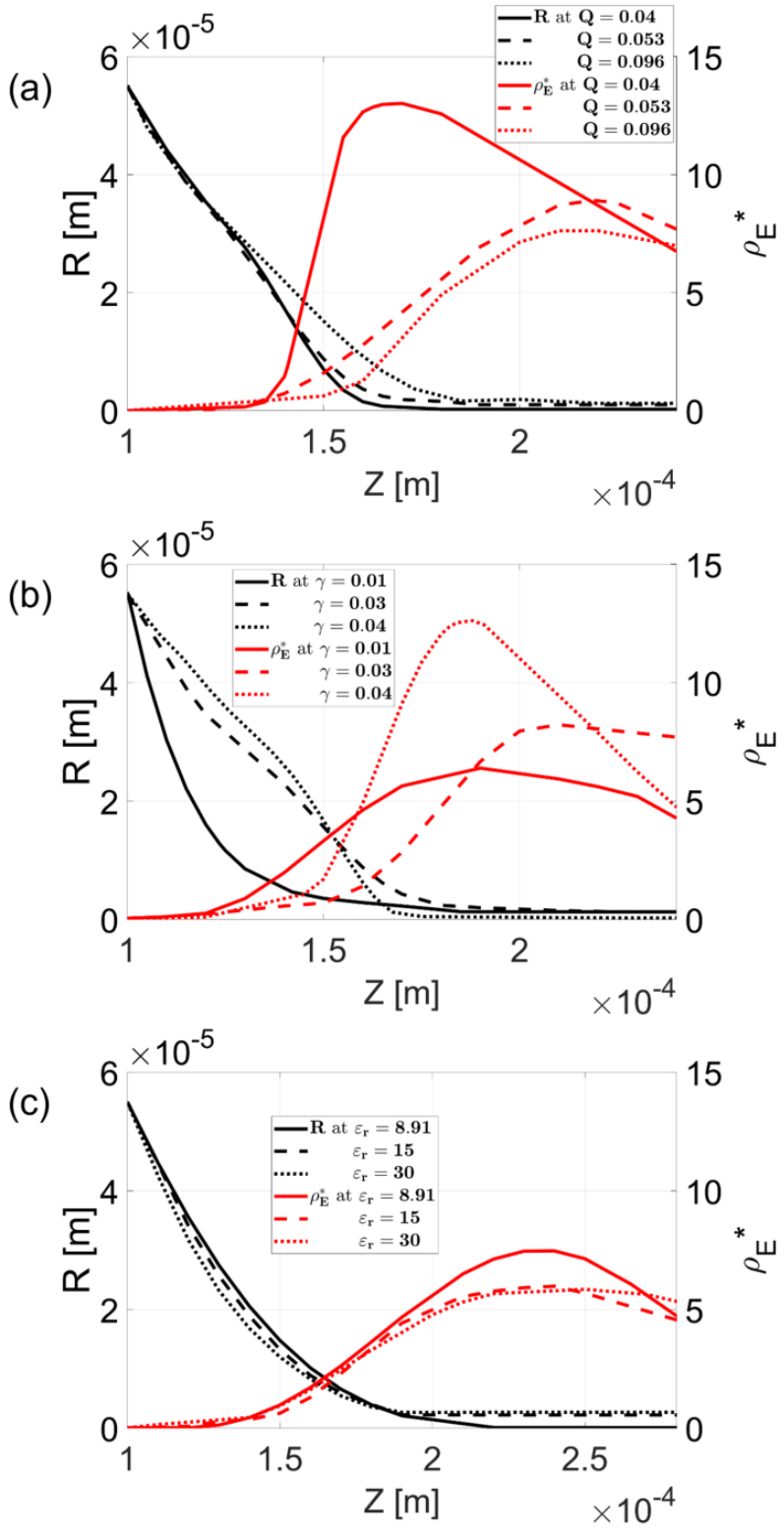

Figure 4.13: Predicted distributions of cone-jet radius and charge density along the meniscus for TBP with respect to (a) Q [mm^3/s], (b) γ [$N\,m^{-1}$], and (c) ε_r.

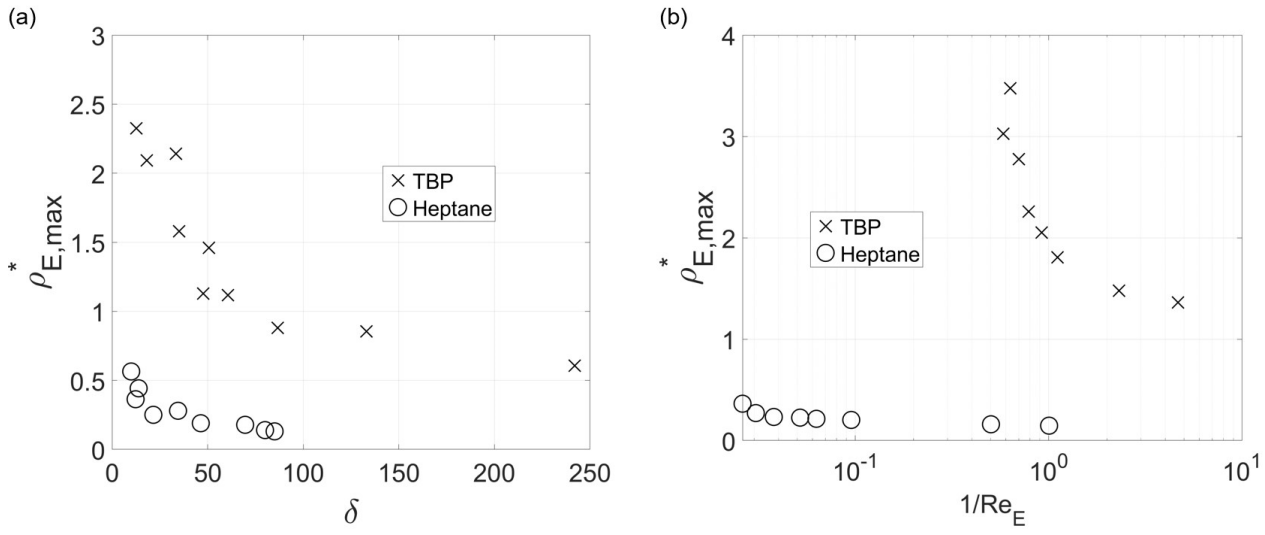

Figure 4.14: Predicted maximum charge density at the cone-to-jet region as a function of (a) the dimensionless flow rate, δ, and (b) the inverse of electrical Reynolds number, $1/Re_E$.

conductivity. The large relaxation time for $\varepsilon_r = 30$ suppresses charge transport to result in a jet radius of 265 µm much larger than 8.78 µm for $\varepsilon_r = 8.91$. It is also consistent with the result observed by Gamero-Castaño & Magnani (2019) that the normalized total current decreases from 2.5 to 2.0 for the relative permittivity increasing from 8.91 to 64.9 with no noticeable variation in the meniscus[39].

The scaling equation for q_s in Eq. 4.5 suggests the surface charge independent of the flow rate high enough above the minimum $Q^* = \delta Re_E$, to maintain a stable cone-jet[74]. The results in Figure 4.14(a) also support $\rho_{E,max}$ insensitive to δ in the range, $\delta > 50$. Note the increasing effect of δ on $\rho_{E,max}$ with increasing conductivity in Figure 4.14(a). Similarly, decreasing $1/Re_E$ results in increasing charge density with such effect intensifying with increasing conductivity in Figure 4.14(b).

The cone-to-jet length was scaled as $\frac{\gamma}{\varepsilon_0 E_t^2} \sim \left(\frac{\varepsilon_0^2 \gamma}{\rho \sigma^2}\right)^{\frac{1}{3}} \delta$ in Gañán Calvo (2004), where E_t is the tangential electric field[6]. The predicted results for the cone-to-jet length are fitted as $L_{cj} \sim \delta^{0.42}$ for heptane and as $L_{cj} \sim \delta^{0.58}$ for TBP in Figure 4.15(a). Weaker dependence on δ for heptane is associated with lower charge density, resulting in a shorter L_{cj} than for TBP. Note lower $\rho_{E,max}$ at

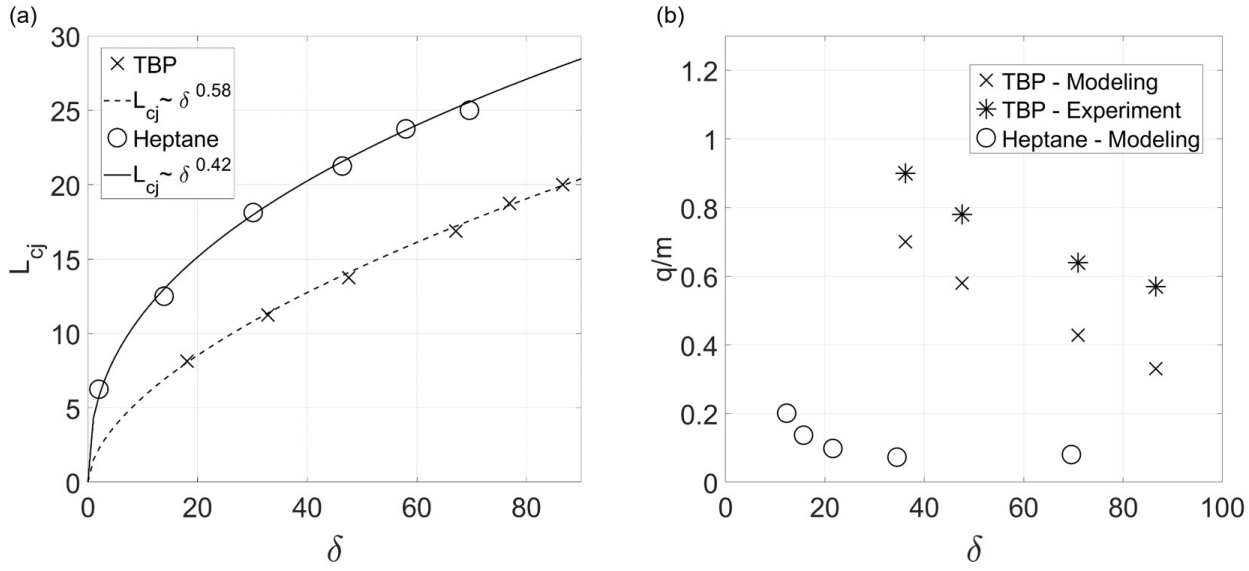

Figure 4.15: Predicted (a) cone-to-jet length [μm] and (b) specific charge [C/kg] of the emitted droplets as a function of the dimensionless flow rate, δ.

the cone-to-jet region for heptane than for TBP in Figure 4.15(a). The scaling, $L_{cj} \sim \delta^{0.58}$, fitted for TBP ($Re_E = 0.86$) shows stronger dependence than $L_{cj} \sim \delta^{0.17}$ from the BEM results in Gamero-Castaño & Magnani (2019)[39]. It may be due to the emergence of a convex meniscus leading to higher charge density and a shorter L_{cj}, which is not taken into account in Gamero-Castaño & Magnani (2019). In Figure 4.15(b), the specific charge of the emitted droplets decreases with increasing δ to support the experimental observations for moderate conductivity[7]. As a result, decreasing δ and increasing Re_E yields high charge concentration at the cone-to-jet region with shorter L_{cj} resulting in high specific charge (q/m) of the emitted droplets. Further work may be required to extend the new FVM to higher conductivity liquids, such as the ionic liquid, EMI-Im (1-Ethyl-3-methylimidazolium bis(trifluoromethylsulfonyl)imide) employed in electric propulsion. For such high conductivity liquid, the meniscus is expected to have a more convex conical shape[10] with an even shorter L_{cj}. High normal electric field, E_n, due to the increased charge density could explain possible ion evaporation at the high conductivity limit[75, 76, 77, 78].

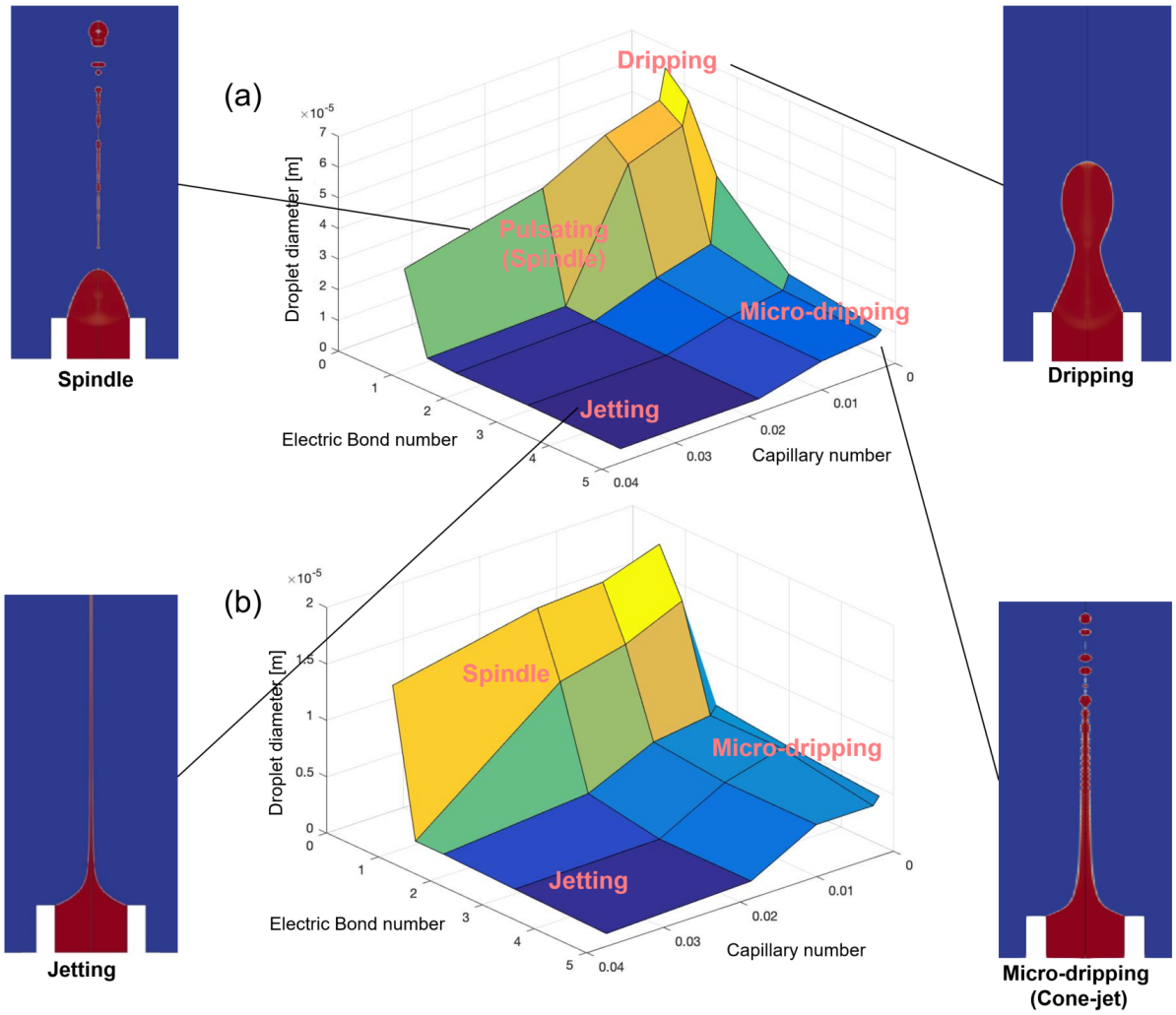

Figure 4.16: Various emission modes and meniscus shapes in the regime map at (a) $\sigma = 1\,\mu\mathrm{S\,m^{-1}}$ and (b) $\sigma = 100\,\mu\mathrm{S\,m^{-1}}$ for $B_E = 47.6$.

4.3 High conductivity liquid

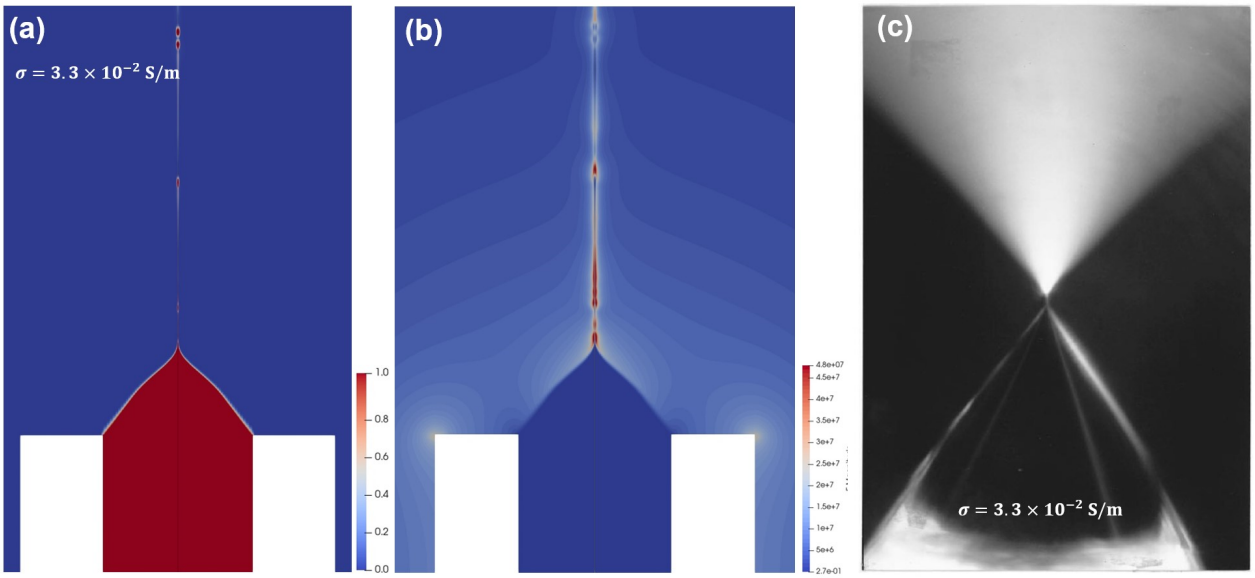

Figure 4.17: Computed (a) liquid volume fraction, (b) magnitude of the electric field, and (c) photograph of TBP ($\sim 3.3 \times 10^{-2}\,\mathrm{S\,m^{-1}}$) electrospray from Gamero-Castaño & Hruby (2002)[7].

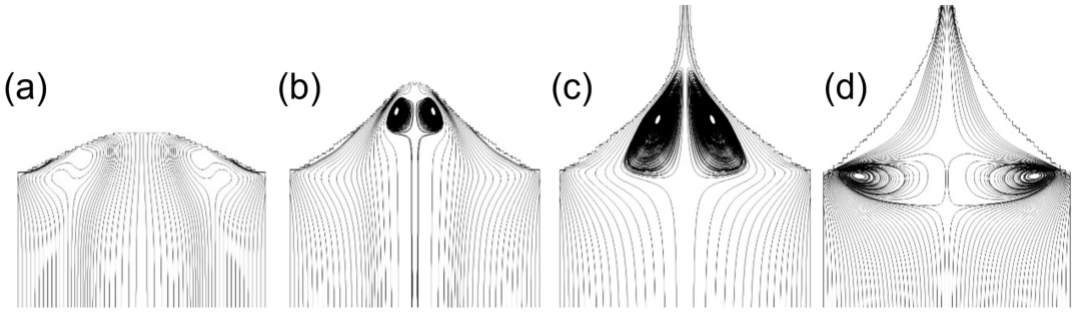

Figure 4.18: Transient evolution of recirculating flow for low conductivity liquid, heptane.

Figure 4.17(a,b) show the computed results of liquid volume fraction and electric field magnitude for TBP of high conductivity from Gamero-Castaño & Hruby (2002)[7]. The computed meniscus shape and magnitude of the electric field show good agreement with the experimental observation in Figure 4.17(c). Note that high conductivity dilates the surface, forcing more charge to the meniscus of a smaller radius of curvature. The high surface tension of TBP or the ionic

liquid, EMI-Im, resists the tangential stress, resulting in a convex meniscus. The convex shape meniscus leads to a higher charge concentration and a shorter cone-to-jet length than those of the low and moderate conductivity liquids. Unlike gradually varying menisci for low and moderate conductivity, an abrupt change allows a smaller radius of curvature at the relatively shorter cone-to-jet length for high-conductivity and high-surface-tension liquids. Note the smaller jet diameter and smaller droplets with a smaller cone-to-jet length due to higher charge density and stronger electric field than those for heptane in Figure 4.2.

As previously discussed, the tangential electrostatic force dominating the surface tension force is one of the main causes of instability in the whipping emission mode for high conductivity liquids[34, 33, 79, 17]. It is difficult to achieve stability due to high electric forces in micro-dripping (cone-jet) or jetting emission modes of high-conductivity liquid. The mechanism of dripping and jetting emissions is Rayleigh-Plateau instability, in which perturbation grows either absolutely or convectively in a homogeneous medium. Convective instability is locally not affected by the perturbations due to the high convective velocity of the liquid. In contrast, absolute instability grows without any limitation to affect both upstream and downstream of the jet for weak convective flow. Note the jet is globally unstable and going through chaotic flows such as whipping emission at a low δ above the critical B_E. Instabilities are investigated to understand how the recirculation flow affects the steady cone-jet mode at varying operating conditions and physical properties.

Recirculation flow driven by the tangential electrostatic stress in the cone was first observed by Hayati *et al.*[80] and further investigated to define the flow patterns experimentally and numerically at increasing flow rates[45, 43]. The two axisymmetric recirculation pockets reside near the emitter in the bulk liquid in the steady cone-jet mode[43, 81]. The nominal cone-jet and a single dominant recirculation cell are consistent with the published results for low conductivity[43, 41]. The computed results for low conductivity liquid in Figure 4.18 are also consistent with the similar behavior in experimental observation[81]. At startup conditions, a small recirculating pocket emerges at the tip of the cone and gradually increases at the advancing tip and induces high pressure at the neck or the cone-to-jet region of typically high charge concentration. Note the air bubble

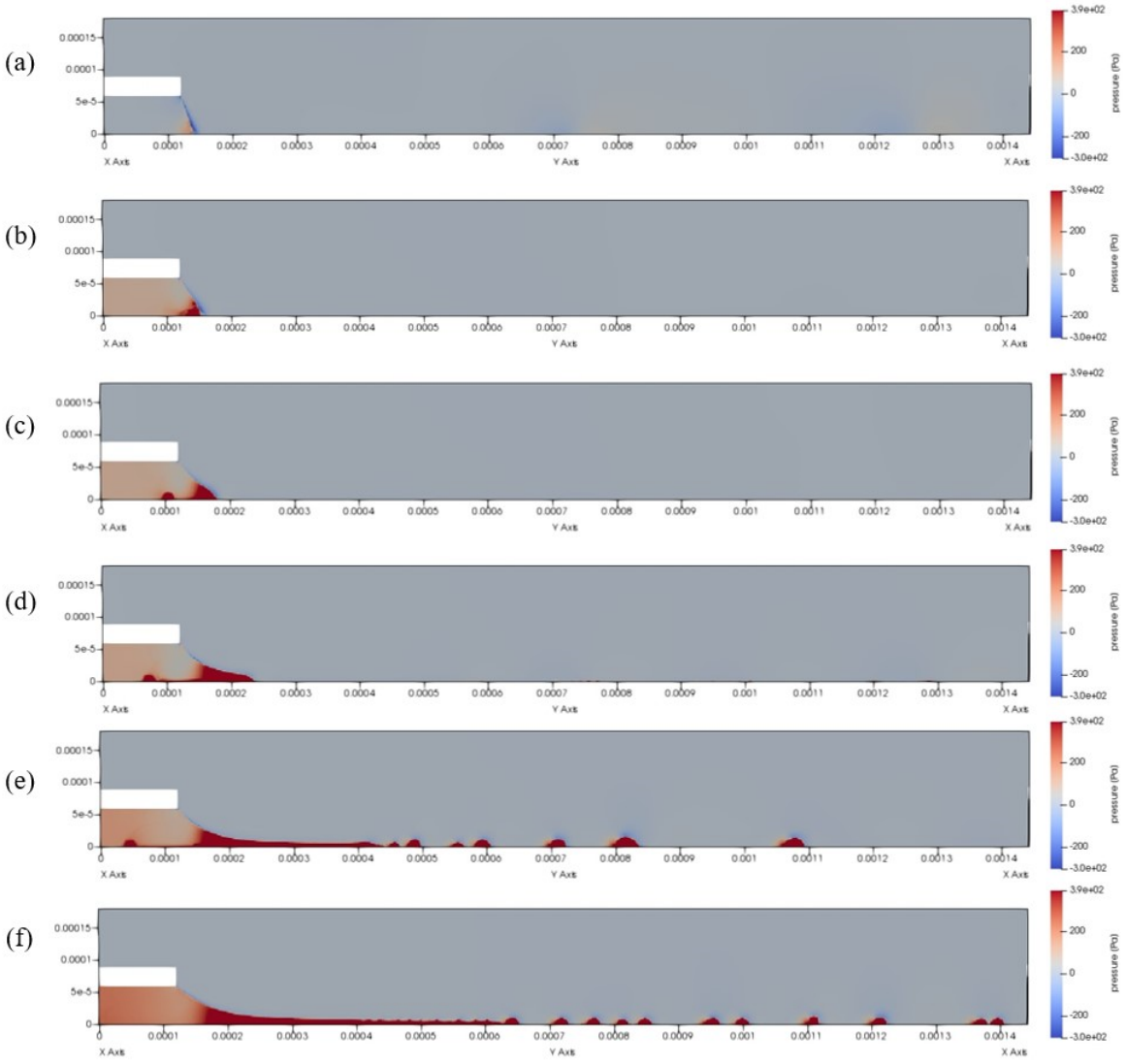

Figure 4.19: Transient evolution of the pressure field to achieve the steady cone-jet mode.

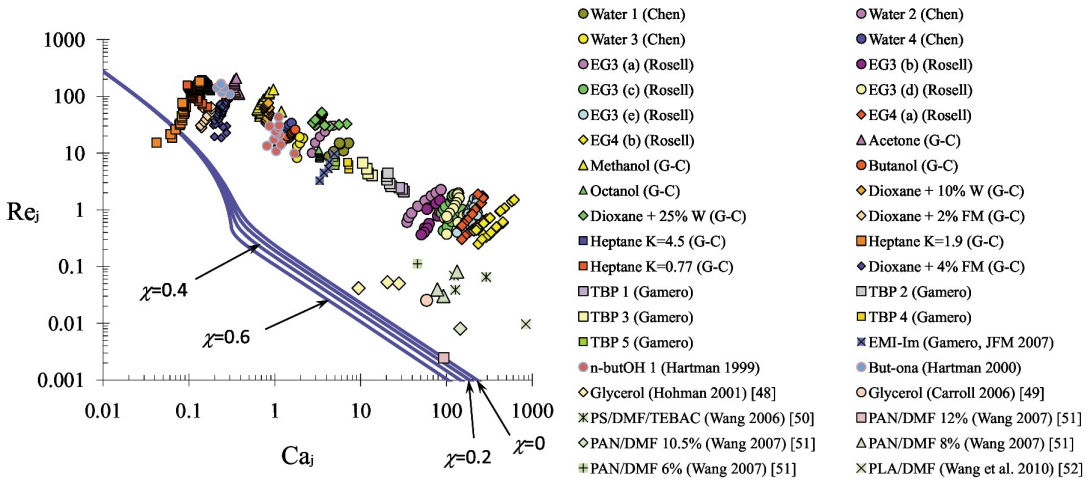

Figure 4.20: Transition between absolute and convective instabilities from Lopez-Herrera[9].

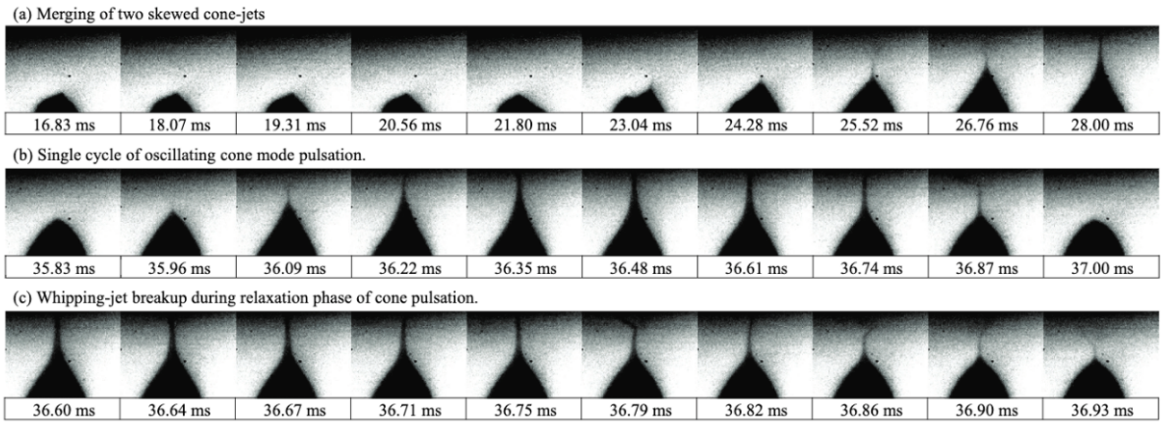

Figure 4.21: A single cycle of pulsating emission mode for EMI-Im[10].

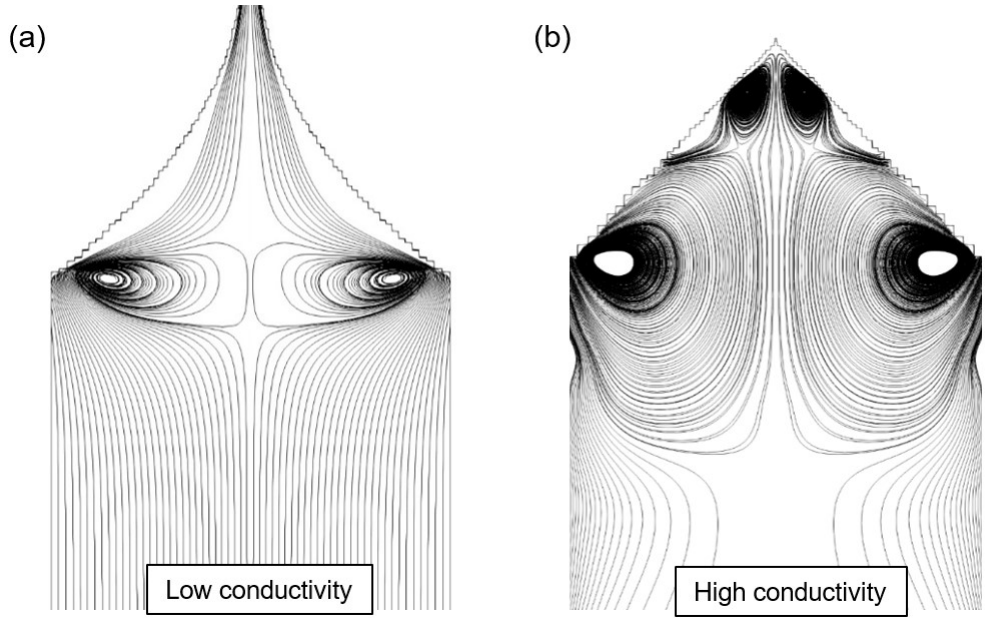

Figure 4.22: Axisymmetric recirculation flow for (a) the low conductivity liquid, heptane, and (b) the higher conductivity liquid, 10% EMI-Im. Note (b) is captured at the end of a pulsating emission cycle.

protruding from the tip of the cone due to the pressure difference at startup in Figure 4.19. There may be several detrimental issues for bubble protrusion clogging the nozzle, which will not be discussed in the work.

The high-conductivity liquid presents recirculation flow structures different from those in low and moderate-conductivity liquids. Multiple recirculation cells may emerge at the cone tip in the high conductivity liquid, unlike in lower conductivity liquids near the minimum flow rate at the end of each pulsation cycle in Figure 4.22. Recirculation structures also strongly depend on varying flow rates and electric Reynolds numbers. Reducing the flow rate results in recirculation emerging at $\delta = 47.6$, and dominating at $\delta = 18.1$ in Figure 4.23. Note the evolution of the recirculation flow for low and high-conductivity liquid is shown in Appendix B. Change of the meniscus shape, flattened surface from the concave meniscus, provokes high electric stresses at the cone-to-jet region where the radius of curvature is small at a lower flow rate. The recirculation structure begins to grow stronger at a lower flow rate where the cone shape is flattened or convex. Increasing the

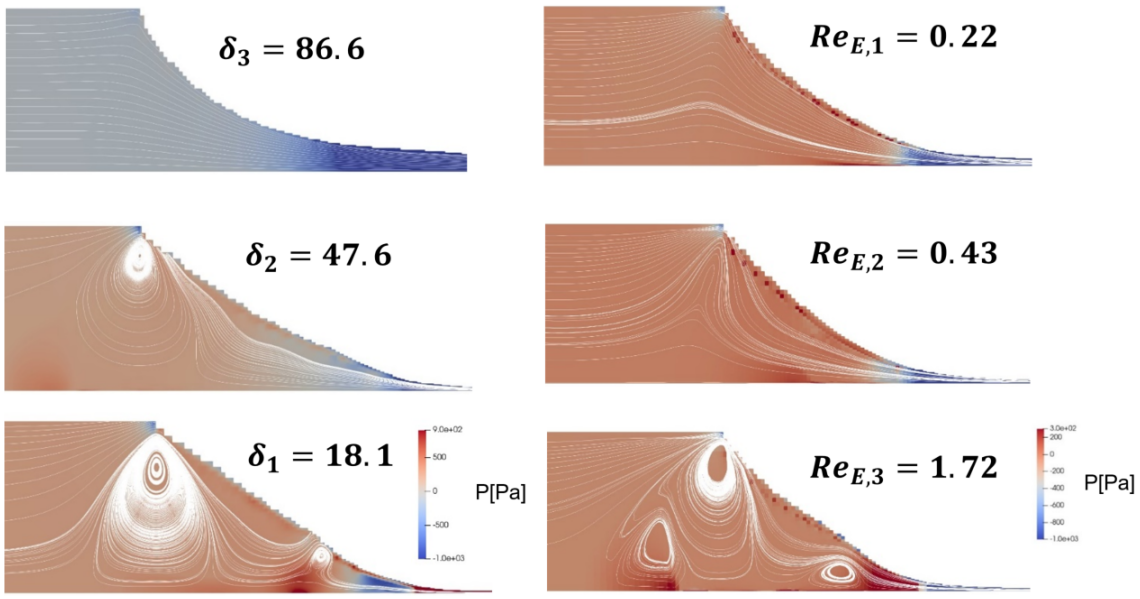

Figure 4.23: Recirculation flows and pressure fields at varying flow rates, $\delta_1 = 18.1$, $\delta_2 = 47.6$, and $\delta_3 = 86.6$ and electric Reynolds numbers, $Re_{E,1} = 0.22$, $Re_{E,2} = 0.43$, and $Re_{E,1} = 1.72$.

electric Reynolds number causes instability in the flow allowing multiple recirculation cells, and may lead to a failure of the cone-jet mode. The highly pressurized region is due to the recirculation of the flow. Note high-frequency pulsating emission around 800 Hz at the operating conditions and geometrical configuration given in Gamero-Castaño & Hruby[7]. A growing recirculation cell indicates high $\rho_E \boldsymbol{E}$ induced by small δ, which is attributed to the onset of axisymmetric instability and spontaneous toroidal flow as the axisymmetric instability breaks down[82, 83, 84]. For example, the axisymmetric meridional flow intensifies with more than one recirculation cell emerging with lower δ and higher Re_E in the high conductivity regime. This implies the onset of axisymmetric instability due to high tangential electrostatic force at the cone-to-jet region and the resulting toroidal motion intensifying with the increasing applied potential along the jet[24].

Besides these axisymmetric behaviors, nonlinearity in the EHD equations leads to asymmetric unsteady cone-jet behavior as well as the formation of off-axis main and satellite droplets. Shtern and Vladimir observed swirl motion due to flow instability, which was claimed to be due to the axisymmetric breakdown of recirculation[83]. Recently, it was shown experimentally that azimuthal

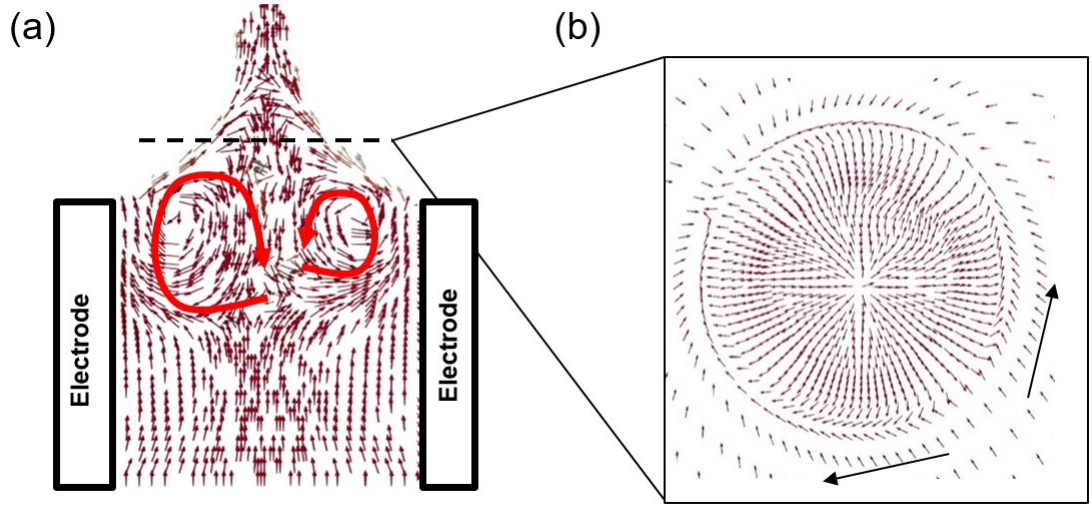

Figure 4.24: (a)An asymmetric recirculation flow field inside the cone-jet and (b) the flow field of a horizontal cross-section of the jet at the dotted line

instability contributes to swirling motion around the saddle point near the apex of the Taylor cone for ethanol[81]. We observed asymmetric recirculation flow by employing a three-dimensional model (which will be discussed in Chapter 6) in Figure 4.24. The breakdown of axisymmetric recirculation led to two toroidal flows swirling in opposite directions in Figure 4.24, i.e., whipping instability at the jet. The onset of the whipping jet occurs at the end of a pulsating emission cycle according to Uchizono *et al.*[10]. It implies that axisymmetric recirculation at the cone tip evolves into toroidal flow motion in the bulk fluid and develops whipping instability near the minimum stability flow rate.

4.4 Geometric Effect

The mission lifetime of an electrospray thruster is critically affected by unstable emission modes at off-nominal flow rates and voltages. MicroNewton Thruster (CMNT) operates in the droplet modes of capillary emitters at a high thrust-to-power ratio and low specific impulse. On the other hand, externally-wetted electrospray thrusters operate in the ion mode at a high specific impulse but

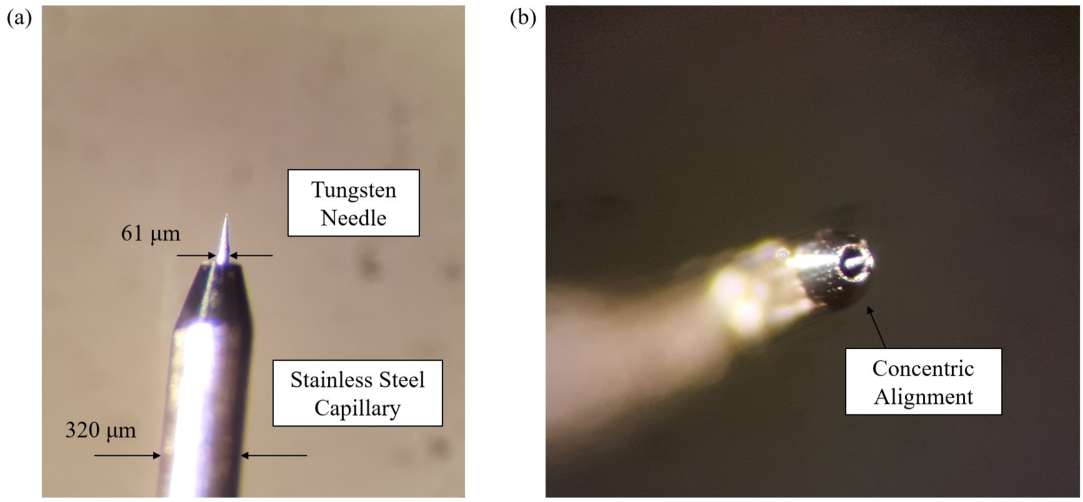

Figure 4.25: (a) Coaxial emitter of stainless steel capillary of 320 µm outer diameter with 61 µm diameter with the tapered end, tungsten needle, and (b) magnified photograph showing a concentric alignment. Photographs credit from Wright *et al.*[11]

lower thrust-to-power ratio. A new emitter design here applies an additional needle in the emitter to achieve the ion or the droplet mode at different operating conditions as shown in Figure 4.25. An externally-wetted needle allows the field emission at the tip at a low flow rate, resulting in the ion mode, whereas capillary emission forms a liquid cone to result in the droplet mode at a high flow rate, as shown in Figure 4.26. The emitter consists of a chamfered stainless steel capillary (SIS Metal TaperTip electrospray emitter) and 61 µm diameter tungsten wire. More details are given on the experimental apparatus in Wright *et al.*[11]

The externally-wetted needle provides several advantages due to a stronger electric field at the tip of the needle. The tip promotes ion emission at lower flow rates, while the concentric needle helps to maintain an axisymmetric structure of the cone jet, prohibiting any off-axis behavior from a tilted cone or whipping motion of the propellant. Liquid volume fraction and magnitudes of the electric field are shown for (a) the standard and (b) coaxial emitter in Figure 4.27 and Figure 4.28. The high magnitude electric field of the coaxial emitter can be explained through the problem of two-conducting spheres. If the conducting spheres of two different sizes are in direct contact, the equipotential surface is given by $V = \frac{1}{4\pi\varepsilon_0}\frac{\rho_{E,s1}}{r_{s1}} = \frac{1}{4\pi\varepsilon_0}\frac{\rho_{E,s2}}{r_{s2}}$ where r_{s1} and r_{s2} denote the large and

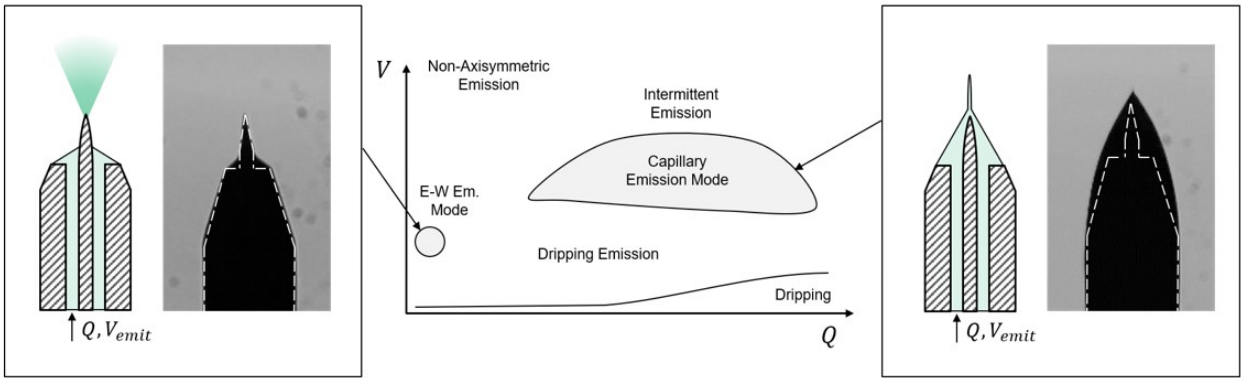

Figure 4.26: Design and operating regimes of the coaxial emitter in Wright *et al.*[11]

Figure 4.27: Liquid volume fraction for (a) the standard emitter and (b) the coaxial emitter at $\delta = 2.7$ and $B_E = 169$.

Figure 4.28: Electric field magnitude for (a) the standard emitter and (b) the coaxial emitter at $\delta = 2.7$ and $B_E = 169$.

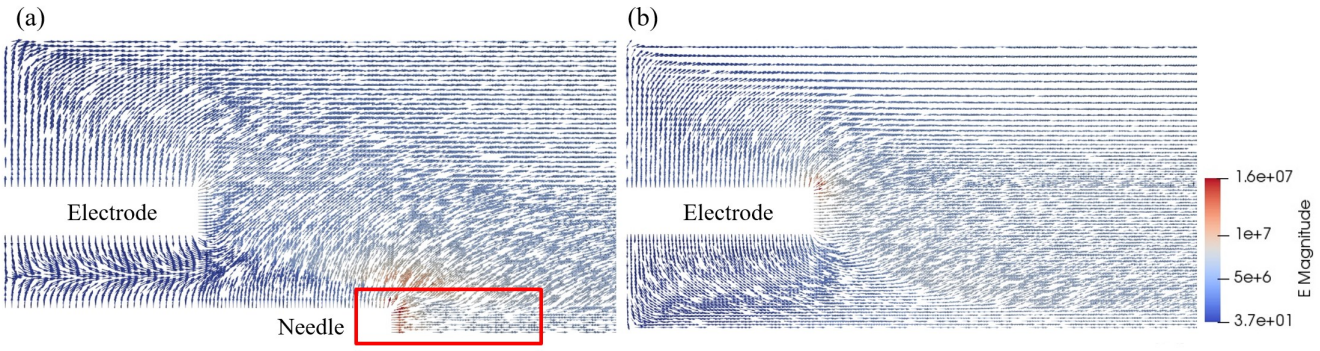

Figure 4.29: Electric field vectors and magnitudes for (a) the coaxial emitter and (b) the standard emitter.

the small radius of the spheres. Assuming a large diameter of the outer emitter and a small diameter of the needle, the needle provides higher charge density so that $\rho_{E,s1} < \rho_{E,s2}$. The protruded needle results in a stronger electric field around the emitter in Figure 4.25(b). Note the electric field at the outer tip of the standard emitter is stronger than that at the coaxial emitter, where the electric charge moves toward the tip of the needle. It suggests that a sharp tip on the body of the emitter should be carefully avoided in manufacturing the emitter. Also, reduced protrusion length resembles the operation of the capillary emitter at a low emitter voltage due to high electrostatic force in the stability regime map. The startup voltage was approximated as[85],

$$V_{start} = \sqrt{\frac{\gamma R cos\theta_T}{2\varepsilon_0} ln\left(\frac{4d}{R}\right)} \tag{4.6}$$

where R, θ_T, and d are emitter radius, cone angle, and emitter-extractor distance.

Figure 4.30 shows the pressure fields in the standard emitter and the coaxial emitter at $\delta = 2.7$, $B_E = 169$. Note higher pressure and local surface tension of reduced radius of curvature match the high electrostatic force due to the high electric field induced at the tip of the needle in the coaxial emitter. This leads to a finer jet and smaller droplet diameters with a higher charge-to-mass ratio. The flow fields are shown for two different flow rates of the coaxial emitter in Figure 4.31. The flow field at $\delta = 4.32$ resembles recirculation flow in the renowned backward-facing step with a larger recirculating cell for increasing $Re = \frac{\rho u L}{\mu}$[86]. This axisymmetric recirculation may break

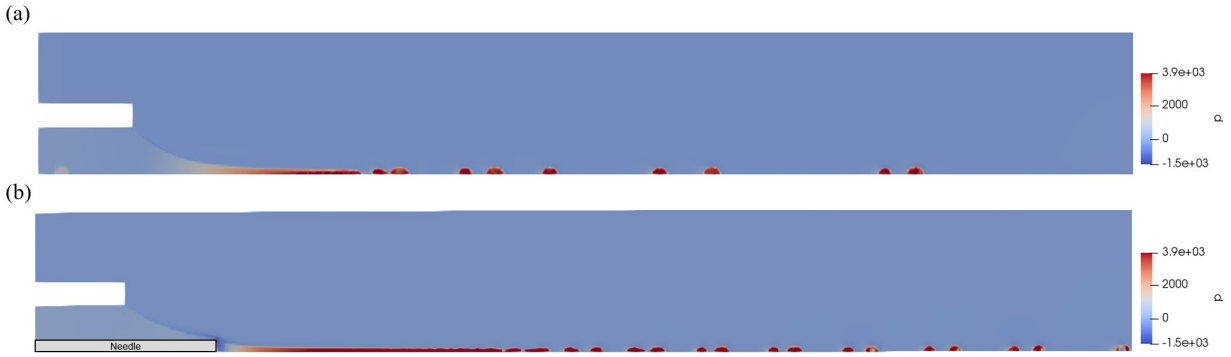

Figure 4.30: Pressure field for (a) the standard emitter and (b) the coaxial emitter at $\delta = 2.7$ and $B_E = 169$.

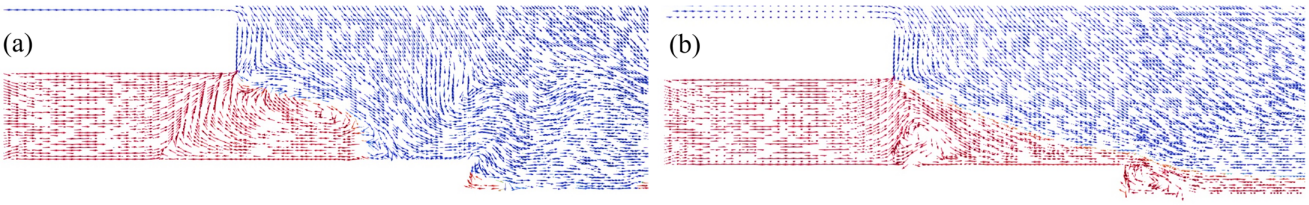

Figure 4.31: Flow fields for the coaxial emitter at different flow rates, (a) $\delta = 1.08$ and (b) $\delta = 4.32$.

down to cause meridional flow motion and influence the thruster's lifetime, which will be discussed later. Further sharpening of the needle tip may reduce the recirculation and promote field emission in the coaxial emitter.

Figure 4.32 shows the volume fraction and the electric field at different emitter tip angles. Liquid with a steeper meniscus shows higher electric field magnitude at the tip for a larger chamfering angle. A small radius of curvature promotes high charge concentration, as the electric charge goes through strong electrostatic repulsion on a flat surface in Figure 4.32(c). Consequently, any sharp point must be avoided in the manufacturing of the emitter for the operation of the electrospray thruster in its full capacity. Note the chamfered tips are rounded to avoid unnecessary field emission in Figure 4.32(b,c).

Continuous wetting of the outside emitter is another significant problem not yet understood in the thruster operation[15, 16]. Stacking the propellant may cause unfavorable emission modes

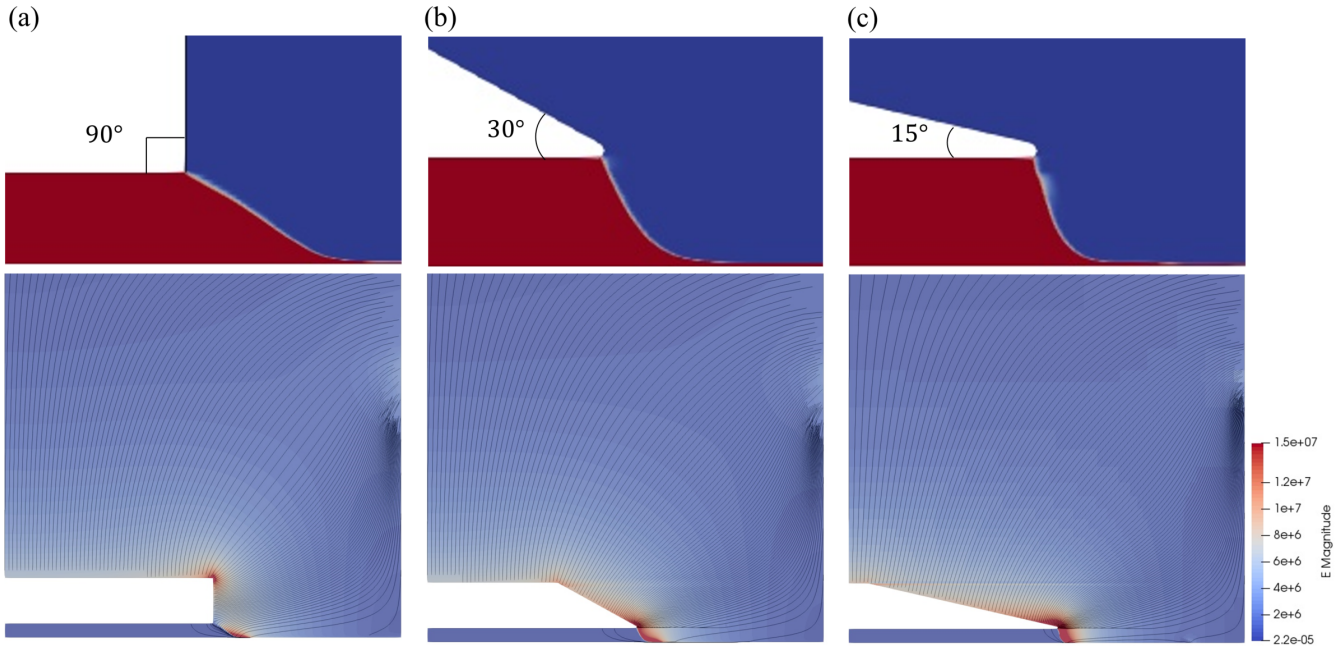

Figure 4.32: Electrospray emission with (a) blunt, (b) 30° chamfered, and (c) 15° chamfered tip emitters for TBP of electrical conductivity, $\sigma = 3.3 \times 10^{-2}\,\mathrm{S\,m^{-1}}$.

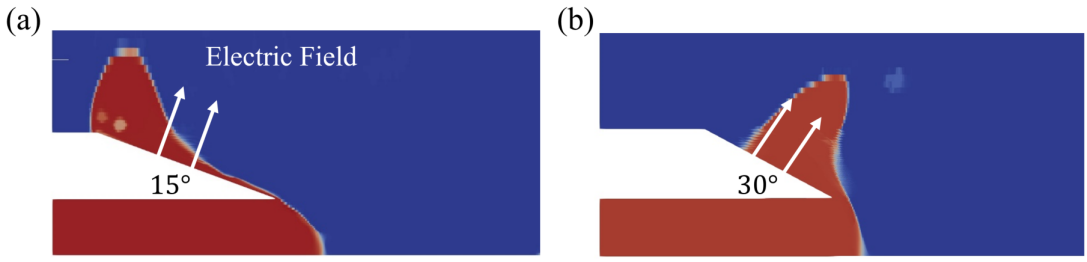

Figure 4.33: Propellant wetting at the outer emitter for (a) 15° chamfer angle and (b) 30° chamfer angle at startup condition, $T = 0.1\,\mathrm{ms}$.

at startup emission. In particular asymmetric wetting is subject to tilted-cone emission leading to overspray of the emitter[15, 14]. Figure 4.33 shows the emitters with two different chamfer angles, 15° and 30° at startup, $T = 0.1\,\mathrm{ms}$. The electric field normal to the emitter surface is depicted as a white arrow at both angles, 15° and 30°. Note the tangential electrostatic force promoting to wet the emitter at the triple point, where the emitter, liquid, and vacuum meet. It is because the advancing contact angle is larger than 90 degree at the triple point. As the chamfer angle increases, it tends to impede wetting in exchange for a low thrust efficiency. As a lower chamfer angle allows higher emitter efficiency due to higher charge concentration, the chamfer angle should be carefully selected for a robust emitter with less wetting and higher thrust efficiency.

CHAPTER 5

Energy Analysis and Joule Heating Effect

5.1 Motivation: Temperature Dependent Propellants

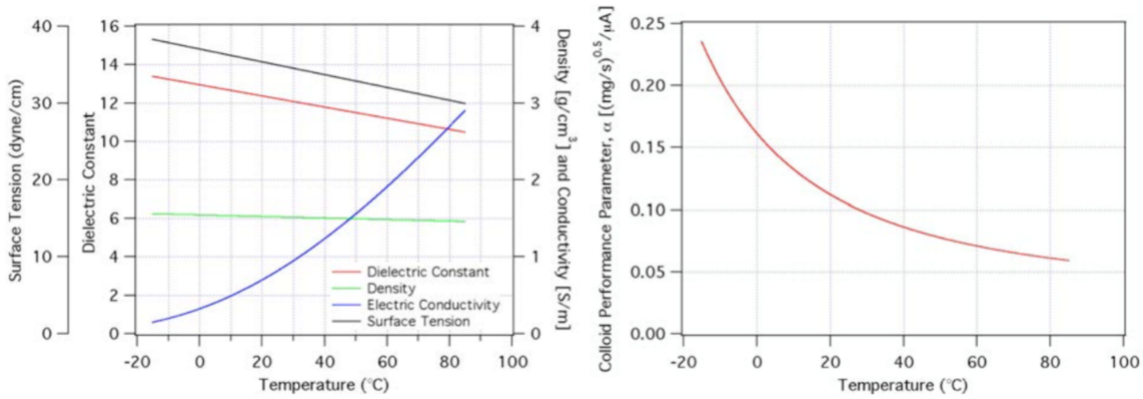

Figure 5.1: Liquid properties of EMI-Im (left) and the colloid performance parameter (right), α, as a function of the temperature. Figure credit from J. Ziemer[12].

The propellant temperature can significantly impact the cone-jet droplet emission and the ionization process in the electrospray transition region. In general, electrospray characteristics strongly depend on the propellant's physical properties. Temperature change affects the propellant's key liquid properties, such as electrical conductivity, permittivity, surface tension coefficient, and viscosity. Viscosity significantly decreases with increasing temperature, which enables increased emission current through the jet[87, 88]. Ion beam currents tended to increase with increasing temperature, resulting in an increased proportion of large cluster ions, whereas that of smaller cluster ions decreased with increasing temperature[89]. Experiments measuring a voltage deficit via retarding potential analyzer reveal that the largest fraction of the voltage deficit of the

emitted droplets resulted from the viscous and Ohmic dissipations at the cone-to-jet region[90]. This voltage deficit strongly depended on the propellant's electrical conductivity, permittivity, and viscosity while independent of the flow rate.

Figure 5.1 shows the liquid properties of higher electrical conductivity and lower surface tension coefficient with increasing temperature. A larger electric force will lead to unstable emission modes due to lower surface tension and higher conductivity at the cone-to-jet region. In Figure 5.2, simulation results are shown for heptane at $T = 280K$, $T = 300K$, $T = 320K$, $T = 340K$, $T = 360K$ with the liquid properties such as density, electrical conductivity, viscosity, and surface tension coefficient given as a function of temperature. It confirms that electrospray emission is affected by the liquid properties varying significantly in the liquid temperatures. It is, therefore, crucial to understand and control the temperature of the electrospray cone-jet and plume to investigate various emission behaviors.

The energy conservation equation in Eqs. 5.1 is applied to the finite volume model to consider the effects of varying temperatures of the cone jet. The energy equation for the cone-jet includes additional source terms than the original energy equation for a more accurate prediction of the energy of charged droplets. We considered the additional energy terms required to overcome surface tension and electrostatic repulsion, which can affect the energy of charged droplets under different operating conditions.

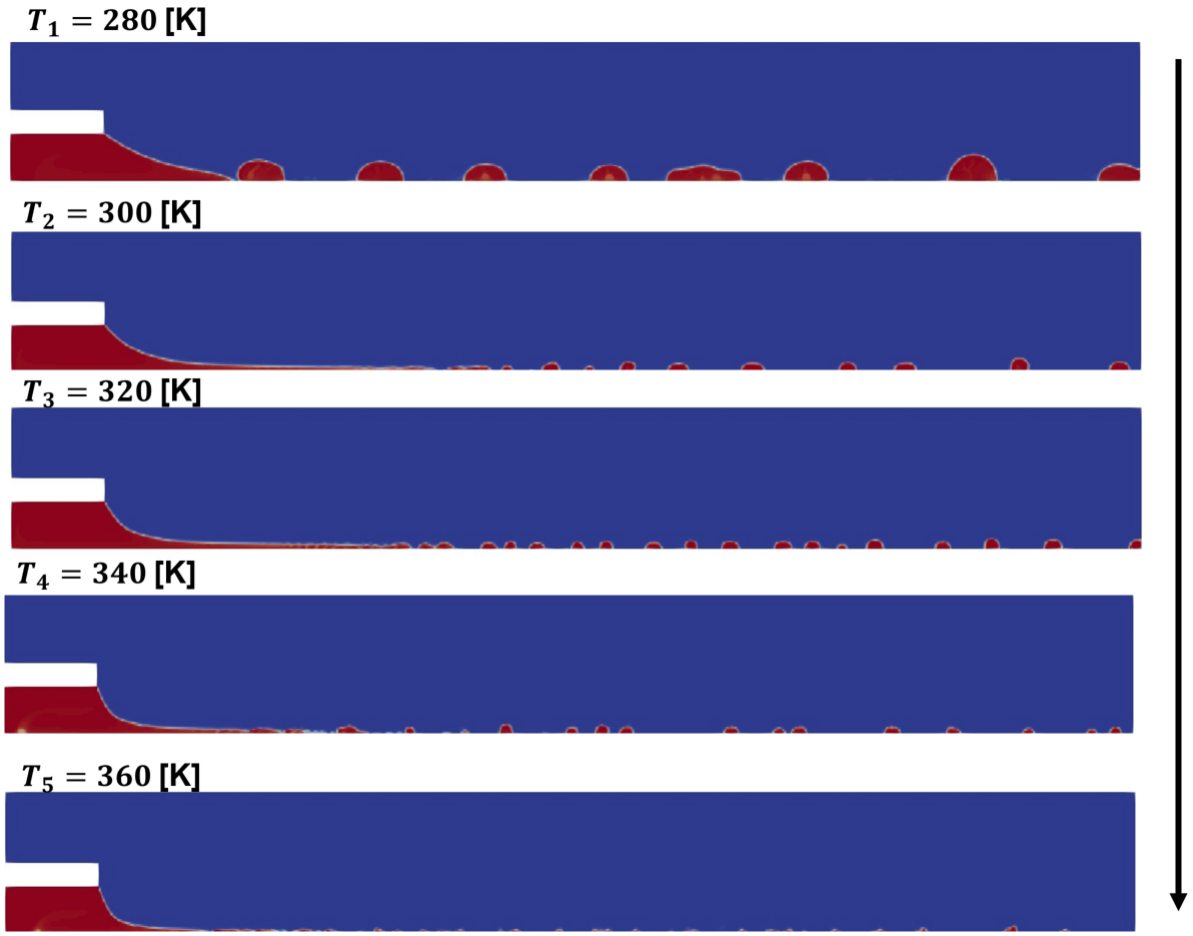

Figure 5.2: Simulation results with the liquid properties, i.e., density, electrical conductivity, viscosity, and surface tension coefficient, given as a function of the temperature at $T = 280\,\mathrm{K}$, $T = 300\,\mathrm{K}$, $T = 320\,\mathrm{K}$, $T = 340\,\mathrm{K}$, $T = 360\,\mathrm{K}$.

5.2 Model Formulation

5.2.1 Energy Equation

We solve the incompressible continuity and momentum equations coupled through the liquid properties with the energy equation given as,

$$\rho C_P \left(\left(\frac{\partial T}{\partial t} \right) + \boldsymbol{u} \cdot \nabla T \right) = \nabla \cdot (\kappa \nabla T) + \phi, \tag{5.1}$$

where T, C_p, κ, and ϕ represent temperature, specific heat, thermal conductivity, and the heat source term. The heat source term includes joule and viscous dissipation given as,

$$\phi = \phi_{Joule} + \phi_{\mu} = (\sigma \nabla V) \cdot \nabla V + (\tau : \nabla \boldsymbol{u}), \tag{5.2}$$

where σ, V, and τ are electrical conductivity, potential, and viscous tensor. To consider the liquid interface in a two-phase temperature field, the thermal conductivity, κ, is modeled by the weighted arithmetic mean (WAM) as,

$$\kappa = \alpha_{liq} \mu_{liq} \frac{Cp_{liq}}{Pr_{liq}} + (1 - \alpha_{liq}) \mu_{vac} \frac{Cp_{vac}}{Pr_{vac}}. \tag{5.3}$$

However, the WAM led to significant numerical diffusion and failed to reproduce the interface accurately, as shown in Figure 5.3. Linear interpolation in the WAM results in smoothly varying κ with significant false diffusion and energy leakage through the interface. To conserve energy, we utilized the parameter f, leading to a sharp interface of κ given as,

$$\kappa_{cell} = \left[\alpha_{liq} \left(\mu_{liq} \frac{C_{p,liq}}{Pr_{liq}} \right)^{1/f} + (1 - \alpha_{liq}) \left(\mu_{vac} \frac{C_{p,vac}}{Pr_{vac}} \right)^{1/f} \right]^{f}, \tag{5.4}$$

where κ_{cell} is the cell averaged quantity. The subscripts, liq and vac, represent liquid and vacuum, respectively. We set the ϕ_{Joule} applicable only when $\alpha_{liq} > 0.9$ to ensure an increase in temperature

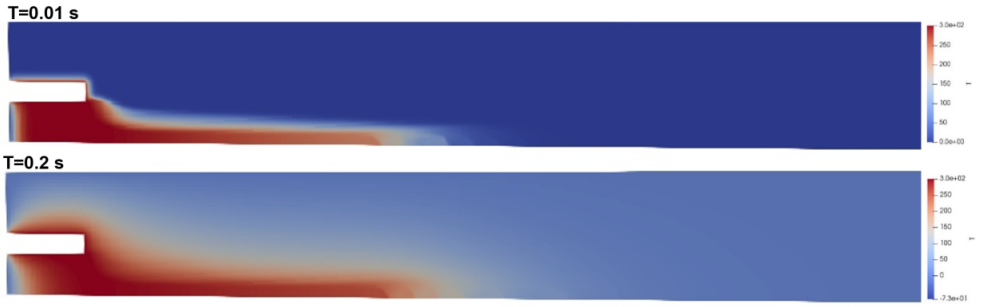

Figure 5.3: Temperature fields around the cone-jet from initially uniform 300 K at (a) $t = 0.1$ ms and (b) $t = 0.2$ ms.

only in the liquid, not at the interface with false volume fraction. Note the comparison between $f = 1$ and $f = 20$ for the results of volume fraction and temperature fields at different electrical permittivities are shown in Appendix C.

5.3 Joule Heating Effect

Joule heating or Ohmic heating is the process in which electrical current passes through a conductor and generates heat due to resistance. It is given as

$$\frac{H}{t} = I^2 R_E \tag{5.5}$$

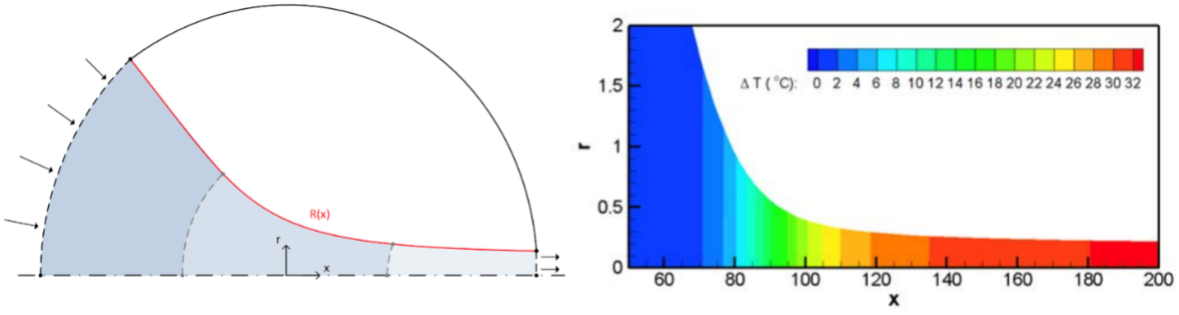

Figure 5.4: Modeling of dissipation and self-heating of the propellant at the cone-to-jet region. Figure credit from Magnani and Gamero-Castaño[13].

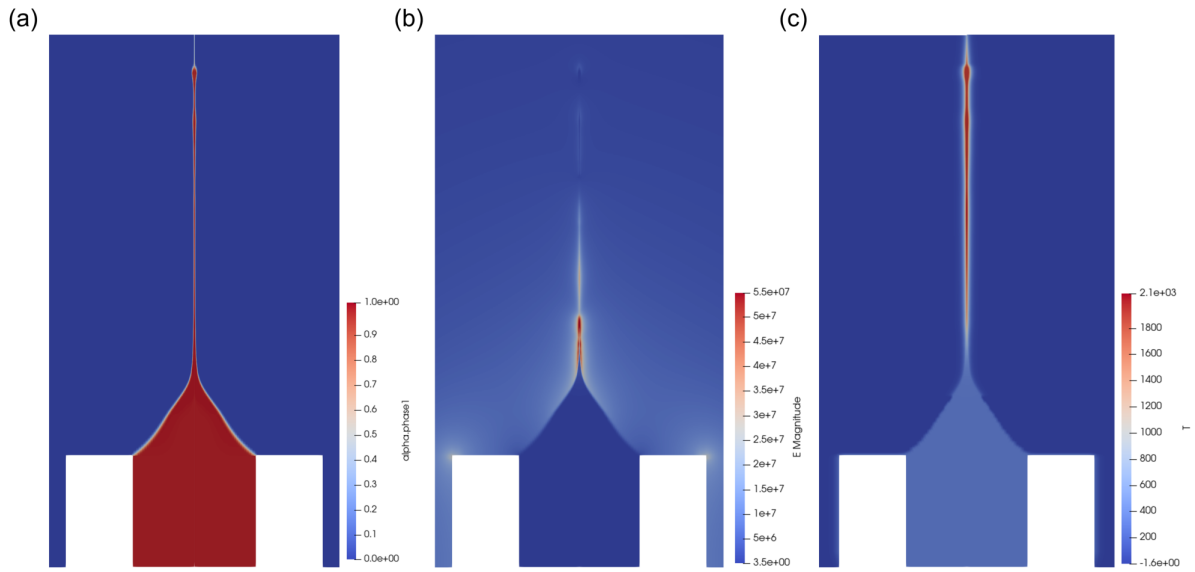

Figure 5.5: (a) Volume fraction, (b) electric field magnitude, and (c) temperature of tributyl phosphate (TBP) at $\varepsilon_r = 8.9$.

where H, t, I, and R_E represent heat production rate, time, electrical current, and electrical resistance. Joule heating can occur in the liquid cone-to-jet region where the charges are concentrated in an electrospray. As electrical current flows through a narrow liquid jet, it can heat up the liquid to result in significant changes in the fluid properties. Lower voltage and careful control of the liquid flow rate can help to reduce the Joule heating effects.

There are reports of temperature increase at the cone-to-jet region due to the Ohmic heating[90, 13]. Gamero-Castaño estimated the temperature increase of 1 K, 11 K, and 27 K at electrical conductivity, $9.47 \times 10^{-4}\,\mathrm{S\,m^{-1}}$, $0.0142\,\mathrm{S\,m^{-1}}$ for Propylene Carbonate (PC), and $0.104\,\mathrm{S\,m^{-1}}$ for Formamide (FORM) near minimum flow rate before it reaches unstable modes[90]. Magnani and Gamero-Castaño divided the computational domain into three separate regions to obtain an analytical solution under simplifying assumptions of negligible velocity upstream and two-dimensional flow downstream[13]. They reported temperature increase of 15 to 30 K at the downstream cone-to-jet region for EMI-Im ionic liquid ($0.88\,\mathrm{S\,m^{-1}}$) in Figure 5.4. Temperature increase, ΔT, predominantly takes place in the cone-to-jet region given as

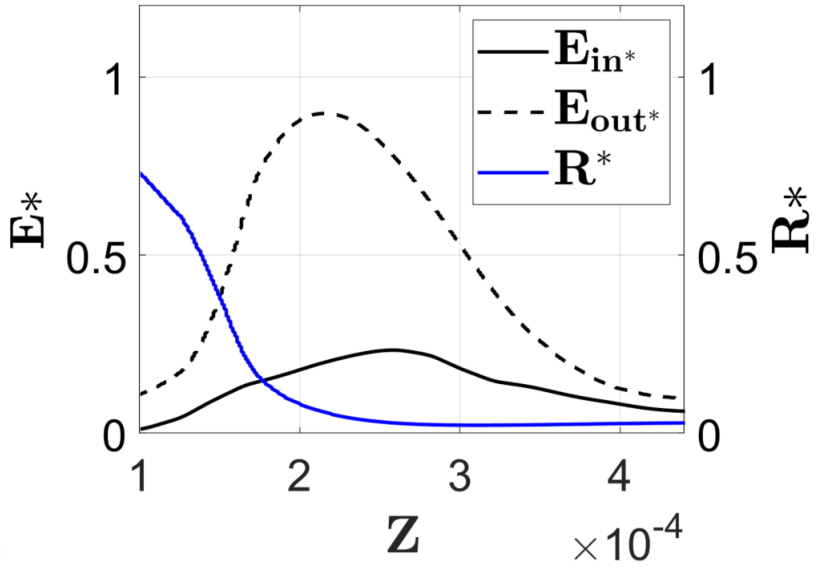

Figure 5.6: Meniscus R^* and electric field magnitude at the inner liquid and the outer meniscus of liquid.

$$\Delta T = \frac{P_\Omega + P_\mu}{\rho Q} \sim k_T \left(\frac{\mu^2 \gamma \sigma}{\varepsilon_0 Q \rho^3} \right)^{1/2} \tag{5.6}$$

where the asymptotic relation is valid at a lower electric Reynolds number, leading to a larger viscous and temperature increase[90]. P_Ω, P_μ, and k_T denote total Ohmic and viscous power dissipations and the temperature constant as a function of the dielectric constant. In Figure 5.5, volume fraction, electric field, and temperature field of steady cone-jet mode are shown for tributyl phosphate (TBP) with increased conductivity, $\sigma = 1 \times 10^{-3}\,\mathrm{S\,m^{-1}}$. Due to the high electric field at the cone-to-jet region, the propellant is heated along the jet. Since we are only interested in the cone meniscus and the cone-to-jet region, we will constrain our discussion to the cone-to-jet region where the electric field magnitude is the highest. Downstream jet past the cone-to-jet region requires additional physical consideration, such as temperature-dependent electrical properties like electrical conductivities, which will provoke ion emissions and plume interactions.

The main cause of the temperature increase is Ohmic and viscous dissipation of the propellant at the narrowing meniscus. The experiments reveal that a significant fraction of the electric power

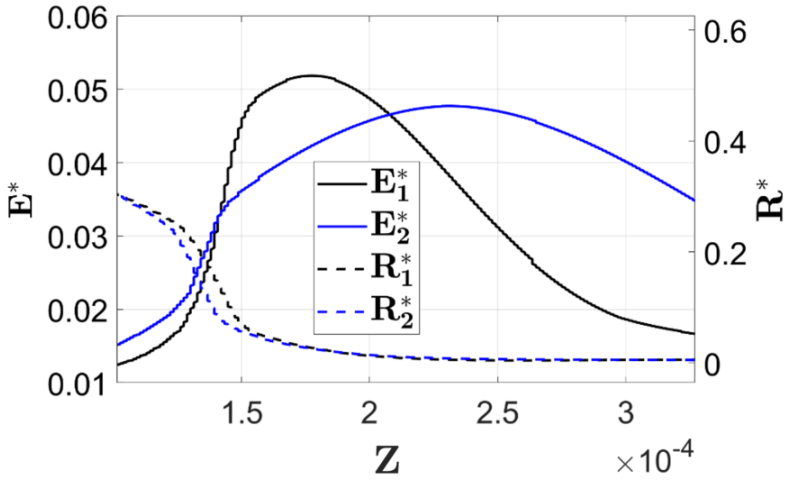

Figure 5.7: Meniscus R^* and electric field magnitude, E_1^* at $\varepsilon_r = 20$ and E_2^* at $\varepsilon_r = 50$.

is degraded by Ohimc and viscous dissipation, as well as converted into surface energy[90]. The voltage deficit, i.e., the emitter voltage minus the retarding potential of the droplets, is the amount degraded in the cone-jet and not converted into beam kinetic power[90]. According to the experimental observation, the deficit does not depend on the flow rate, where it consistently shows about 350 V, 17 % of the total electrical power, but rather strongly depends on the electrical conductivity, viscosity, and dielectric constant of the liquid[90]. The electrical current and the voltage deficit strongly depend on the dielectric constant, indicating that the charge relaxation effects are important in the cone-to-jet region[90]. Here we observed that the temperature of the liquid starts to increase at the end of the cone-to-jet region due to the dissipation predominantly taking place at the cone-to-jet region in Figure 5.5. The main cause of the Ohmic dissipation is the leaky dielectric liquid's outer and internal electric field at the cone-to-jet region and the upstream jet due to the voltage drop along the jet shown in Figure 5.6. The calculated temperature for TBP is 360 to 400 K at the downstream cone-to-jet region. In Figure 5.7, temperature is calculated at $\varepsilon_r = 20$ and $\varepsilon_r = 50$. As experimental observation indicates that the charge relaxation strongly affects the voltage deficit, permittivity change impedes the charge transport with the reduced electric field at the cone-to-jet region. The maximum calculated temperatures at the downstream cone-to-jet region are $T = 540$ K at $\varepsilon_r = 20$ and $T = 420$ K at $\varepsilon_r = 50$. The reduced electric field allows low

Ohmic heating and temperature. Note steeper meniscus is observed at $\varepsilon_r = 50$, although the electric field is high at high electrical permittivity. It is mainly because the polarization force due to high polarization results in high electrostatic force forming a steeper cone[91].

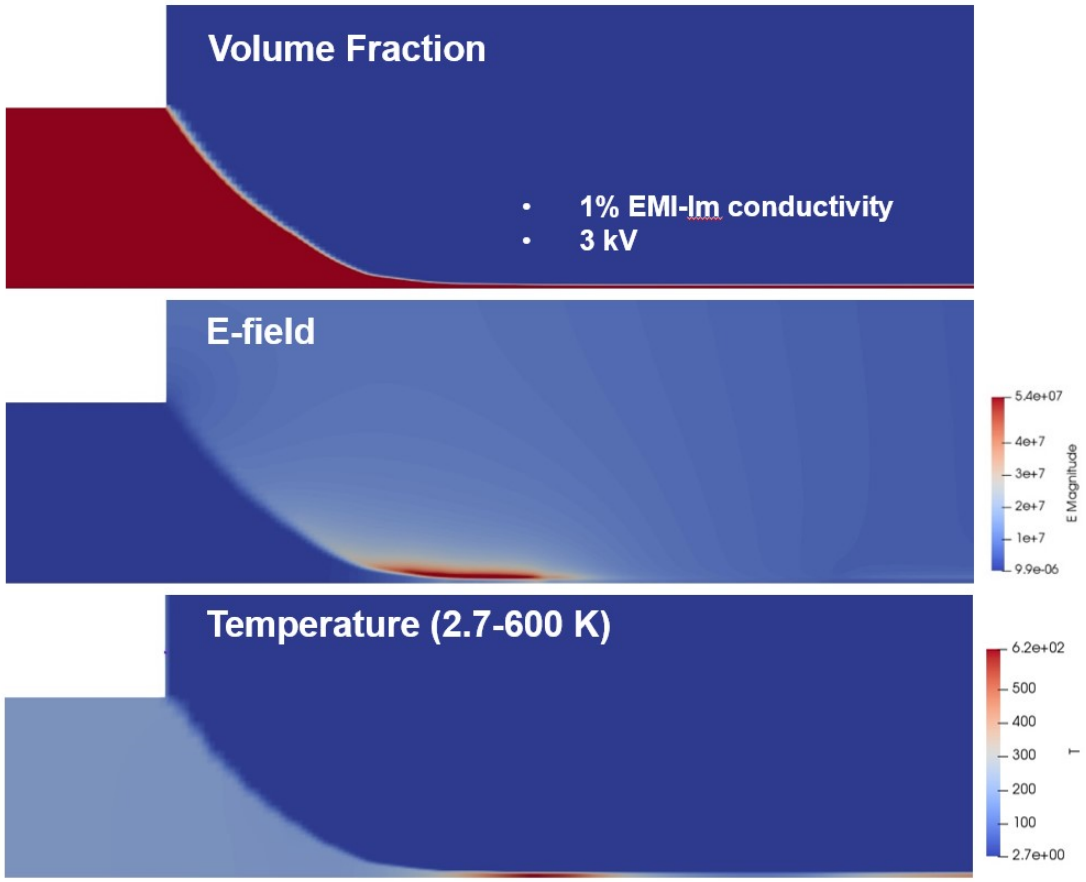

Figure 5.8: (a) Volume fraction, (b) electric field, and (c) temperature due to the Joule heating for 1% EMI-Im ($\sigma = 0.08 \times 10^{-2}\,\mathrm{S\,m^{-1}}$).

Temperatures are given from the modeling results for two different electrical conductivities, 1% ($\sigma = 0.08 \times 10^{-2}\,\mathrm{S\,m^{-1}}$) and 10% ($\sigma = 0.08 \times 10^{-1}\,\mathrm{S\,m^{-1}}$) EMI-Im in Figure 5.8 and Figure 5.9. Due to the Joule heating with no ionization, the temperature increased to 620 K for 1% EMI-Im and 1400 K for 10% EMI-Im at the cone-to-jet region. We acquired the temperature increase due to Joule heating for both conductivities and concluded that the phenomena were caused by the inner electric field in the liquid jet. Several researchers report the existence of the internal electric field due to the potential drop along the longitudinal axis in the liquid jet.

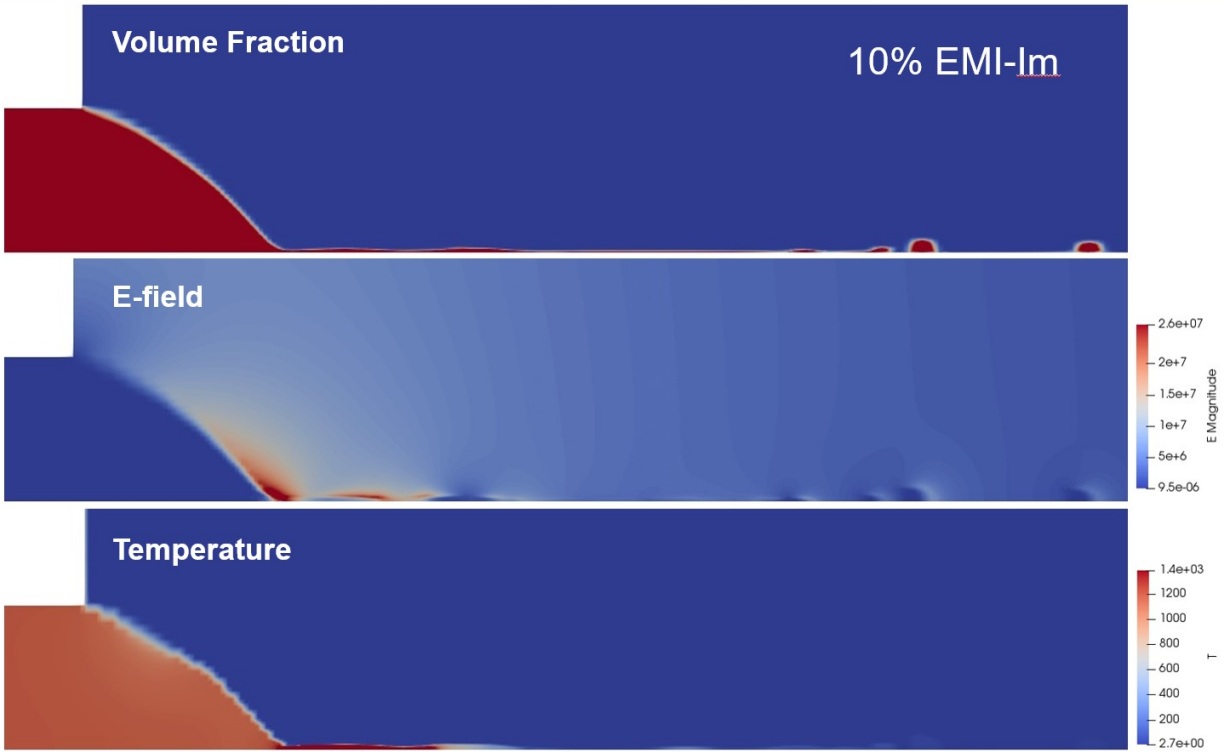

Figure 5.9: (a) Volume fraction, (b) electric field, and (c) temperature due to the Joule heating for 10% EMI-Im ($\sigma = 0.08 \times 10^{-1}\,\mathrm{S\,m^{-1}}$).

CHAPTER 6

Asymmetric Tilted-Cone Jet Emission

6.1 Motivation: Electrospray Overspray

Electrospray is an EHD emission process where bulk liquid forms a cone meniscus, leading to the formation of a jet, droplets, and/or ions under the influence of an externally applied electric field. Numerous studies have been conducted experimentally on the emission modes of electrospray in the past decades[33, 34, 92]. Zeleny first observed the emission modes of electrospray, Cloupeau & Prunet-Foch examined various cone-jet structures and operating modes of different operating conditions and physical properties[33, 34] such as simple, skewed, ramified, and multi-jets. Rosell-Llompart *et al.* categorized emission modes as increasing the electrical Bond number with respect to the Weber number[92]. At a lower Weber number ($We \ll 1$), unsteady modes such as electro-dripping, spindle, and intermittent cone-jet mode are present with strong cohesion force. At a higher Weber number ($We \gg 1$), steady axisymmetric simple and varicose jetting modes are present. Further increasing the electrical Bond number ($B_E \gg 1$) grants asymmetric whipping mode where the jet undergoes lateral displacement, which gets amplified in the flow, resulting in irregular whipping patterns[92].

One of the significant life-limiting concerns in electrospray thrusters is the propellant flux to the downstream electrodes, known as grid impingement[93, 15, 16]. Off-axis emission contributes to this flux along with the plume expansion as droplets are emitted at a large angle from the emitter axis. The tilted cone emission mode involves the angle of emission tilted from its normal orientation in an electrospray. There were reports on an off-axis cone and jet tilt behavior with increasing

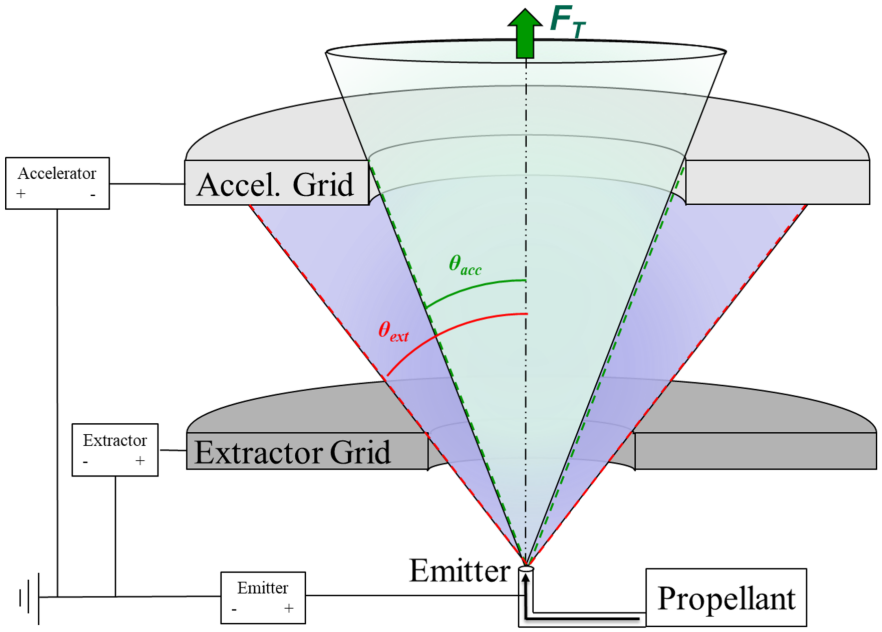

Figure 6.1: Primary failure mechanism: Overspray leading to grid impingement[14, 15, 16]. Figure credit from Thuppul *et al.*[14]

electrical potential of the emitter in numerous experiments. Lee *et al.* identified experimentally asymmetric tilted jet emission and the voltage-flow rate sensitivity map for various liquid mixtures, where the flow was stabilized with the increasing proportion of terpineol or the decreasing ratio of electrical conductivity to surface tension coefficient. More recently, Uchizono *et al.* observed steady tilted cone jet emission of a high conductivity ionic liquid 1-ethyl-3-methylimidazolium bis(trifluoromethyl sulfonyl)imide (EMI-Im)[10]. The tilted (or skewed) emission occurs in the transition between cone-jet and multi-jet modes, in which tilted cone and jet emerge as the applied emitter voltage is above the potential required for the steady cone-jet mode[10]. The emitter voltage increasing from 1.3 kV to 2.0 kV led to increasing the angle of the conical meniscus with respect to the ideal thrust axis. Ultimately, further increasing the voltage leads to dual and multi-jet emission modes[19, 94, 34].

Several potential factors are reported to cause the tilted cone jet, such as emitter imperfections leading to asymmetric emitter wetting and asymmetries in the electric field surrounding the Taylor

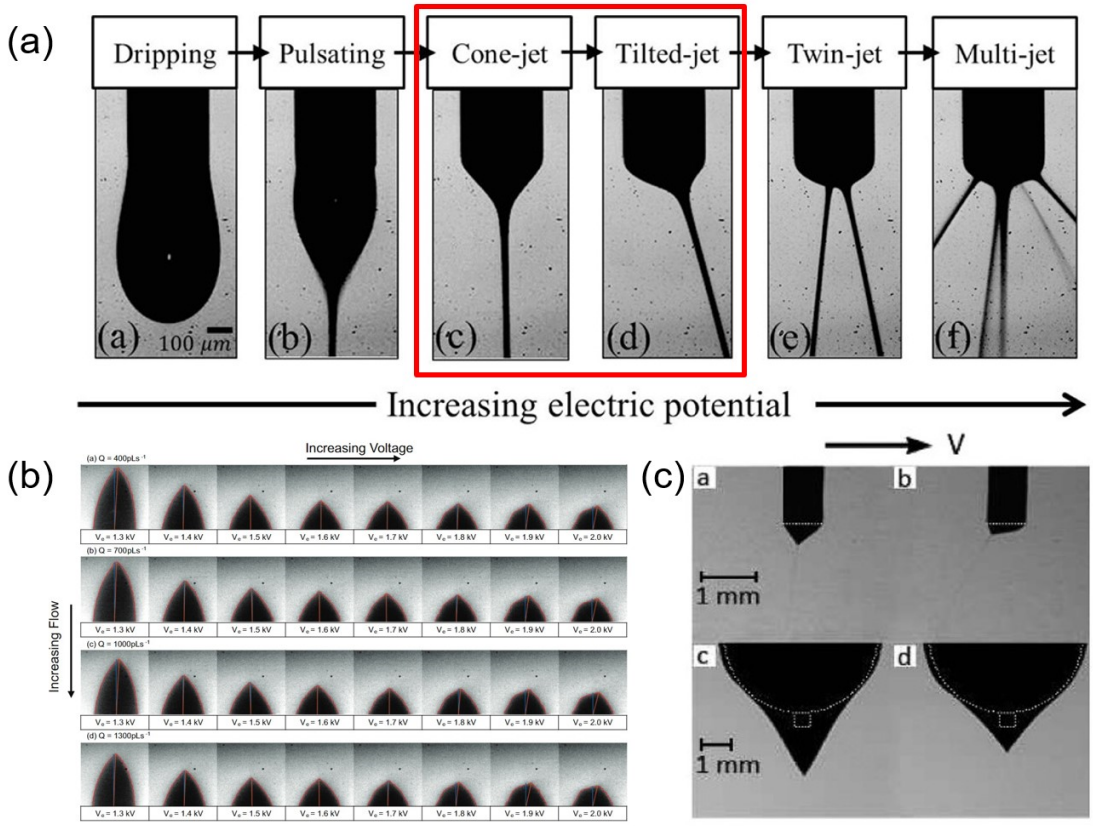

Figure 6.2: (a) Photographs of various emission modes at increasing electrical voltage. Figure credit from Lee *et al.*[17] (b) Images of the EMI-Im electrospray emission site with flow setpoints between 400 $\mathrm{pL\,s^{-1}}$ and 1300 $\mathrm{pL\,s^{-1}}$, and emitter voltage setpoints from 1.3 kV to 3.0 kV. The blue line indicates the center axis of the capillary, and the orange line indicates the angle of the cone's apex with respect to the center axis. Figure credit from Uchizono *et al.*[10] (c) Asymmetric cone-tilt emission using a simple nozzle and the axisymmetric steady cone-jet using an extender cap. Figure credit from Morad *et al.*[18]

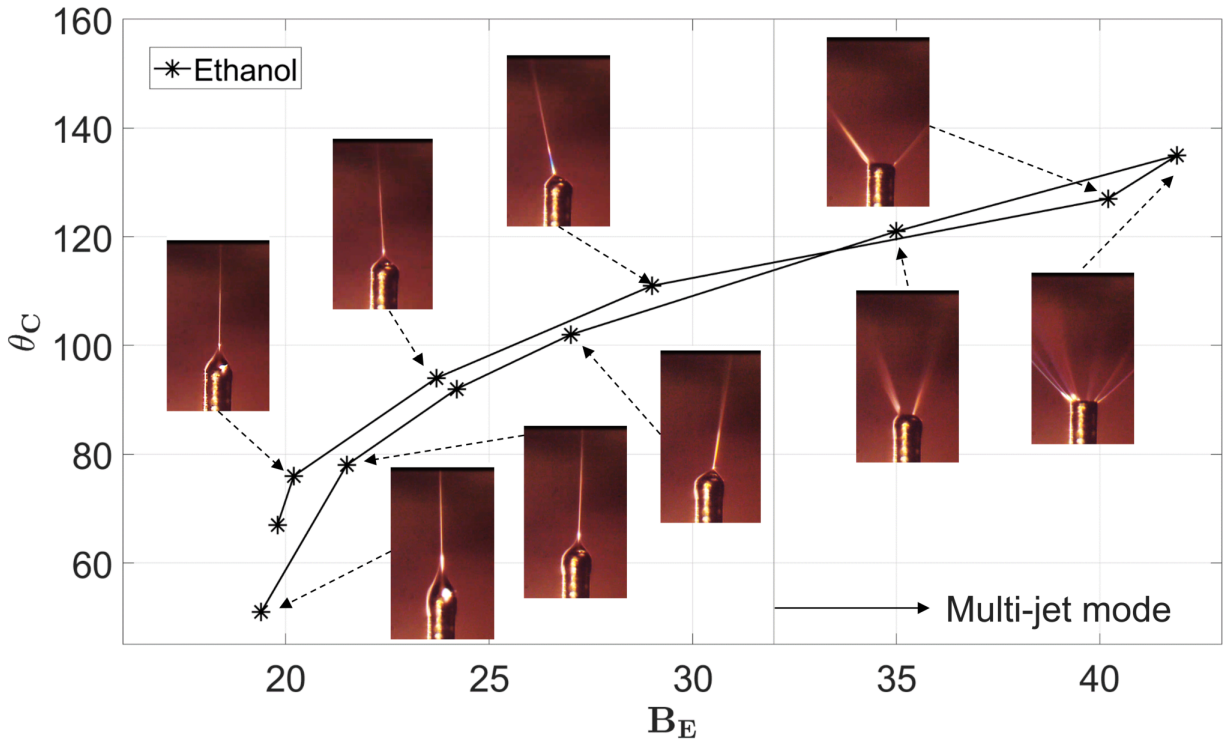

Figure 6.3: Cone angles at varying electrical Bond number, B_E, and the photographs of steady emission modes for each setpoint using ethanol. The experimental apparatus is detailed in Wright *et al.*[19]

cone[95]. N. Sochorakis *et al.* reported that the imperfections of both inner and outer emitter morphology may lead to asymmetric hydrodynamics and wetting conditions to cause tilted cone-jet[95]. Also, the emitter misalignments led to the distortion of the electric field, resulting in the asymmetric jet directions in the multiple emitter array[95]. However, the experiment does not resolve why the tilted cone jet occurs without misalignment in the array. Since the mechanistic description of the tilted cone-jet emission of the single emitter is still missing in the experimental observations, it is appropriate to investigate the asymmetric emission phenomena through a three-dimensional numerical EHD model extended from Huh and Wirz[91].

The objective of this study is to use a three-dimensional EHD model that can provide a detailed emission mechanism of a transition from the axisymmetric steady cone jet to the asymmetric tilted cone jet. Results are validated against experimental observations in various operating conditions in Section 6.2.1. We will then investigate the modeling results by comparing axisymmetric cone-jet and asymmetric tilted cone for different liquid properties in Section 6.2.2. Sensitivity analysis on varying electrical permittivity will be performed to show how meniscus shape and associated charge density and electric field changes at the cone-to-jet region in Section 6.3. The transition from jet breakup to Whipping emission will be investigated at varying electrical permittivity in Section 6.4.

6.2 Tilted-Cone Emission

The three-dimensional axisymmetric EHD Finite Volume Method (FVM) model was extended from the two-dimensional axisymmetric EHD solver developed by Huh and Wirz[91]. The 2^{nd}-order-accurate linear upwind scheme suppresses false diffusion due to the discretized convection term[65, 66]. As the velocity boundary conditions, a fixed constant value is applied at the inlet, the zero-gradient condition at the outlet, and the wall. Similarly, as the pressure boundary condition, the zero-gradient is applied at the inlet and zero total pressure at the outlet and the wall to maintain a vacuum in the domain.

Liquids	$\rho(kg/m^3)$	$\sigma(S/m)$	$\gamma(N/m)$	$\varepsilon(F/m)$	$\nu(m^2/s)$
Ethanol	789	5×10^{-5}	0.02	22.5	3×10^{-6}
E2T8	909	1.5×10^{-6}	0.0315	9.2	1.49×10^{-5}

Table 6.1: Liquid properties of ethanol and ethanol and terpineol mixture.

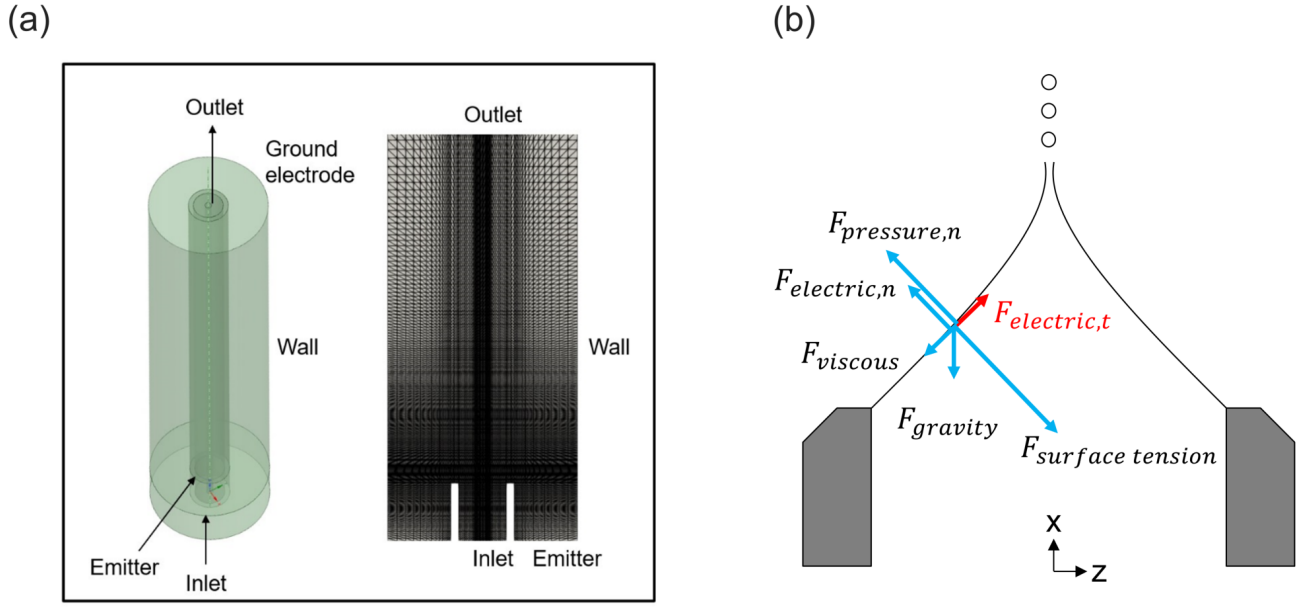

Figure 6.4: (a) Computational domain, (b) normal and tangential forces acting on the liquid meniscus.

6.2.1 Jet Diameters and Validation

$$D = \left(\frac{\rho\varepsilon_0 Q^3}{\sigma\gamma}\right)^{\frac{1}{6}}, \tag{6.1}$$

Simulation is based on the experimental setup and operating condition, including flow rate and voltage in Lee *et al.*[17] with the given physical properties of 20% ethanol and 80% terpineol mixture, E2T8. Relevant liquid properties of E2T8 are listed in Table 6.1, and other mixtures are listed in Appendix A. The three-dimensional domain covers the region from emitter to extractor and is constructed by the meshing software ANSYS-ICEM in Figure 6.4(a) and also shown in Ap-

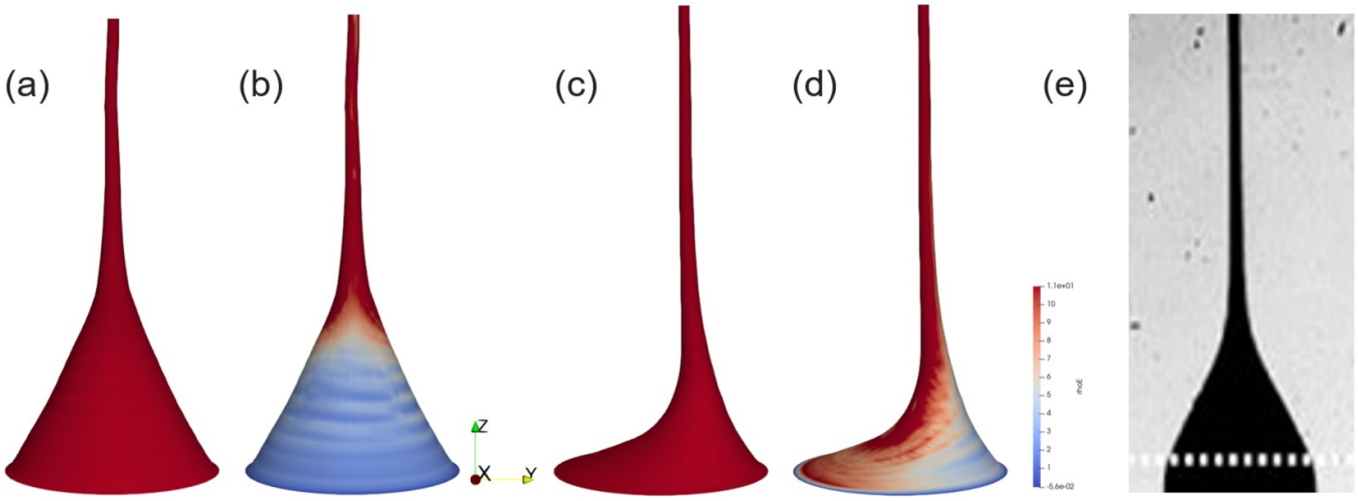

Figure 6.5: (a) Volume fraction, (b) charge density of the steady axisymmetric cone-jet at $B_E = 66$, (c) volume fraction, (d) charge density of the steady asymmetric tilted cone at $B_E = 126$, and (e) photograph of the steady cone-jet for E2T8 at $B_E = 66$. Figure credit from Lee *et al.*[17]

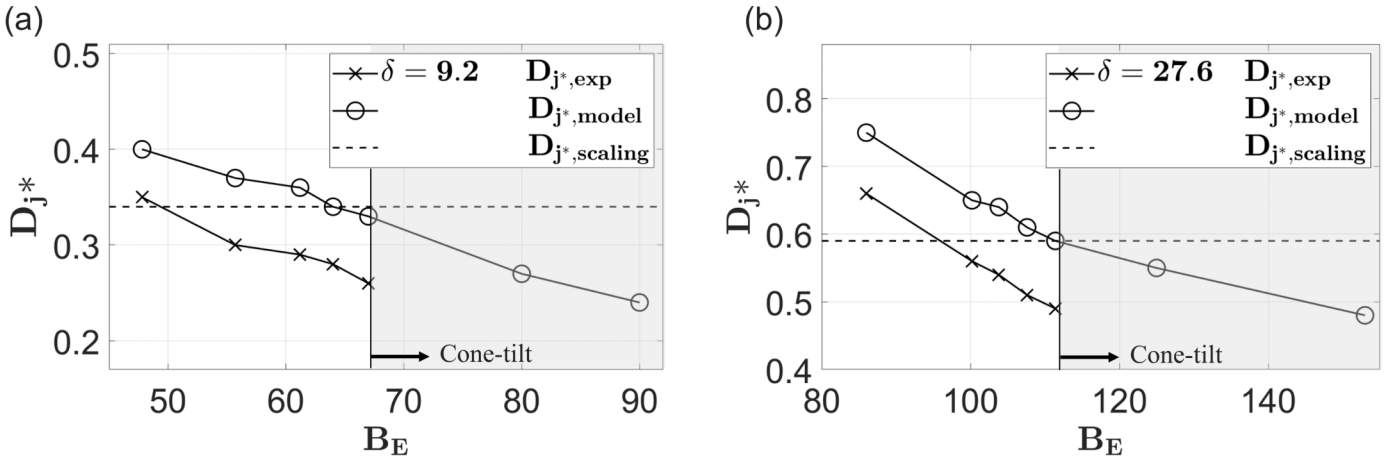

Figure 6.6: Dimensionless jet diameters, D_{j^*}, by experiment, modeling, and scaling law for E2T8 at different B_E at (a) $\delta = 9.2$ and (b) $\delta = 27.6$.

pendix D. Normal and tangential forces acting on the liquid meniscus are depicted in Figure 6.4(b), where the electrostatic force and the liquid pressure balance the concave-outward surface tension in the normal direction and the tangential electrostatic force balances the viscous force in the tangential direction.

Figure 6.6(a-b) show the calculated volume fraction and charge density distribution of the steady axisymmetric cone-jet, which are in good agreement with the experimental observations at $B_E = 66$ in Figure 6.6(e)[17]. Further increasing in B_E disturbs the axisymmetric balance to result in a steady tilted cone-jet at $B_E = 126$ in Figure 6.9(c-d). The scaling relationship is derived by Gañán Calvo in Eq. 6.1. The jet diameter decreases with increasing B_E due to high tangential electric forces for both flow rates, $\delta = 9.2$ and $\delta = 27.6$. Although the scaling is given as a function of the flow rate and physical properties only, the jet diameter strongly depends on the electric Bond number at the higher flow rate, $\delta = 27.6$, as discussed in the past studies[17, 5, 91]. Further increase of B_E over 67 at $\delta = 9.2$ and 112 at $\delta = 27.6$ result in the tilted cone-jet emissions due to the breakdown of the symmetric balance of the driving forces at the cone-to-jet region.

6.2.2 Electric Bond Number Sensitivity

Electrostatic forces at the liquid meniscus are shown with B_E increasing from 66 to 126 in Figure 6.7(a). The concentrated charge results in the highest electrostatic force at the cone-to-jet region, where the convective current changes from 5 % to 95 % of its final value[91] in Figure 6.7(b). The higher tangential electrostatic force, F_E, t, results in a steeper meniscus with a higher cone angle at the region. After reaching critical B_E, the force balance does not hold for F_E larger than the opposing surface tension and viscous forces to result in tilted cone emission at the cone-to-jet region. Note the scaling for $\frac{F_{E,n}}{F_{E,t}}$ agrees well with previous studies[39, 41]. In Figure 6.8, (a) axisymmetric steady cone-jet emission develops into (b) steady tilted cone-jet mode with a more skewed cone shape as increasing B_E for ethanol. The steady-state emission results suggest that the skewed cone shape achieves an equal balance between forces acting at the liquid meniscus. The results were obtained with increasing emitter voltage from 1 kV to 1.3 kV at a constant flow

rate, suggesting a lateral perturbation due to geometrical asymmetries growing with the increasing electrical stresses. Decreasing back to 1 kV results in axisymmetric steady cone-jet mode. The experimental apparatus is detailed in Wright *et al.*[19] Note the regime map of EHD stability for ethanol, and the computed results are shown in Appendix E.

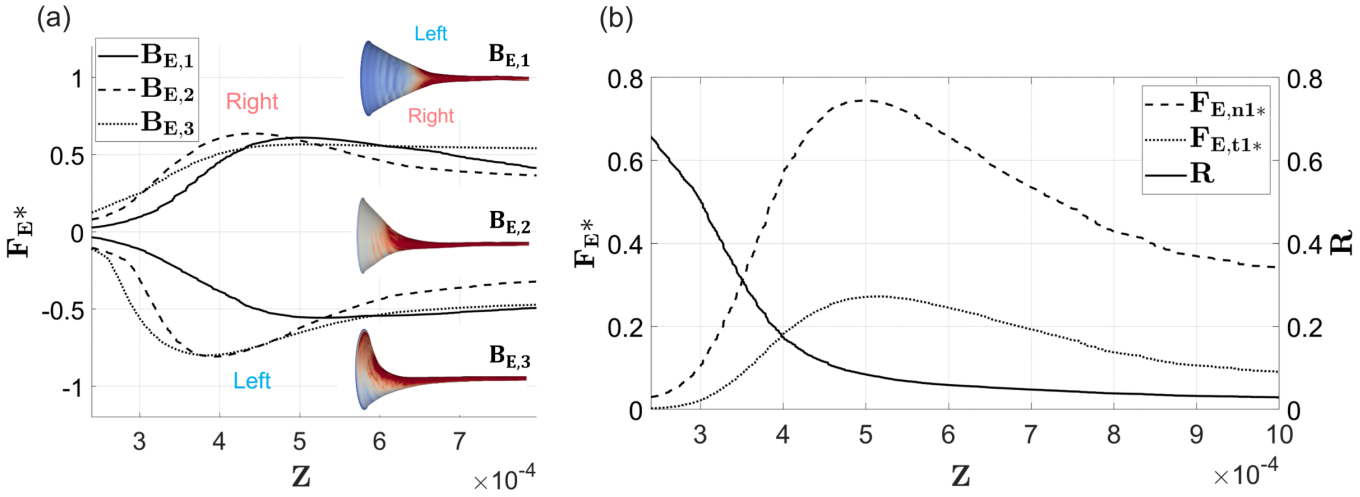

Figure 6.7: (a) Electrostatic forces along the z-axis, $F_{E,1*}$ at $B_E = 66$, $F_{E,2*}$ at $B_E = 76$, and $F_{E,3*}$ at $B_E = 126$. (b) Normal and tangential electrostatic forces, and the radius of the cone, R, along the Z-axis for $F_{E,1*}$ at $B_E = 66$.

Transient evolution is shown to reach the steady-state tilted cone emission under axisymmetric boundary conditions in Figure 6.9(a). Perturbation starts to grow at 0.25 ms in Figure 6.9(d) when the tangential electrostatic force increases to accelerate the liquid interface dilating and tilting the cone and the jet at the cone-to-jet region of high charge concentration. At 0.3 ms in Figure 6.9(e), the high tangential force at the cone-to-jet region begins to deform the cone upstream and introduces charge at the dilated surface with a smaller radius of curvature. The charge's tangential component of the electrostatic repulsion at the flattest surface is the greatest, resulting in higher charge concentration to the surface with smaller radius curvature. According to Gauss's law, since the electric field is normal to the interface, concentrated electric field lines at the dilated surface apply high electrostatic force. When electrostatic force balances the surface tension and viscous force, the emission reaches a steady state through (f-h). In Figure 6.10, the meniscus shape, the

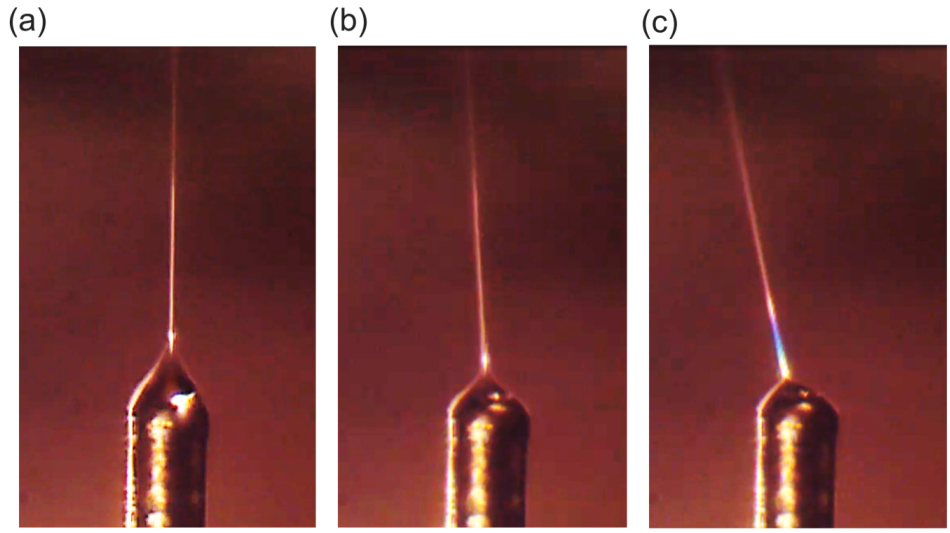

Figure 6.8: (a) Axisymmetric steady cone-jet emission at $B_E = 20.2$, (b) asymmetric tilted cone-jet emission at $B_E = 23.7$, and at (c) $B_E = 29$ for ethanol.

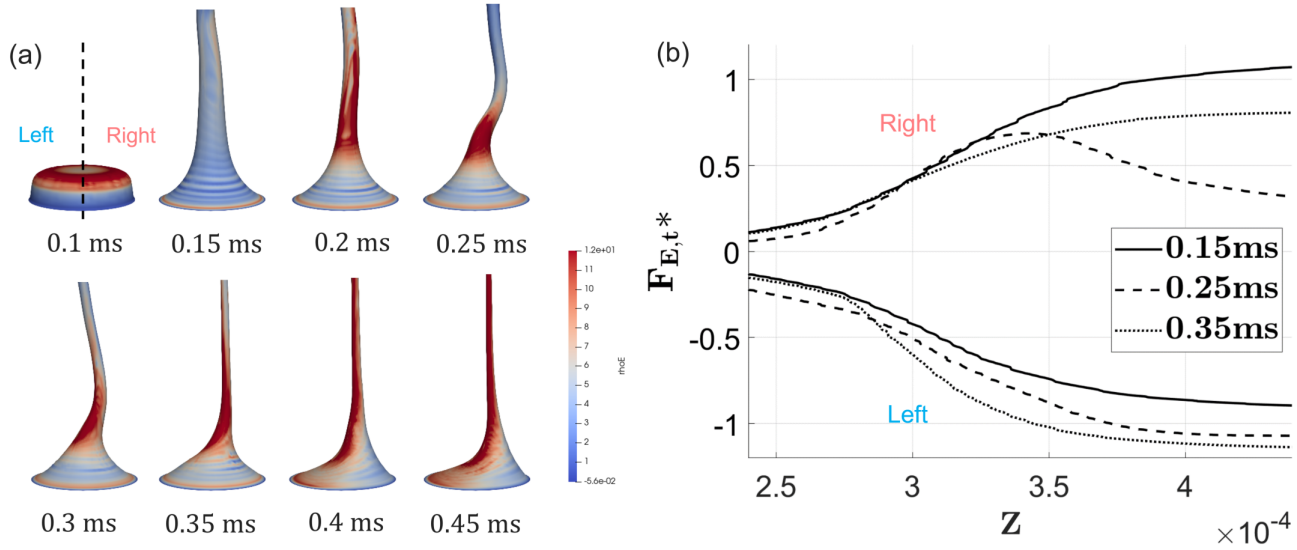

Figure 6.9: Transient evolution to achieve the steady-state tilted cone at (a) 0.1 ms, (b) 0.15 ms, (c) 0.2 ms, (d) 0.25 ms, (e) 0.3 ms, (f) 0.35 ms, (g) 0.4 ms, (h) 0.45 ms, and (i) magnitudes of tangential electrostatic force at $t_b = 0.15$ ms, $t_d = 0.25$ ms, $t_f = 0.35$ ms.

electrostatic force, and the electric field magnitudes are shown at $B_E = 66$ and $B_E = 126$ of the selected plane with the most variance. At $B_E = 126$, the high electrostatic force on the left side of the meniscus tilts the cone and the jet to the positive X-axis. In Figure 6.10(d), the normal directional

electric field magnitude at the left side of the liquid interface is higher than that of the right side, whereas the tangential field magnitudes are equivalent. This electrical field jump condition across the interface in the normal direction describes the high charge concentration on the left meniscus according to Eq. 3.15.

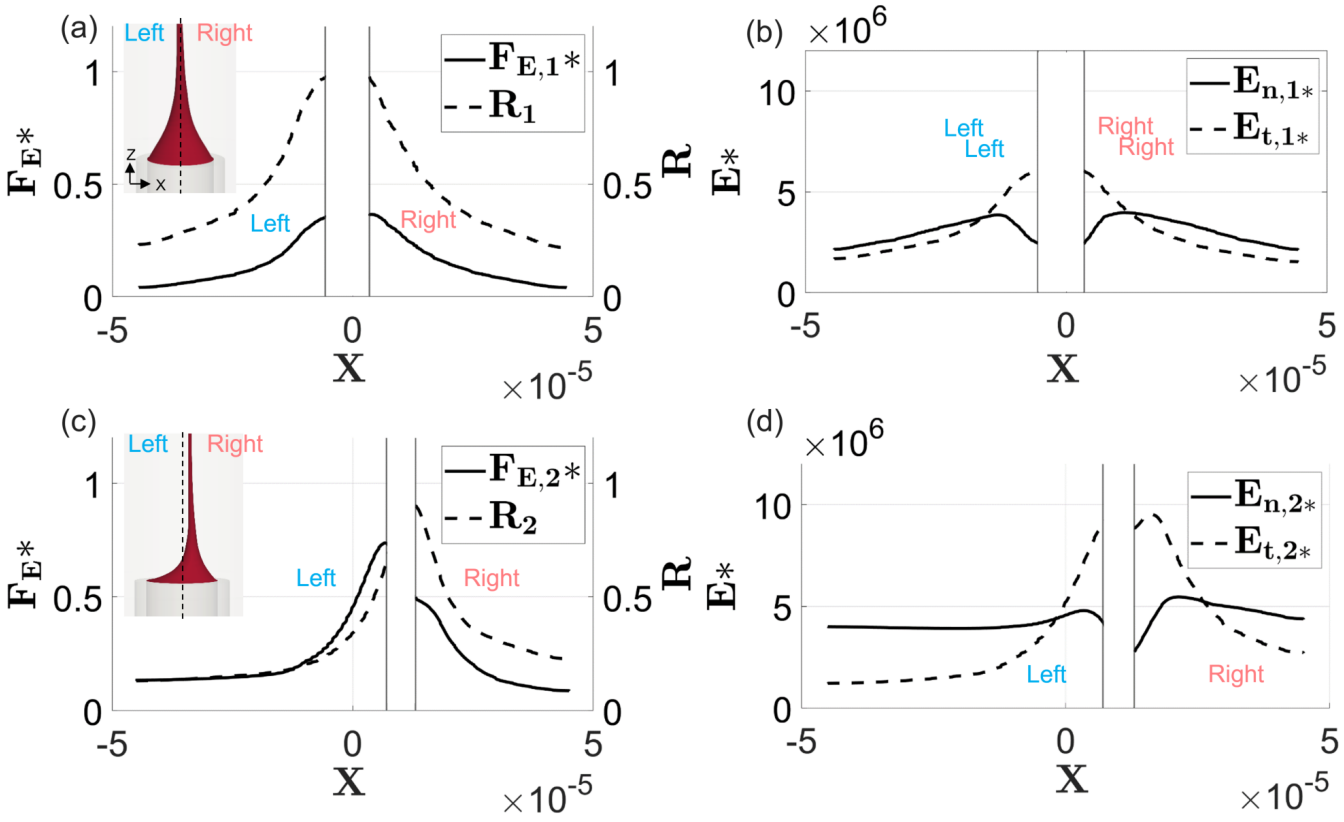

Figure 6.10: Radius of the cone, the magnitudes of resultant electrostatic force, normal and tangential electric field along the meniscus for (a,b) $B_E = 66$ and (c,d) $B_E = 126$.

In Figure 6.11, surface tension, $F_{\gamma,n}$, viscous, $F_{\mu,n}$, pressure, $F_{p,n}$, and electrostatic force, $F_{E,n}$, balance in the normal direction along the longitudinal axis in the Z-X plane, indicating the results are steady-state. The higher $F_{E,n}$ due to high charge concentration allows the dilated surface at the left meniscus in Figure 6.11(a), leading to the higher $F_{\gamma,n}$ than that of the right meniscus in Figure 6.11(b).

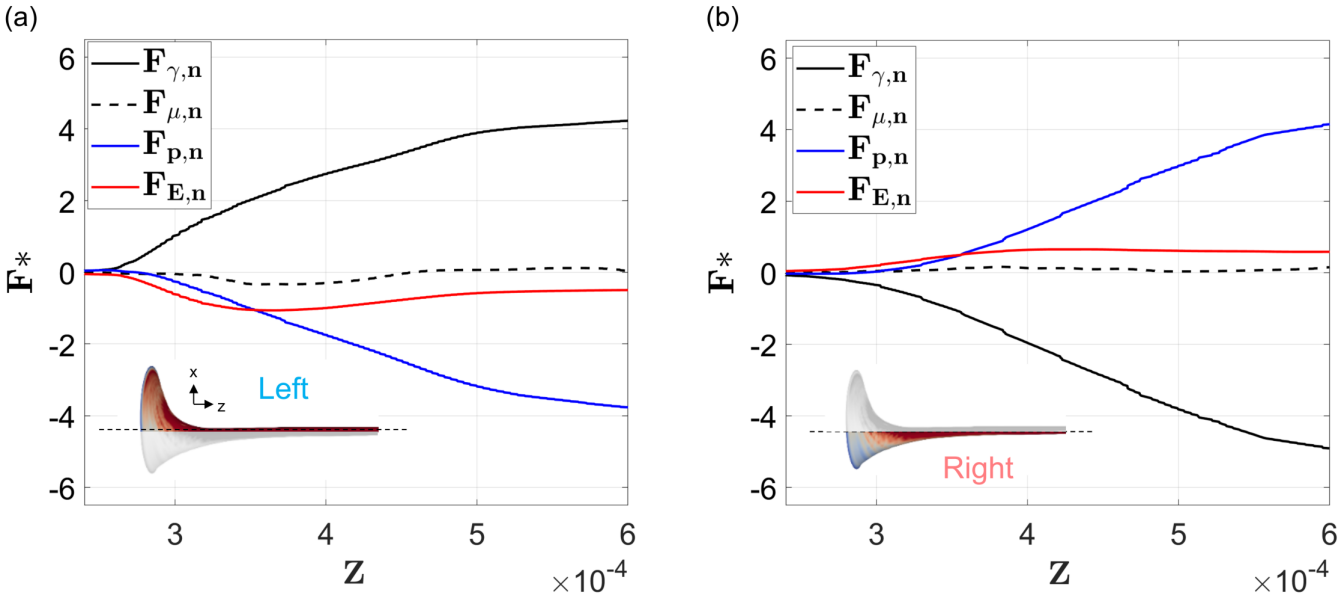

Figure 6.11: Surface tension force, $F_{\gamma,n}$, viscous force, $F_{\mu,n}$, pressure force, $F_{p,n}$, and electrostatic force, $F_{E,n}$, in the normal direction along the Z-axis at $B_E = 126$ for meniscus on (a) left and (b) right.

6.3 Electrical Permittivity Effect

The normal and tangential electric fields at the liquid meniscus for $\varepsilon_r = 9.2$ are compared to those of $\varepsilon_r = 20$ in Figure 6.12. Note that both the results are steady-state axisymmetric cone-jet mode emissions. Increasing the permittivity enhances charge relaxation time, resulting in higher polarization of the material, reducing the effective electric field. At $\varepsilon_r = 20$, the average charge density in the cone-to-jet region is about 70 % of that at $\varepsilon_r = 9.2$. $\frac{E_{n,2}}{E_{n,1}} \sim 0.7$ confirms the electric field jump condition at the meniscus in the normal direction. Increasing permittivity allows reduced charge density, leading to larger jets and emitted droplets[91, 39]. Although high permittivity leading to high charge relaxation decelerates the charge transport, increased polarization force allows high $F_{E,n}$ as shown in Figure 6.13. The results are axisymmetric cone-jet mode emission, and the forces are counterbalancing, which implies the emissions are steady-state. High $F_{E,n}$ results in a steeper meniscus with the reduced surface tension, F_γ. Also, reduced opposing pressure, F_p, correlates with the lower electrostatic suction due to lower charge concentration resulting in higher jet diam-

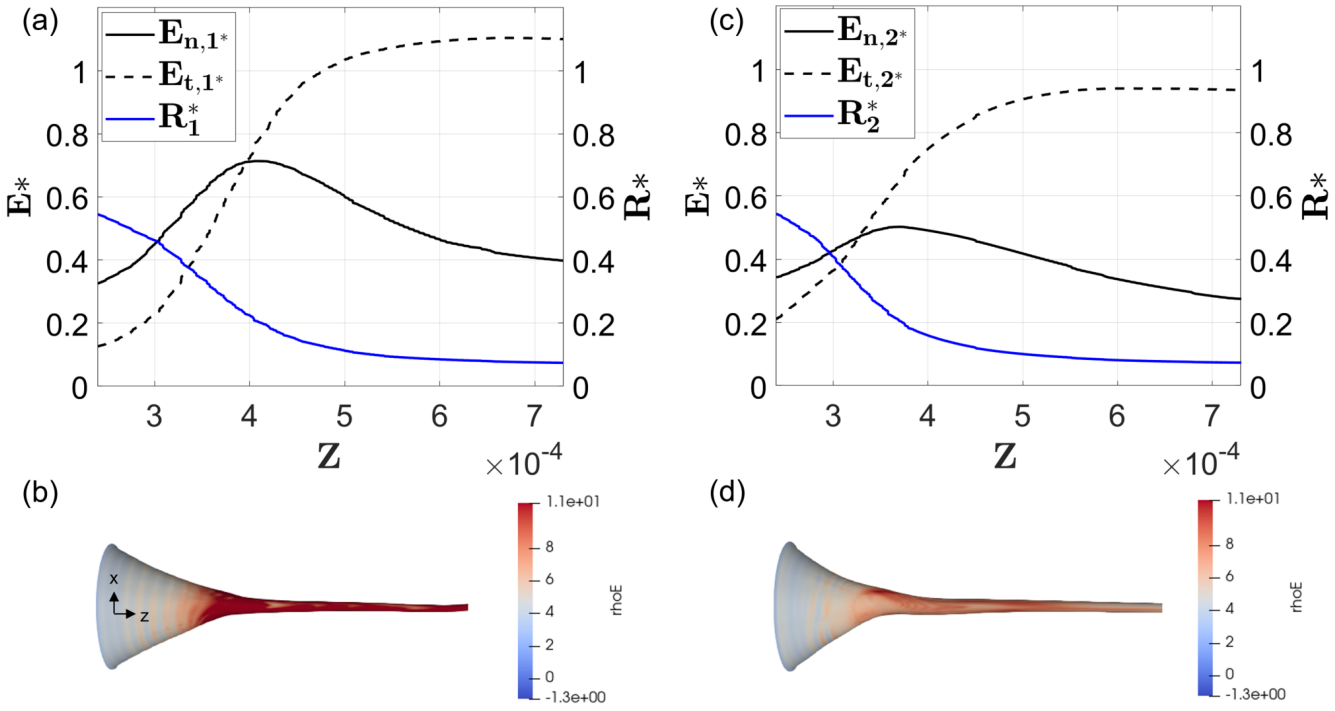

Figure 6.12: Radius of the cone, R^*, magnitude of normal electric field,E_n, magnitude of tangential electric field,E_t, and surface charge density at $B_E = 61$ for (a,b) $\varepsilon_{r,1} = 9.2$ and (c,d) $\varepsilon_{r,2} = 20$.

eters. Note the normal directional viscous force, $F_{\mu,n}$, is negligible everywhere. In Figure 6.14, the jet diameters for $\varepsilon_{r,2} = 20$ increased the jet diameters about 30 % where the scaling for the jet diameter remains at $D_j^* = 0.34$ for $B_E = 61$. It is consistent with the reduced total current for higher permittivity studied by Gamero-Castaño and Magnani, where increasing permittivity grants higher electric relaxation impeding the charge transport[39]. Also, increasing permittivity results in higher $\frac{F_{E,n}}{F_{\gamma,n}}$ at the cone-to-jet region, which easily tilts the cone. In Figure 6.14, the cone tilts at $B_E = 72$ for $\varepsilon_{r,2} = 20$ whereas $B_E = 89$ for $\varepsilon_{r,2} = 9.2$. Note the permittivity effect on meniscus shape, and the resultant electrostatic force weakens as the conductivity increases[91].

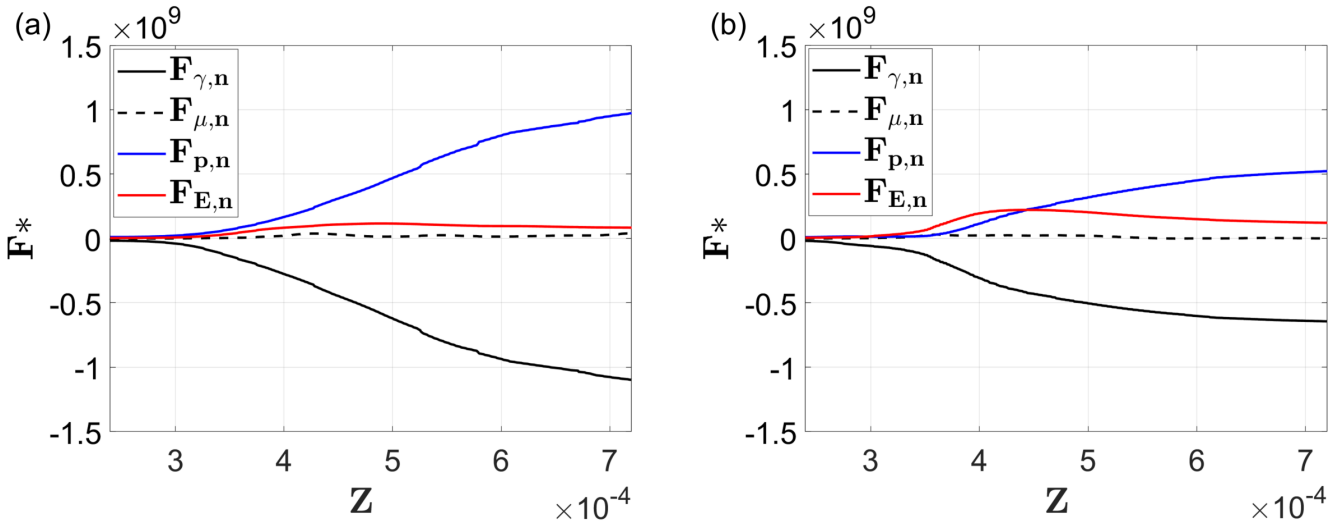

Figure 6.13: Surface tension force, $F_{\gamma,n}$, viscous force, $F_{\mu,n}$, pressure force, $F_{p,n}$, and electrostatic force, $F_{E,n}$, in the normal direction along the Z-axis at $B_E = 61$ for (a) $\varepsilon_{r,1} = 9.2$ and (b) $\varepsilon_{r,2} = 20$.

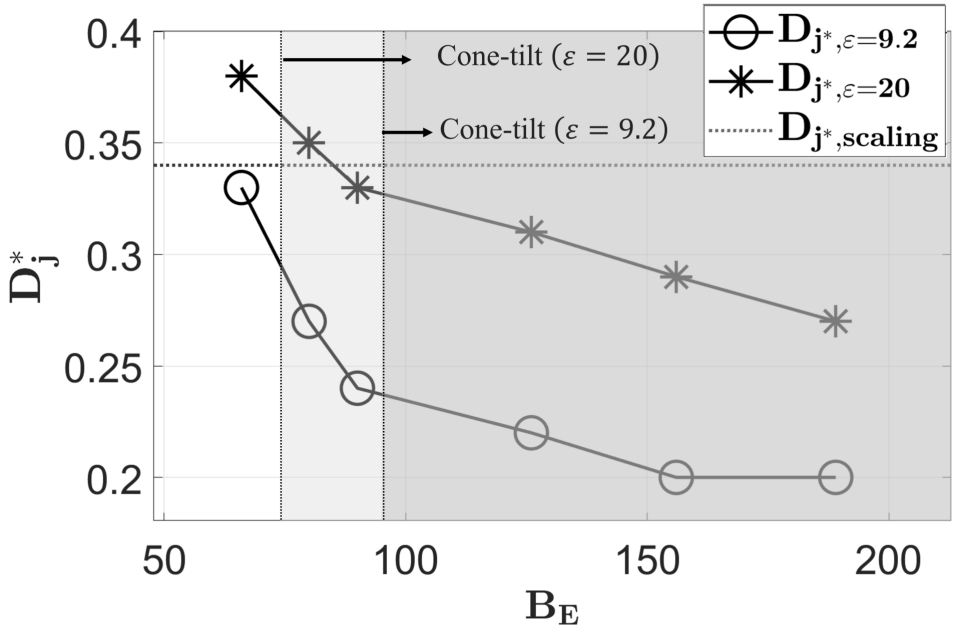

Figure 6.14: Jet diameters, D_j^*, with respect to B_E by calculation and the scaling law for $\varepsilon_{r,1} = 9.2$, $\varepsilon_{r,2} = 20$.

6.4 Whipping Jet Emission

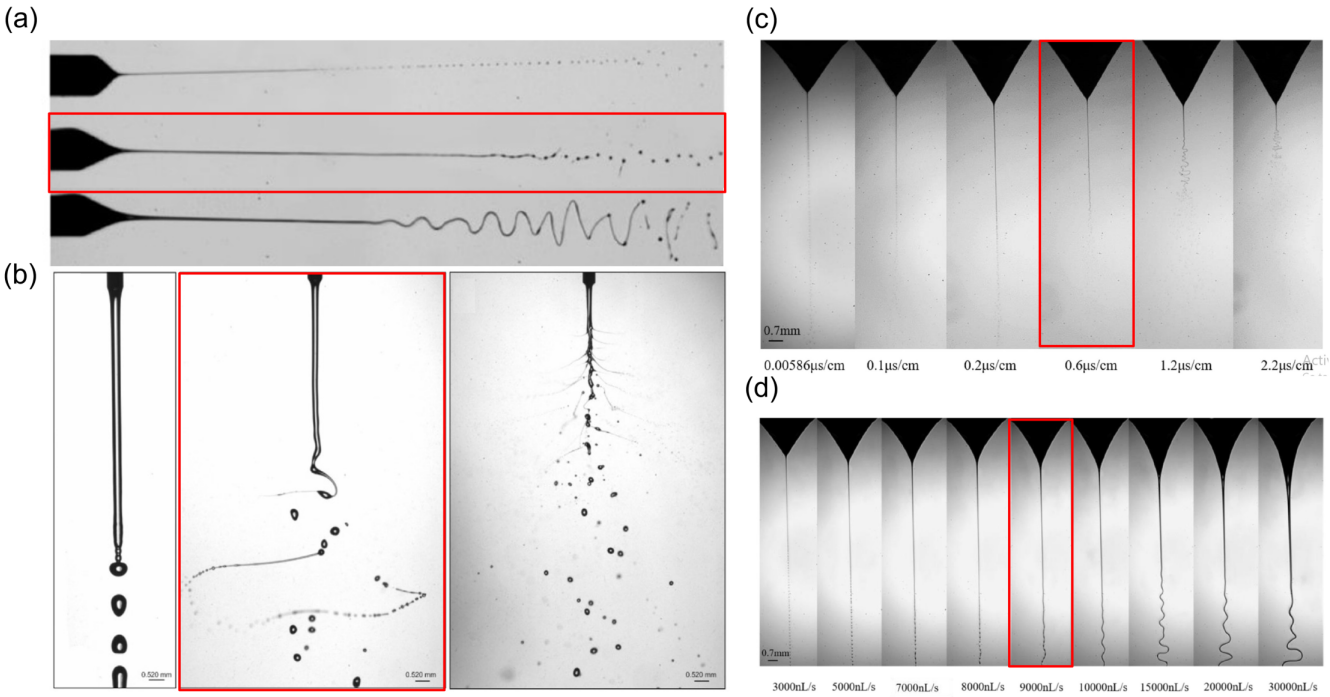

Figure 6.15: (a) Photographs of jet breakup, transition to whipping, and whipping regime. Figure credit from Yang *et al.*[20]. (b) Photographs of the three breakup mechanisms in the simple-jet mode deionized water: varicose breakup, whipping breakup, and ramified breakup. Figure credit from Agostinho *et al.*[21] (c) Photographs of jet breakup to whipping instabilities at the increasing conductivities of diethylene glycol (DEG) and (d) jet breakup to whipping instabilities at the increasing flow rates of DEG. Figure credit from Yang *et al.*[20].

Whipping emission is of significant interest since the electrospray plume angle can be affected by whipping behavior further downstream of the jet. In particular, whipping emission is intensified at the cone-to-jet region of high conductivity propellant, e.g., in unfavorable operating conditions at a high flow rate[10]. Whipping may be one of the possible failure mechanisms leading to electrospray overspray. Investigation of when and how whipping occurs is crucial to avoid unstable whipping emissions and for operation in favorable conditions.

The three main instabilities, classical Rayleigh, axisymmetric (conducting mode), and asymmetric (whipping) instabilities, were described by Hohman *et al.* and depicted by Bagchi *et al.* in

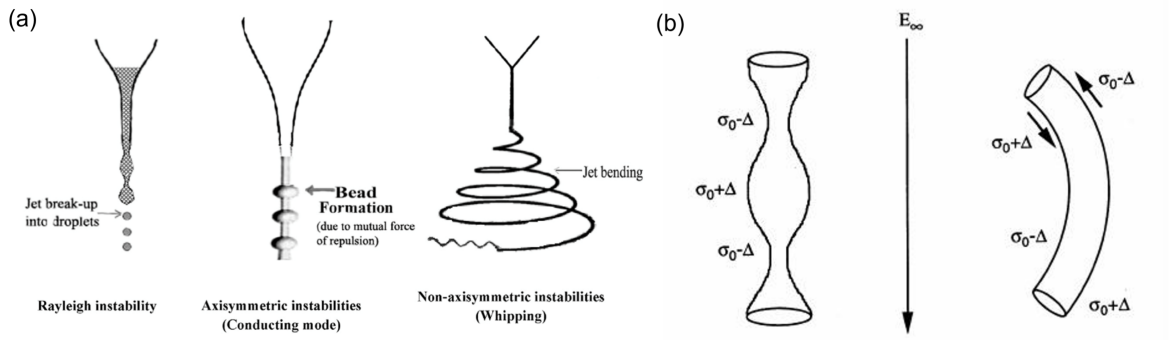

Figure 6.16: (a) Classical (axisymmetric) Rayleigh instability, Electric field induced axisymmetric instability, and asymmetric instability[22] and (b) perturbations of the surface charge density (σ_0) for axisymmetric and asymmetric instability in the jet. Figure credit from Hohman *et al.*[23]

Liquids	$\rho(kg/m^3)$	$\sigma(S/m)$	$\gamma(N/m)$	$\varepsilon(F/m)$	$\nu(m^2/s)$
DEG	1118	1×10^{-5}	0.0421	6.66	3.44×10^{-5}

Table 6.2: Liquid properties of Diethylene glycol (DEG).

Figure 6.16(a)[22, 23]. Rayleigh instability occurs mainly due to the surface tension force and is suppressed by high electrostatic and viscoelastic forces. Axisymmetric instability is induced by an externally applied electric field and occurs at the location where perturbation of the surface charge causes beads to emerge along with the straight jet. Coulombic repulsion and the electric field between bulging regions enhance the formation of the beads[23]. Note Δ in Figure 6.16(b) denotes the perturbation of the surface charge density. On the other hand, whipping instability initiates from jet bending caused by an imbalance of the tangential stresses due to the external electric field and surface charge movement[23]. The charge distribution interacts with the external electric field and leads to mutual repulsion of surface charges to cause jet bending. These instabilities grow at different rates according to the fluid properties and the given operating conditions[23].

To better understand the whipping mechanism, the main objective of this study was to capture the transition from jet breakup to the whipping regime, when the perturbation grows into meridional flow due to nonuniform charge density further downstream jet in Figure 6.15[20, 21]. Three separate regions are identified according to surface velocities, the cone-to-jet region of sink flow

with the surface velocity of 1-2 $\mathrm{m\,s^{-1}}$, the upstream jet with helical surface velocities of near zero magnitude, and the downstream jet with the clockwise toroidal flow and the magnitudes of the surface velocity increasing up to 5-8 $\mathrm{m\,s^{-1}}$ at $\delta = 0.68$, $Re_E = 0.67$, and $B_E = 49.3$.

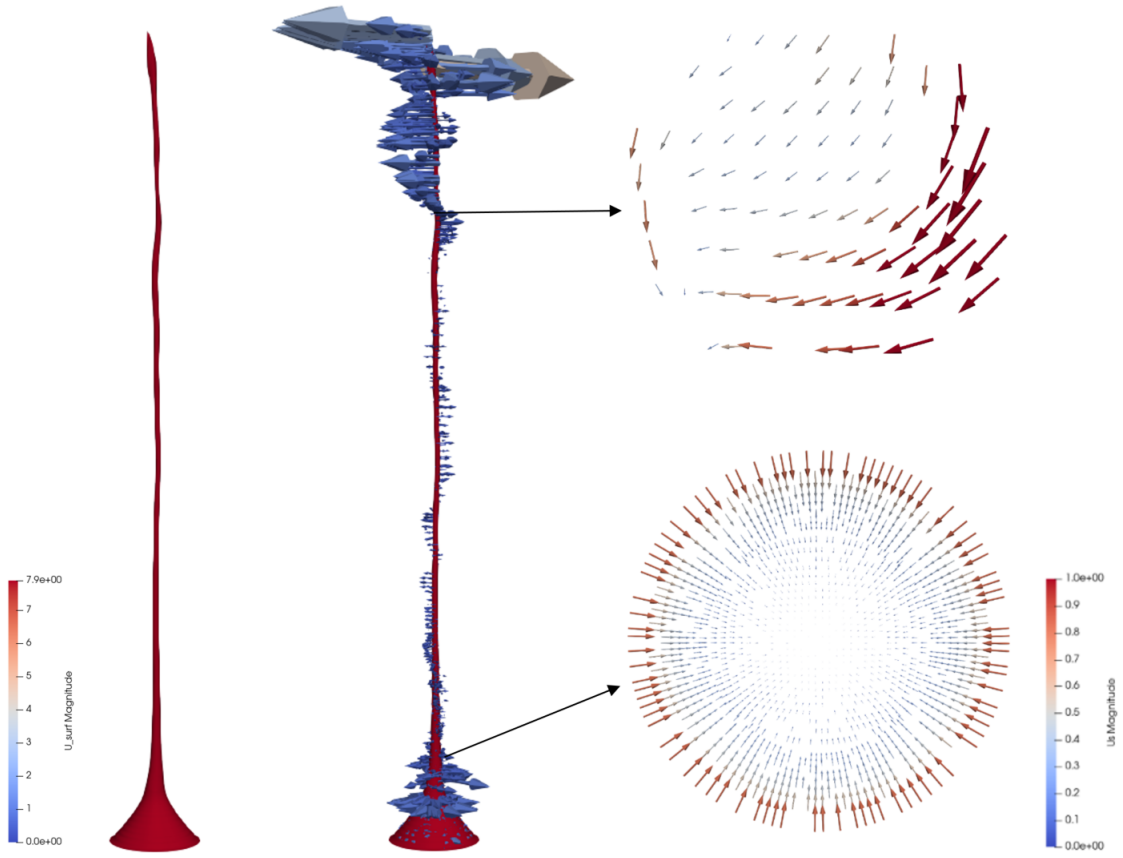

Figure 6.17: Computed results of a straight jet and the surface velocity field for diethylene glycol (DEG) at $B_E = 49.3$ in the given experimental setup[20]. Velocity fields on the horizontal cross-sectional are shown at the cone-to-jet and the downstream jet region.

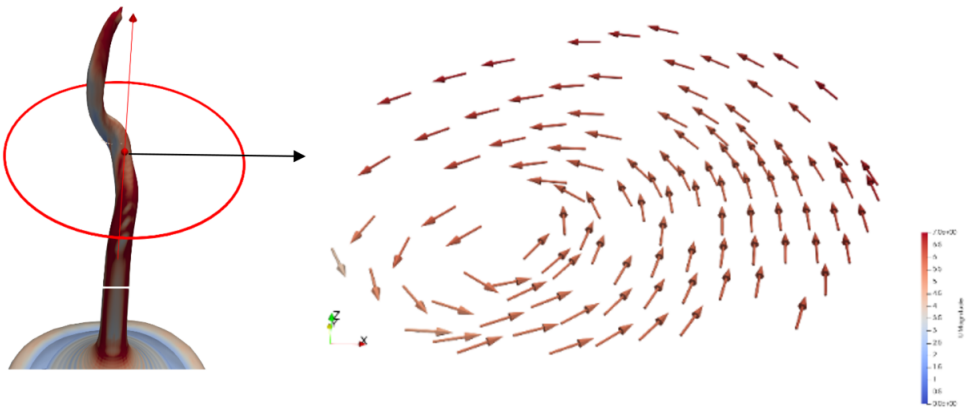

Figure 6.18: Asymmetric whipping emission and the magnified horizontal cross-sectional velocity field at startup condition, $t = 0.1\,\text{ms}$.

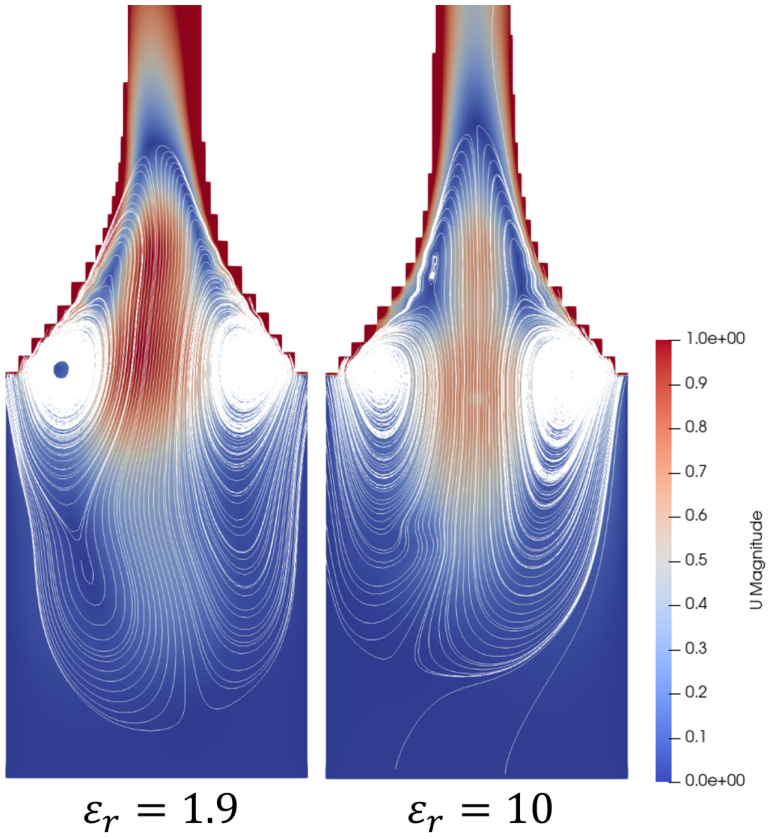

Figure 6.19: Velocity magnitude and flow field for DEG at $B_E = 126.9$, (a) $\varepsilon = 1.9$ and (b) $\varepsilon = 10$.

CHAPTER 7

Conclusion and Future Research

7.1 Conclusion

We have developed 2D and 3D leaky dielectric Electrohydrodynamic (EHD) models in the open-source Finite Volume Method (FVM) code OpenFOAM. Compared to the approaches such as Boundary Element Method (BEM), the FVM can accurately predict the interface and multidimensional mechanisms such as charge transport, internal flow, droplet breakup, and tilted cone-jet emission for electrospray devices. Our new interface interpolation scheme in the Volume-of-Fluid (VOF) method allows the conservation of electric charge and reproduces experimentally observed meniscus shapes in the cone-to-jet region. This interface scheme extends the FVM approach from low conductivity ($\sim 10^{-7}\,\mathrm{S\,m^{-1}}$, i.e., heptane) to moderate conductivities that are three orders of magnitude higher ($\sim 10^{-4}\,\mathrm{S\,m^{-1}}$). The new model is validated against droplet diameter, total current, and specific charge in good agreement with experiment and scaling laws for heptane and tributylphosphate (TBP) in the literature. Results show the droplet diameter decreases as the dimensionless flow rate decreases or the electric Reynolds number increases. These are consistent with the parametric investigation for the meniscus shape and the maximum charge density varying with the critical operating conditions, i.e., flow rate and potential difference, and key liquid properties, i.e., conductivity, surface tension, viscosity, and relative permittivity. Decreasing charge density with increasing relative permittivity is explained in terms of the effect of more considerable relaxation time being dominant over that of a steep meniscus due to a large polarization force. Results also show the meniscus changing from a concave to a convex shape toward the vacuum, increasing maximum charge density and decreasing cone-to-jet length as the conductivity or the

surface tension coefficient rises. A high charge density in the cone-to-jet region leads to a high specific charge of emitted droplets with a high jetting velocity. Further work will be required to extend the FVM approach with the new interpolation scheme to more challenging ionic liquids of high conductivity, such as EMI-Im, where the jet/diameter sizes are sub-microns requiring more computing powers due to the high resolution of the computational domain.

The energy equation is employed for the governing equation of the finite volume model to accurately predict the energy of the charged droplets under different operating conditions. The new interface interpolation scheme devised in the VOF method is implemented to ensure energy conservation for accurate temperature prediction due to Joule dissipation, i.e., Ohmic heating and viscous dissipation. The increasing temperature is observed after the cone-to-jet region, where internal and outer electric fields at the liquid surface are highest along the jet. Ohmic dissipation tends to reduce with increasing electrical permittivity, $T = 540\,\mathrm{K}$ at $\varepsilon = 20$ and $T = 420\,\mathrm{K}$ at $\varepsilon = 50$ for $B_E = 5.5$, where high charge relaxation impedes the electric field.

We extended the axisymmetric two-dimensional leaky dielectric EHD model using OpenFOAM to a three-dimensional EHD model to capture steady tilted cone-jet emission. The 3D model is validated against jet diameters from the experiment and scaling law for E2T8 liquid. Results show the jet diameter reduces with the increasing electrical Bond number. Cone-tilt occurs at $B_E = 67$ for dimensionless flow rate, $\delta = 9.2$, and at $B_E = 111$ for $\delta = 27.6$ where higher tangential electrostatic force results from a lower flow rate in the cone-to-jet region. The B_E above a critical value causes cone tilt, where asymmetric tangential electrostatic force results in a dilated surface on the tilted cone, allowing higher charge density until the surface tension counterbalances electrostatic force. The normal electric field at the dilated liquid meniscus is about 15 % higher than that on the opposite side of the meniscus, implying the valid jump condition for the electric field in the model. Although increasing permittivity leads to higher charge relaxation with a lower effective electric field that impedes charge transport through the cone and the jet, the ratio of the higher electrostatic force to the surface tension grants a lower critical electrical Bond number tilting the cone at $B_E = 72$ for $\varepsilon_r = 20$ and $B_E = 89$ for $\varepsilon_r = 9.2$.

Overall, this dissertation shows that important insight into electrospray physics can be obtained through 2D and 3D EHD FVM-based computational modeling. Thus, providing a platform for understanding electrospray physics and exploring pathways for improvement in the electrospray lifetime and performance. A critical development needed to perform this investigation of higher conductivity liquids relevant to electrospray thrusters was the development of a new interface interpolation scheme at the free surface that enables effective conservation of important quantities such as charge and energy.

7.2 Future Work

A large computational burden usually makes it challenging to utilize a CFD model for industrial applications[96, 97]. In particular, the EHD cases in this work require seven input parameters, including two operating conditions, i.e., voltage and flow rate, and five liquid properties, i.e., surface tension, viscosity, density, electrical conductivity, and permittivity. Geometric parameters such as the chamfering angle of the emitter and the emitter-extractor distance may also be considered independent input conditions. There are different approaches to developing a Reduced-Order-Model (ROM), which may alleviate excessive computing power requirements. One approach is to apply Proper Orthogonal Decomposition (POD), i.e., Principal Component Analysis (PCA), for randomly sampled conditions in the multidimensional parameter space[98]. It is followed by a regression step by the Gaussian process regression, Kriging, to perform regression for the coefficients of major eigenvectors as functions of operation conditions[99]. A ROM allows the development of the parametric space with two or more mutually independent input parameters, such as flow rate and electrical conductivity for electrospray emissions. The reconstructed EHD emission results are shown in Appendix F. ROM reproduces a 2-D axisymmetric scalar field at any unexplored operation conditions within a few seconds of calculation compared to several hours to days of actual CFD calculations. Mapping a multidimensional parameter space allows the creation of a digital twin domain for industrial use, reducing expensive computations.

Appendix A

Liquid properties

Liquids	$\rho(kg/m^3)$	$\sigma(S/m)$	$\gamma(N/m)$	$\varepsilon(F/m)$	$\nu(m^2/s)$
Heptane[5]	684	6.26×10^{-7}	0.0186	1.91	4.28×10^{-4}
TBP[7]	976	2.3×10^{-4}	0.028	8.91	3.59×10^{-3}
EMI-Im[7]	1520	8.8×10^{-1}	0.0349	10	2.24×10^{-5}
Ethanol[17]	789	1.5×10^{-4}	0.0228	29.1	1.86×10^{-6}
DEG[20]	1118	1×10^{-5}	0.0421	6.66	3.44×10^{-5}
E2T8[17]	909	1.5×10^{-6}	0.0315	9.2	1.49×10^{-5}
E4T6[17]	879	2.3×10^{-5}	0.0295	14	6.95×10^{-6}
E8T2[17]	819	1.1×10^{-4}	0.0263	22.8	2.54×10^{-6}

Table A.1: Liquid properties of heptane, tributyl phosphate (TBP), EMI-Im, ethanol, diethylene glycol (DEG), 20% ethanol and 80% terpineol liquid (E2T8), E4T6, and E8T2.

Appendix B

Transient Evolution

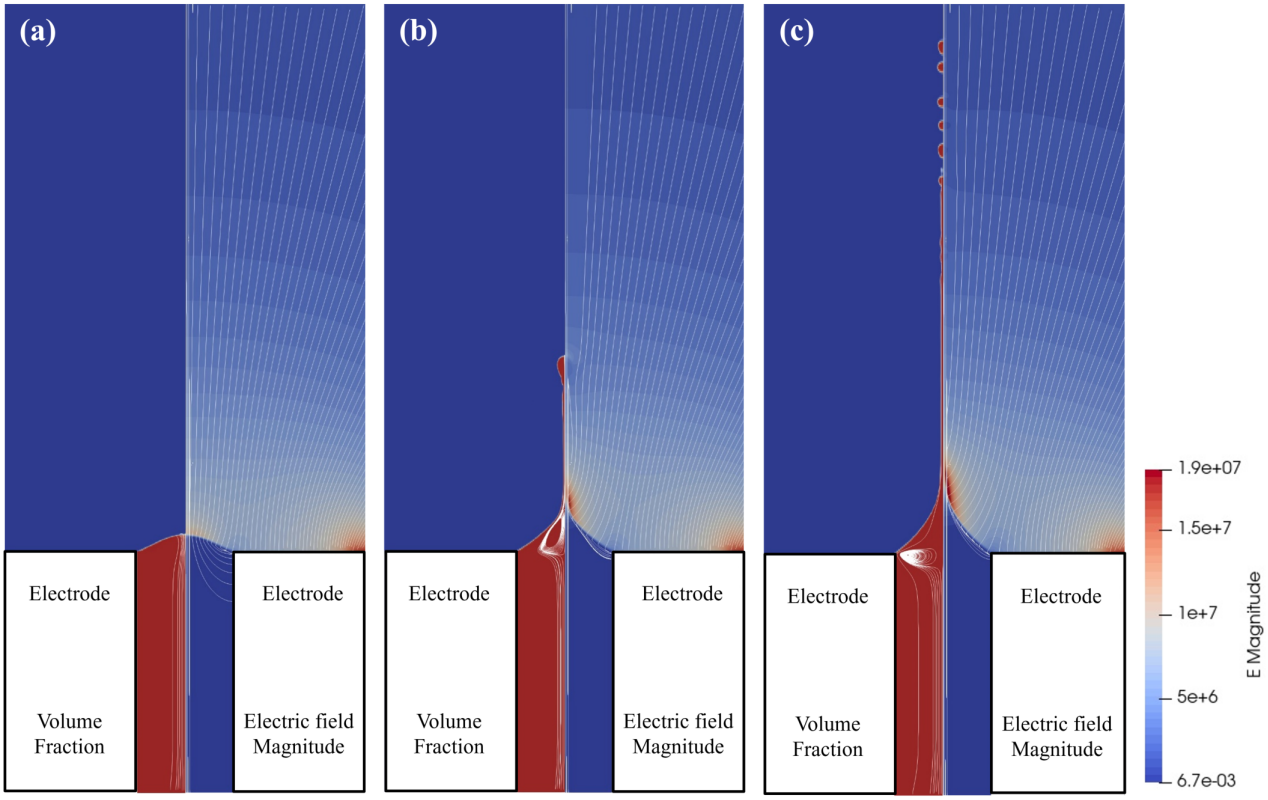

Figure B.1: Transient evolution of low conductivity, heptane, for volume fraction, electric field magnitude, and contour at (a) 0.19 ms, (b) 0.34 ms, and (c) 0.5 ms.

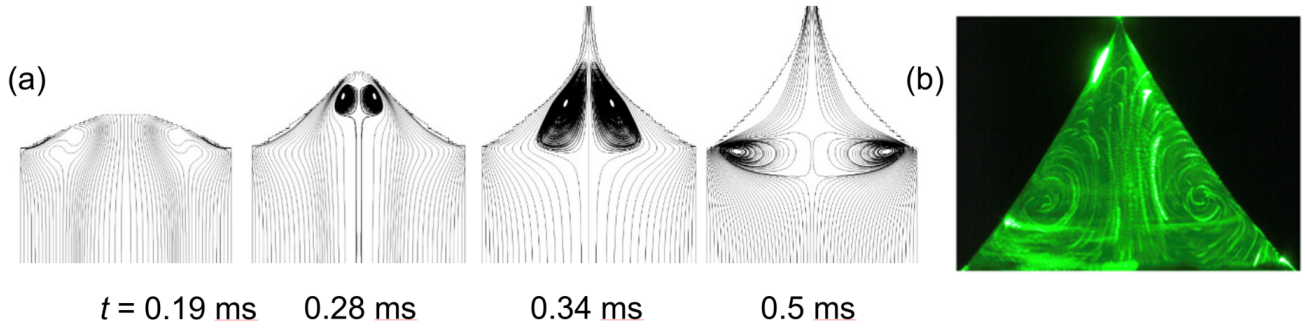

Figure B.2: (a) Transient evolution of the recirculation flow for heptane from the modeling and (b) the steady cone-jet mode from the experiment[24].

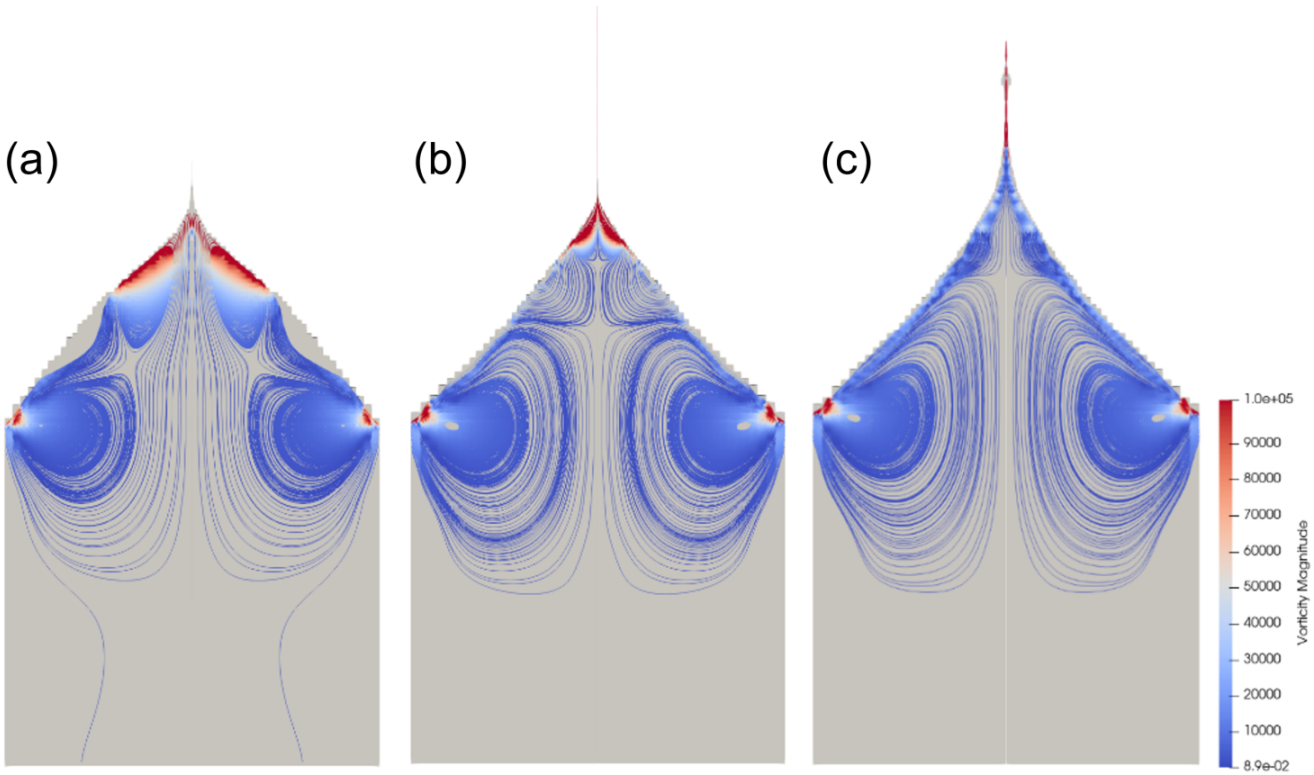

Figure B.3: (a) Transient evolution of the recirculation flow and vorticity magnitude for EMI-Im.

Appendix C

f parameter on Energy Equation

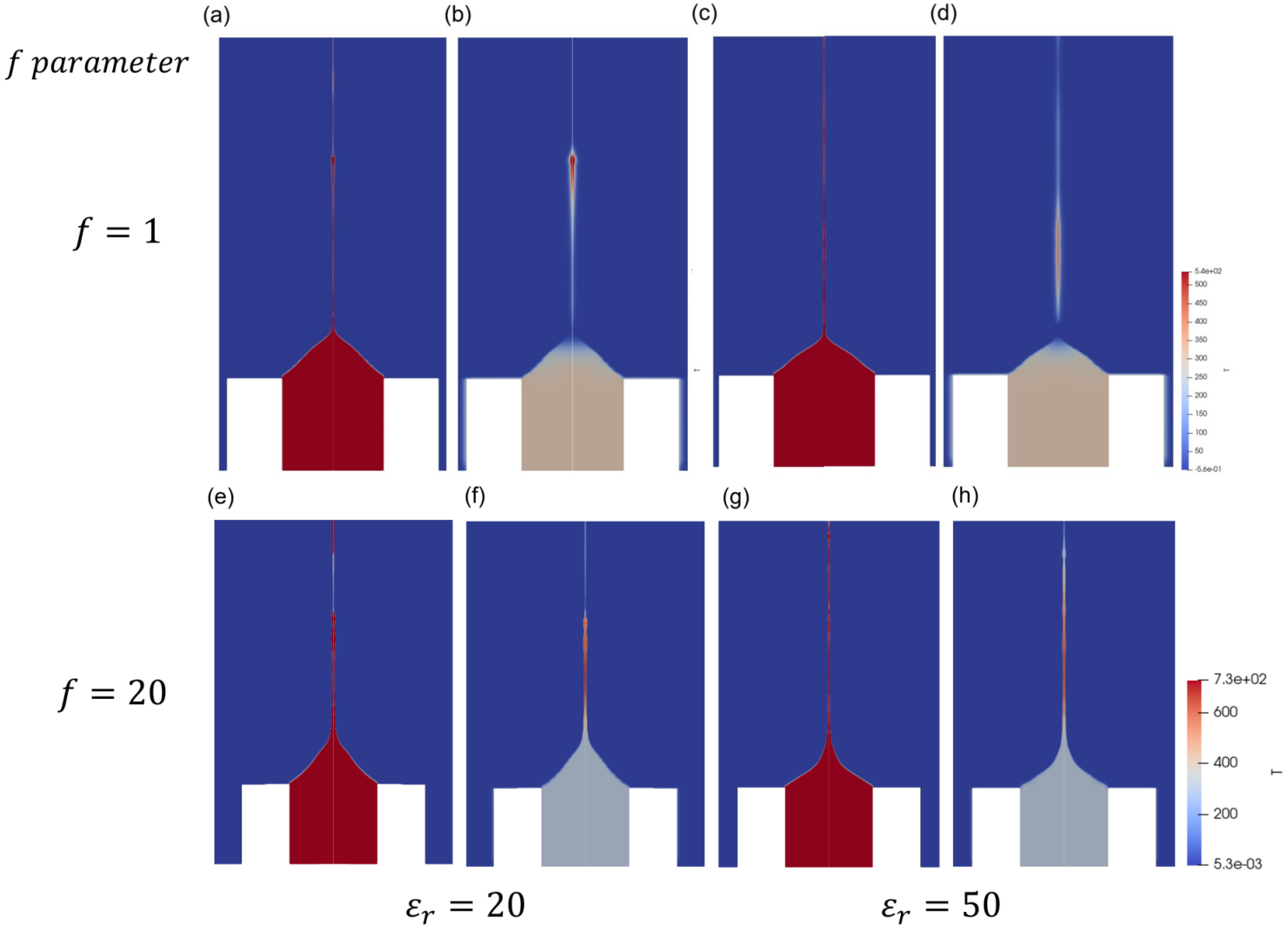

Figure C.1: Volume fraction and temperature field at (a,b) $f = 1$, $\varepsilon = 30$, (c,d) $f = 1$, $\varepsilon = 50$, (e,f) $f = 20$, $\varepsilon = 30$, and (g,h) $f = 20$, $\varepsilon = 50$.

Appendix D

Computational domain

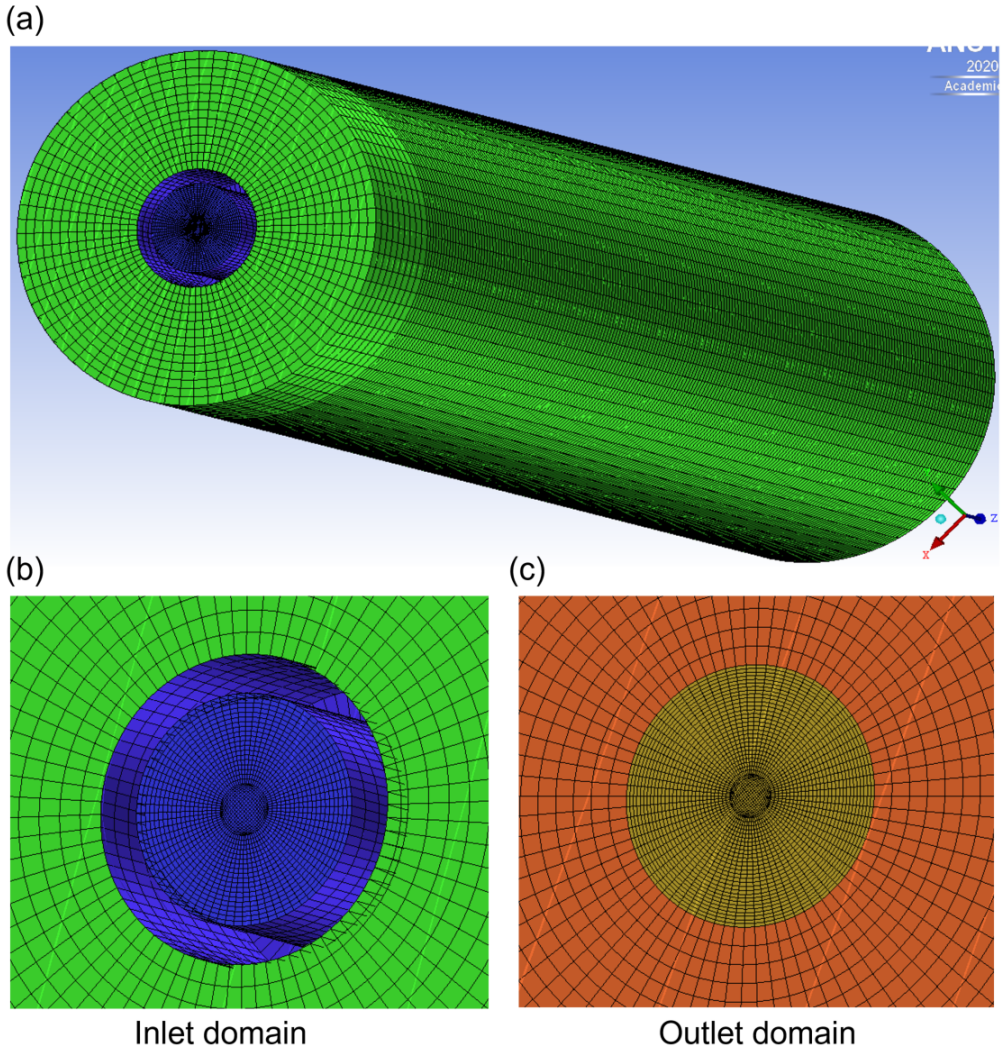

Figure D.1: (a) Three-dimensional computational domain with hexahedral structured 731,868 cells constructed by ANSYS-ICEM, (b) inlet, and (c) outlet domain using O-Grid technique.

Appendix E

Emission modes

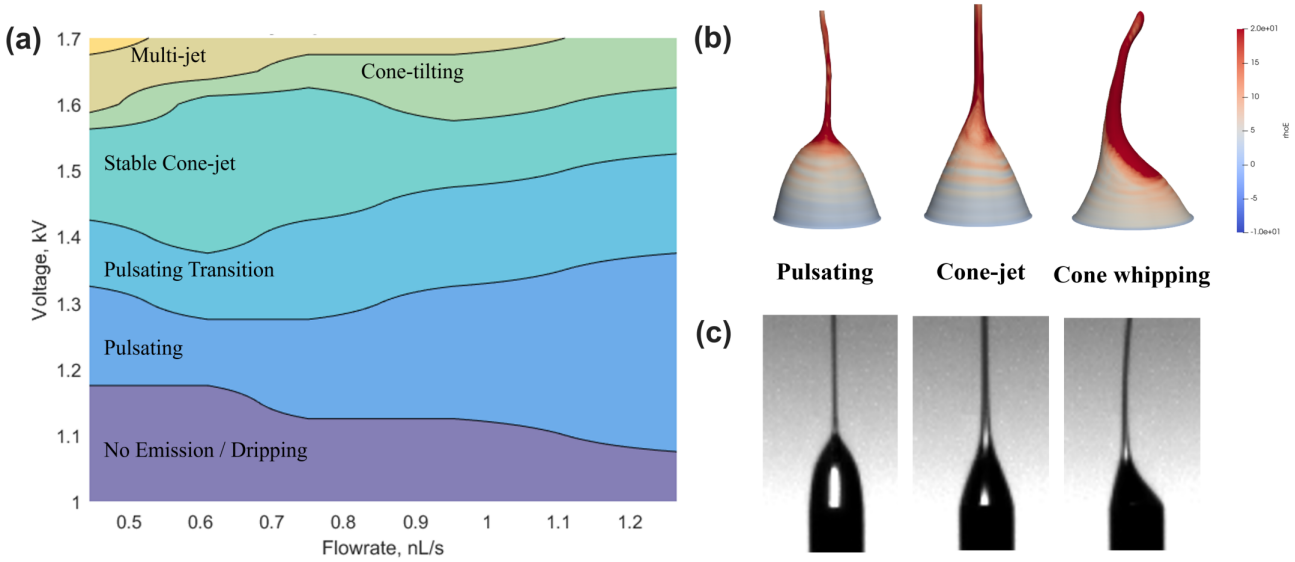

Figure E.1: (a) Regime map of EHD stability for ethanol[19], (b) computed pulsating, cone-jet, and cone whipping emission, and (c) associated experimental observations[19].

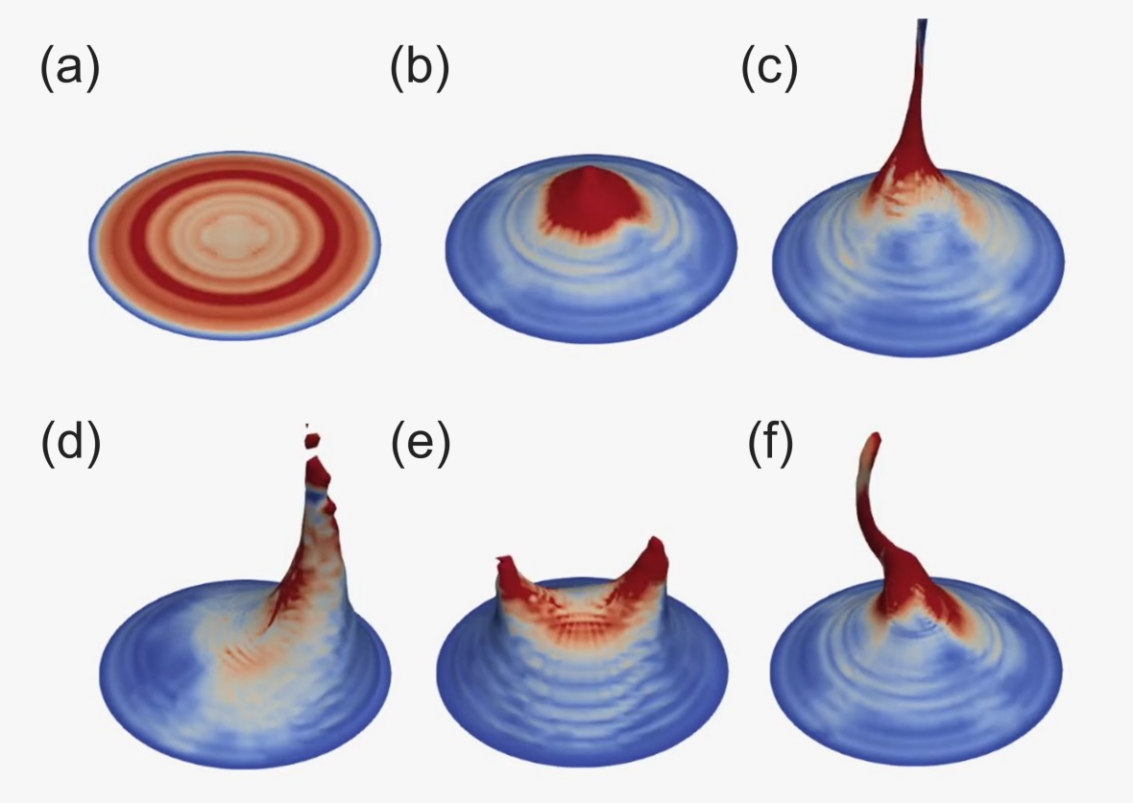

Figure E.2: (a-c) Transient evolution to achieve steady cone-jet emission, (d) asymmetric tilted cone-jet emission, (e) dual jet emission, and (f) whipping emission.

Appendix F

Reduced Order Model

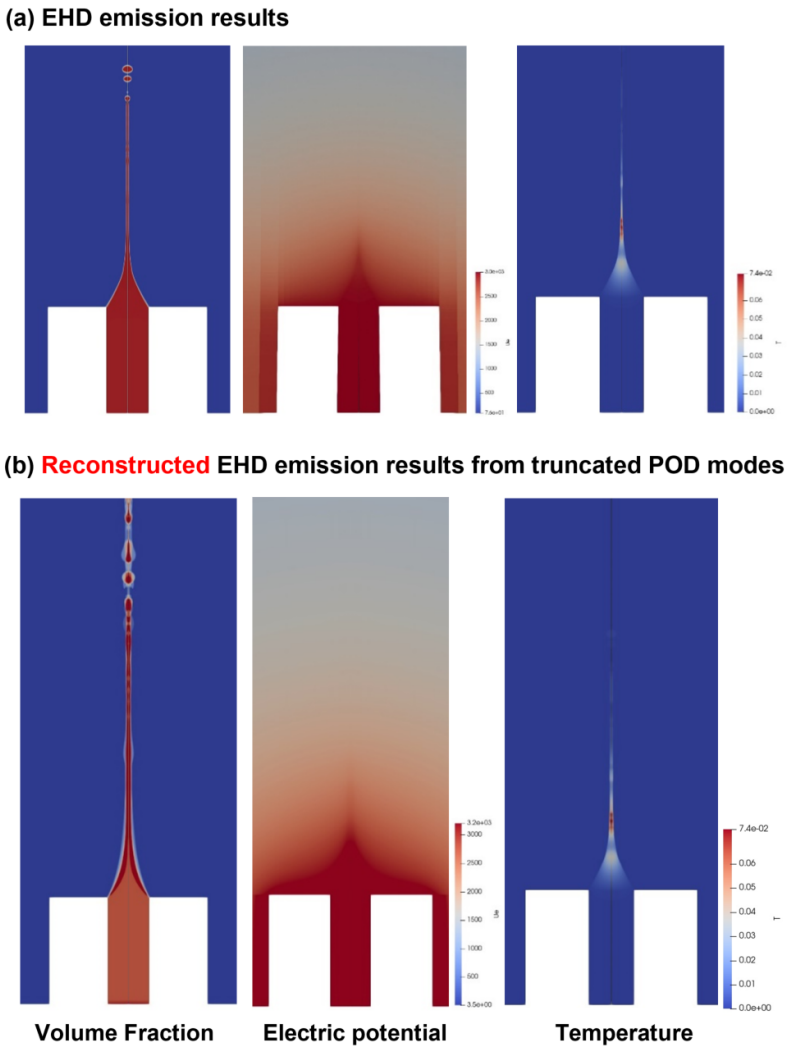

Figure F.1: Volume fraction, electric potential, and temperature field from (a) Electrospray emission results and (b) Reconstructed EHD emission results from truncated POD modes.

Bibliography

[1] E. Kulu, “Nanosatellite launch forecasts - track record and latest prediction,” 2022.

[2] R. Shimmin, J. Schalkwyck, A. Perez, S. Weston, A. Rademacher, J. Tilles, E. Agasid, R. Burton, A. Karacalioglu, and R. Carlino, “Small spacecraft state of the art report 2015,” 01 2016.

[3] M. Peukert and B. Wollenhaupt, “Ohb-system’s view on electric propulsion needs,” 11 2014.

[4] J. K. Ziemer, C. Marrese-Reading, S. M. Arestie, D. G. Conroy, S. D. Leifer, A. L. Ortega, N. R. Demmons, R. E. Wirz, and M. Gamero, *Incorporating Lessons Learned into LISA Colloid Microthruster Technology Development*. [Online]. Available: https://arc.aiaa.org/doi/abs/10.2514/6.2019-3814

[5] K. Tang and A. Gomez, “Monodisperse electrosprays of low electric conductivity liquids in the cone-jet mode,” *Journal of Colloid and Interface Science*, vol. 184, no. 2, pp. 500–511, 1996. [Online]. Available: https://www.sciencedirect.com/science/article/pii/S0021979796906451

[6] A. M. Gañán Calvo, “On the general scaling theory for electrospraying,” *Journal of Fluid Mechanics*, vol. 507, p. 203–212a, 2004.

[7] M. Gamero-Castaño and V. Hruby, “Electric measurements of charged sprays emitted by cone-jets,” *Journal of Fluid Mechanics*, vol. 459, p. 245–276, 2002.

[8] J. F. De La Mora and I. G. Loscertales, “The current emitted by highly conducting taylor cones,” *Journal of Fluid Mechanics*, vol. 260, p. 155–184, 1994.

[9] J. M. López-Herrera, A. M. Gañán-Calvo, and M. A. Herrada, “Absolute to convective instability transition in charged liquid jets,” *Physics of Fluids*, vol. 22, no. 6, p. 062002, 06 2010. [Online]. Available: https://doi.org/10.1063/1.3446972

[10] N. M. Uchizono, A. L. Collins, A. Thuppul, P. L. Wright, D. Q. Eckhardt, J. Ziemer, and R. E. Wirz, "Emission modes in electrospray thrusters operating with high conductivity ionic liquids," *Aerospace*, vol. 7, no. 10, 2020. [Online]. Available: https://www.mdpi.com/2226-4310/7/10/141

[11] P. Wright, H. Huh, N. M. Uchizono, A. Thuppul, and R. E. Wirz, *A Novel Variable Mode Emitter for Electrospray Thrusters*, Sep 2019. [Online]. Available: chrome-extension://efaidnbmnnnibpcajpcglclefindmkaj/https://electricrocket.org/2019/650.pdf

[12] J. K. Ziemer, "Performance of electrospray thrusters iepc-2009-242," 2009. [Online]. Available: https://api.semanticscholar.org/CorpusID:111379910

[13] M. Magnani and M. Gamero, *Modeling of the Dissipation and Self-Heating of the Propellant in Electrospray Thrusters*. [Online]. Available: https://arc.aiaa.org/doi/abs/10.2514/6.2019-4171

[14] A. Thuppul, A. L. Collins, P. L. Wright, N. M. Uchizono, and R. E. Wirz, "Mass flux and current density distributions of electrospray plumes," *Journal of Applied Physics*, vol. 130, no. 10, p. 103301, 2021. [Online]. Available: https://doi.org/10.1063/5.0056761

[15] J. K. Ziemer, T. Randolph, V. Hruby, D. Spence, N. Demmons, T. Roy, W. Connolly, E. Ehrbar, J. Zwahlen, and R. Martin, "Colloid Microthrust Propulsion for the Space Technology 7 (ST7) and LISA Missions," *AIP Conference Proceedings*, vol. 873, no. 1, pp. 548–555, 11 2006. [Online]. Available: https://doi.org/10.1063/1.2405097

[16] J. K. Ziemer, T. M. Randolph, M. Gamero-Castaño, V. J. Hruby, W. Connolly, N. R. Demmons, E. Ehrbar, R. Martin, T. Roy, and D. Spence, "Flight hardware development of colloid microthruster technology for the space technology 7 and lisa missions iepc-2007-288," 2007.

[17] A. Lee, H. Jin, H.-W. Dang, K.-H. Choi, and K. H. Ahn, "Optimization of experimental parameters to determine the jetting regimes in electrohydrodynamic printing," *Langmuir*,

vol. 29, no. 44, pp. 13 630–13 639, 2013, pMID: 24102618. [Online]. Available: https://doi.org/10.1021/la403111m

[18] M. R. Morad, A. Rajabi, M. Razavi, and S. R. P. Sereshkeh, "A very stable high throughput taylor cone-jet in electrohydrodynamics," *Sci Rep*, vol. 6, p. 38509, Dec. 2016.

[19] P. Wright, A. Thuppul, and R. E. Wirz, *Life-Limiting Emission Modes for Electrospray Thrusters*. [Online]. Available: https://arc.aiaa.org/doi/abs/10.2514/6.2018-4726

[20] S. Yang, Z. Wang, Q. Kong, and B. Li, "Varicose-whipping instabilities transition of an electrified micro-jet in electrohydrodynamic cone-jet regime," *International Journal of Multiphase Flow*, vol. 146, p. 103851, 2022. [Online]. Available: https://www.sciencedirect.com/science/article/pii/S0301932221002731

[21] L. Agostinho, B. Bos, A. Kamau, S. Brouwer, E. Fuchs, and J. Marijnissen, "Simple-jet mode electrosprays with water. description, characterization and application in a single effect evaporation chamber," *Journal of Aerosol Science*, vol. 125, pp. 237–250, 2018, from Electro-Hydro-Dynamics of liquids for the production of charged droplets by Electro-Spray to applications for tailored Materials (aerosols, powders, coatings) and Environment. [Online]. Available: https://www.sciencedirect.com/science/article/pii/S0021850217304299

[22] S. Bagchi, R. Brar, B. Singh, and C. Ghanshyam, "Instability controlled synthesis of tin oxide nanofibers and their gas sensing properties," *Journal of Electrostatics*, vol. 78, pp. 68–78, 2015. [Online]. Available: https://www.sciencedirect.com/science/article/pii/S0304388615300528

[23] M. M. Hohman, M. Shin, G. Rutledge, and M. P. Brenner, "Electrospinning and electrically forced jets. I. Stability theory," *Physics of Fluids*, vol. 13, no. 8, pp. 2201–2220, 08 2001. [Online]. Available: https://doi.org/10.1063/1.1383791

[24] A. Gupta, B. K. Mishra, and P. Panigrahi, "Experimental investigation of flow field inside a taylor cone," 2019.

[25] L. Habl and P. Gessini, “Design of a cubesat propulsion system using a cylindrical,” 2015.

[26] BryceTech, “Smallsats by the numbers 2022,” 2022. [Online]. Available: https://brycetech.com/reports/report-documents/Bryce_Smallsats_2022.pdf

[27] D. J. Barnhart, “Very small satellite design for space sensor networks.” Ph.D. dissertation, University of Surrey (United Kingdom)., Guildford, 2008.

[28] R. G. Jahn, *Physics of electric propulsion*. McGraw-Hill, 1968.

[29] I. Levchenko, D. M. Goebel, and K. Bazaka, “Electric propulsion of spacecraft,” *Physics Today*, vol. 75, no. 9, pp. 38–44, 09 2022. [Online]. Available: https://doi.org/10.1063/PT.3.5081

[30] I. Romero-Sanz, R. Bocanegra, J. Fernandez de la Mora, and M. Gamero-Castaño, “Source of heavy molecular ions based on Taylor cones of ionic liquids operating in the pure ion evaporation regime,” *Journal of Applied Physics*, vol. 94, no. 5, pp. 3599–3605, 08 2003. [Online]. Available: https://doi.org/10.1063/1.1598281

[31] M. R. Natisin and H. L. Zamora, “Performance of a fully conventionally machined liquid-ion electrospray thruster operated in pir,” 2019.

[32] G. I. Taylor, “Disintegration of water drops in an electric field,” *Proceedings of the Royal Society of London. Series A. Mathematical and Physical Sciences*, vol. 280, no. 1382, pp. 383–397, 1964. [Online]. Available: https://royalsocietypublishing.org/doi/abs/10.1098/rspa.1964.0151

[33] J. Zeleny, “The electrical discharge from liquid points, and a hydrostatic method of measuring the electric intensity at their surfaces,” *Phys. Rev.*, vol. 3, pp. 69–91, Feb 1914. [Online]. Available: https://link.aps.org/doi/10.1103/PhysRev.3.69

[34] M. Cloupeau and B. Prunet-Foch, “Electrohydrodynamic spraying functioning modes: a critical review,” *Journal of Aerosol Science*, vol. 25, no. 6, pp. 1021–1036, Sep. 1994.

[35] J. R. Melcher and G. I. Taylor, "Electrohydrodynamics: A review of the role of interfacial shear stresses," *Annual Review of Fluid Mechanics*, vol. 1, no. 1, pp. 111–146, 1969. [Online]. Available: https://doi.org/10.1146/annurev.fl.01.010169.000551

[36] A. Gañán-Calvo, J. Dávila, and A. Barrero, "Current and droplet size in the electrospraying of liquids. scaling laws," *Journal of Aerosol Science*, vol. 28, no. 2, pp. 249–275, 1997. [Online]. Available: https://www.sciencedirect.com/science/article/pii/S0021850296004338

[37] C. Pantano, A. Gañán-Calvo, and A. Barrero, "Zeroth-order, electrohydrostatic solution for electrospraying in cone-jet mode," *Journal of Aerosol Science*, vol. 25, no. 6, pp. 1065–1077, 1994. [Online]. Available: https://www.sciencedirect.com/science/article/pii/002185029490202X

[38] F. J. Higuera, "Flow rate and electric current emitted by a taylor cone," *Journal of Fluid Mechanics*, vol. 484, p. 303–327, 2003.

[39] M. Gamero-Castaño and M. Magnani, "Numerical simulation of electrospraying in the cone-jet mode," *Journal of Fluid Mechanics*, vol. 859, p. 247–267, 2019.

[40] M. Herrada and J. Montanero, "A numerical method to study the dynamics of capillary fluid systems," *Journal of Computational Physics*, vol. 306, pp. 137–147, 2016. [Online]. Available: https://www.sciencedirect.com/science/article/pii/S0021999115007883

[41] A. Ponce-Torres, N. Rebollo-Muñoz, M. A. Herrada, A. M. Gañán-Calvo, and J. M. Montanero, "The steady cone-jet mode of electrospraying close to the minimum volume stability limit," *Journal of Fluid Mechanics*, vol. 857, p. 142–172, 2018.

[42] I. Roghair, M. Musterd, D. van den Ende, C. Kleijn, M. Kreutzer, and F. Mugele, "A numerical technique to simulate display pixels based on electrowetting," *Microfluidics and Nanofluidics*, vol. 19, no. 2, pp. 465–482, 2015. [Online]. Available: https://doi.org/10.1007/s10404-015-1581-5

[43] H. Dastourani, M. Jahannama, and A. Eslami-Majd, "A physical insight into electrospray process in cone-jet mode: Role of operating parameters," *International Journal of Heat and Fluid Flow*, vol. 70, pp. 315–335, 2018. [Online]. Available: https://www.sciencedirect.com/science/article/pii/S0142727X17310354

[44] J. López-Herrera, S. Popinet, and M. Herrada, "A charge-conservative approach for simulating electrohydrodynamic two-phase flows using volume-of-fluid," *J. Comput. Phys.*, vol. 230, pp. 1939–1955, 2011.

[45] M. A. Herrada, J. M. López-Herrera, A. M. Gañán Calvo, E. J. Vega, J. M. Montanero, and S. Popinet, "Numerical simulation of electrospray in the cone-jet mode," *Phys. Rev. E*, vol. 86, p. 026305, Aug 2012. [Online]. Available: https://link.aps.org/doi/10.1103/PhysRevE.86.026305

[46] S. Popinet, "Gerris: a tree-based adaptive solver for the incompressible euler equations in complex geometries," *Journal of Computational Physics*, vol. 190, no. 2, pp. 572–600, 2003. [Online]. Available: https://www.sciencedirect.com/science/article/pii/S0021999103002985

[47] P. L. Wright and R. E. Wirz, "Multiplexed electrospray emission on a porous wedge," *Physics of Fluids*, vol. 33, no. 1, p. 012003, 2021. [Online]. Available: https://doi.org/10.1063/5.0030031

[48] M. Sheikholeslami, "Numerical approach for mhd al2o3-water nanofluid transportation inside a permeable medium using innovative computer method," *Computer Methods in Applied Mechanics and Engineering*, vol. 344, pp. 306–318, 2019. [Online]. Available: https://www.sciencedirect.com/science/article/pii/S004578251830495X

[49] A. Dogonchi, Z. Asghar, and M. Waqas, "Cvfem simulation for fe3o4-h2o nanofluid in an annulus between two triangular enclosures subjected to magnetic field and thermal radiation," *International Communications in Heat and Mass Transfer*, vol. 112,

p. 104449, 2020. [Online]. Available: https://www.sciencedirect.com/science/article/pii/S073519331930315X

[50] J. K. Ziemer, C. Marrese-Reading, S. Arestie, N. R. Demmons, R. E. Wirz, A. Collins, and M. Gamero, *Progress on Developing LISA Microthruster Technology*. [Online]. Available: https://arc.aiaa.org/doi/abs/10.2514/6.2020-3609

[51] D. A. Saville, "Electrohydrodynamics: The taylor-melcher leaky dielectric model," *Annual Review of Fluid Mechanics*, vol. 29, no. 1, pp. 27–64, 1997. [Online]. Available: https://doi.org/10.1146/annurev.fluid.29.1.27

[52] O. Lastow and W. Balachandran, "Numerical simulation of electrohydrodynamic (ehd) atomization," *Journal of Electrostatics*, vol. 64, no. 12, pp. 850–859, 2006. [Online]. Available: https://www.sciencedirect.com/science/article/pii/S0304388606000283

[53] J. R. Melcher, *Continuum electromechanics*. MIT Press, 1981.

[54] D. Kothe, W. Rider, S. Mosso, J. Brock, and J. Hochstein, *Volume tracking of interfaces having surface tension in two and three dimensions*, 2012. [Online]. Available: https://arc.aiaa.org/doi/abs/10.2514/6.1996-859

[55] C. Hirt and B. Nichols, "Volume of fluid (vof) method for the dynamics of free boundaries," *Journal of Computational Physics*, vol. 39, no. 1, pp. 201–225, 1981. [Online]. Available: https://www.sciencedirect.com/science/article/pii/0021999181901455

[56] H. Huh and R. E. Wirz, "Numerical simulation of electrospray thruster extraction for highly conductive propellants," 2019.

[57] M. J. Breddan and R. E. Wirz, "Electrospray plume evolution: Influence of drag," *Journal of Aerosol Science*, vol. 167, p. 106079, 2023. [Online]. Available: https://www.sciencedirect.com/science/article/pii/S002185022200115X

[58] S. M. Parmar, A. L. Collins, and R. E. Wirz, *Electrospray Plume Modeling for Rapid Life and Performance Analysis*. [Online]. Available: https://arc.aiaa.org/doi/abs/10.2514/6.2022-1357

[59] N. M. Uchizono, A. L. Collins, C. Marrese-Reading, S. M. Arestie, J. K. Ziemer, and R. E. Wirz, "The role of secondary species emission in vacuum facility effects for electrospray thrusters," *Journal of Applied Physics*, vol. 130, no. 14, p. 143301, 10 2021. [Online]. Available: https://doi.org/10.1063/5.0063476

[60] J. Brackbill, D. Kothe, and C. Zemach, "A continuum method for modeling surface tension," *Journal of Computational Physics*, vol. 100, no. 2, pp. 335–354, 1992. [Online]. Available: https://www.sciencedirect.com/science/article/pii/002199919290240Y

[61] H. Rusche, "Computational fluid dynamics of dispersed two-phase flows at high phase fractions," 2003.

[62] M. Aboukhedr, A. Georgoulas, M. Marengo, M. Gavaises, and K. Vogiatzaki, "Simulation of micro-flow dynamics at low capillary numbers using adaptive interface compression," *Computers and Fluids*, vol. 165, pp. 13–32, 2018. [Online]. Available: https://www.sciencedirect.com/science/article/pii/S0045793018300094

[63] D. A. Hoang, V. van Steijn, L. M. Portela, M. T. Kreutzer, and C. R. Kleijn, "Benchmark numerical simulations of segmented two-phase flows in microchannels using the volume of fluid method," *Computers and Fluids*, vol. 86, pp. 28–36, 2013. [Online]. Available: https://www.sciencedirect.com/science/article/pii/S0045793013002612

[64] H. Jasak and T. Uroić, *Practical Computational Fluid Dynamics with the Finite Volume Method*. Cham: Springer International Publishing, 2020, pp. 103–161. [Online]. Available: https://doi.org/10.1007/978-3-030-37518-8_4

[65] Y. Okagaki, T. Yonomoto, M. Ishigaki, and Y. Hirose, "Numerical study on an interface compression method for the volume of fluid approach," *Fluids*, vol. 6, no. 2, 2021. [Online]. Available: https://www.mdpi.com/2311-5521/6/2/80

[66] N. D. Vaughan, D. N. Johnston, and K. A. Edge, "Numerical simulation of fluid flow in poppet valves," *Proceedings of the Institution of Mechanical Engineers, Part C: Journal of Mechanical Engineering Science*, vol. 206, no. 2, pp. 119–127, 1992.

[67] J. Roenby, H. Bredmose, and H. Jasak, "A computational method for sharp interface advection," *Royal Society Open Science*, vol. 3, no. 11, p. 160405, 2016. [Online]. Available: https://royalsocietypublishing.org/doi/abs/10.1098/rsos.160405

[68] G. Tomar, D. Gerlach, G. Biswas, N. Alleborn, A. Sharma, F. Durst, S. Welch, and A. Delgado, "Two-phase electrohydrodynamic simulations using a volume-of-fluid approach," *Journal of Computational Physics*, vol. 227, no. 2, pp. 1267–1285, 2007. [Online]. Available: https://www.sciencedirect.com/science/article/pii/S0021999107003932

[69] M. Gamero-Castaño, "Electric-field-induced ion evaporation from dielectric liquid," *Phys. Rev. Lett.*, vol. 89, p. 147602, Sep 2002. [Online]. Available: https://link.aps.org/doi/10.1103/PhysRevLett.89.147602

[70] M. Gamero-Castaño, "Electric-field-induced ion evaporation from dielectric liquid." *Physical review letters*, vol. 89 14, p. 147602, 2002.

[71] J. Vila, P. Ginés, J. Pico, C. Franjo, E. Jiménez, L. Varela, and O. Cabeza, "Temperature dependence of the electrical conductivity in emim-based ionic liquids: Evidence of vogel–tamman–fulcher behavior," *Fluid Phase Equilibria*, vol. 242, no. 2, pp. 141–146, 2006. [Online]. Available: https://www.sciencedirect.com/science/article/pii/S0378381206000793

[72] M. Gamero-Castaño, "Dissipation in cone-jet electrosprays and departure from isothermal operation." *Physical review. E*, vol. 99 6-1, p. 061101, 2019.

[73] C. Ma and C. Ryan, "Plume particle energy analysis of an ionic liquid electrospray ion source with high emission density," *Journal of Applied Physics*, vol. 129, no. 8, p. 083302, 2021. [Online]. Available: https://doi.org/10.1063/5.0035889

[74] A. M. Gañán Calvo, "The surface charge in electrospraying: Its nature and its universal scaling laws," *Journal of Aerosol Science*, vol. 30, no. 7, pp. 863–872, 1999. [Online]. Available: https://www.sciencedirect.com/science/article/pii/S0021850298007800

[75] S. W. Miller, B. D. Prince, R. J. Bemish, and J. L. Rovey, "Electrospray of 1-butyl-3-methylimidazolium dicyanamide under variable flow rate operations," *Journal of Propulsion and Power*, vol. 30, no. 6, pp. 1701–1710, 2014. [Online]. Available: https://doi.org/10.2514/1.B35170

[76] M. Gamero-Castaño and J. Fernández de la Mora, "Direct measurement of ion evaporation kinetics from electrified liquid surfaces," *The Journal of Chemical Physics*, vol. 113, no. 2, pp. 815–832, 2000. [Online]. Available: https://doi.org/10.1063/1.481857

[77] D. Garoz, C. Bueno, C. Larriba, S. Castro, I. Romero-Sanz, J. Fernandez de la Mora, Y. Yoshida, and G. Saito, "Taylor cones of ionic liquids from capillary tubes as sources of pure ions: The role of surface tension and electrical conductivity," *Journal of Applied Physics*, vol. 102, no. 6, p. 064913, 2007. [Online]. Available: https://doi.org/10.1063/1.2783769

[78] I. Romero-Sanz, R. Bocanegra, J. Fernandez de la Mora, and M. Gamero-Castaño, "Source of heavy molecular ions based on taylor cones of ionic liquids operating in the pure ion evaporation regime," *Journal of Applied Physics*, vol. 94, no. 5, pp. 3599–3605, 2003. [Online]. Available: https://doi.org/10.1063/1.1598281

[79] J. Zeleny, "Instability of electrified liquid surfaces," *Phys. Rev.*, vol. 10, pp. 1–6, Jul 1917. [Online]. Available: https://link.aps.org/doi/10.1103/PhysRev.10.1

[80] I. Hayati, A. I. Bailey, and T. F. Tadros, "Mechanism of stable jet formation in electrohydrodynamic atomization," *Nature*, vol. 319, no. 6048, pp. 41–43, 1986. [Online]. Available: https://doi.org/10.1038/319041a0

[81] A. Gupta, B. K. Mishra, and P. Panigrahi, "Internal and external hydrodynamics of taylor cone under constant and alternating voltage actuation," *Physics of Fluids*, vol. 33, no. 11, p. 117118, 2021. [Online]. Available: https://doi.org/10.1063/5.0071921

[82] V. Shtern, *Bifurcation of Swirl in Conical Counterflows*. Cambridge University Press, 2012, p. 28–59.

[83] V. Shtern and A. Barrero, "Striking features of fluid flows in taylor cones related to electrosprays," *Journal of Aerosol Science*, vol. 25, no. 6, pp. 1049–1063, 1994. [Online]. Available: https://www.sciencedirect.com/science/article/pii/0021850294902011

[84] A. Barrero, A. M. Gañán Calvo, J. Dávila, A. Palacio, and E. Gómez-González, "Low and high reynolds number flows inside taylor cones," *Phys. Rev. E*, vol. 58, pp. 7309–7314, Dec 1998. [Online]. Available: https://link.aps.org/doi/10.1103/PhysRevE.58.7309

[85] D. P. H. Smith, "The electrohydrodynamic atomization of liquids," *IEEE Transactions on Industry Applications*, vol. IA-22, no. 3, pp. 527–535, 1986.

[86] G. Biswas, M. Breuer, and F. Durst, "Backward-Facing Step Flows for Various Expansion Ratios at Low and Moderate Reynolds Numbers ," *Journal of Fluids Engineering*, vol. 126, no. 3, pp. 362–374, 07 2004. [Online]. Available: https://doi.org/10.1115/1.1760532

[87] A. Xu, Y. Zhang, Z. Li, and J. Wang, "Viscosities and conductivities of 1-butyl-3-methylimidazolium carboxylates ionic liquids at different temperatures," *Journal of Chemical & Engineering Data*, vol. 57, no. 11, pp. 3102–3108, 2012. [Online]. Available: https://doi.org/10.1021/je300507h

[88] J. Jacquemin, P. Husson, A. A. H. Padua, and V. Majer, "Density and viscosity of several pure and water-saturated ionic liquids," *Green Chem.*, vol. 8, pp. 172–180, 2006. [Online]. Available: http://dx.doi.org/10.1039/B513231B

[89] Y. Fujiwara, "Effects of the temperature of a protic ionic liquid on ion beam production by vacuum electrospray," *Journal of Vacuum Science Technology B*, vol. 41, no. 2, p. 024202, 03 2023. [Online]. Available: https://doi.org/10.1116/6.0002403

[90] M. Gamero-Castaño, "Dissipation in cone-jet electrosprays and departure from isothermal operation," *Phys. Rev. E*, vol. 99, p. 061101, Jun 2019. [Online]. Available: https://link.aps.org/doi/10.1103/PhysRevE.99.061101

[91] H. Huh and R. E. Wirz, "Simulation of electrospray emission processes for low to moderate conductivity liquids," *Physics of Fluids*, vol. 34, no. 11, 11 2022, 112017. [Online]. Available: https://doi.org/10.1063/5.0120737

[92] J. Rosell-Llompart, J. Grifoll, and I. G. Loscertales, "Electrosprays in the cone-jet mode: From taylor cone formation to spray development," *Journal of Aerosol Science*, vol. 125, pp. 2–31, 2018, from Electro-Hydro-Dynamics of liquids for the production of charged droplets by Electro-Spray to applications for tailored Materials (aerosols, powders, coatings) and Environment. [Online]. Available: https://www.sciencedirect.com/science/article/pii/S0021850217304366

[93] A. Thuppul, P. L. Wright, A. L. Collins, J. K. Ziemer, and R. E. Wirz, "Lifetime considerations for electrospray thrusters," *Aerospace*, vol. 7, no. 8, 2020. [Online]. Available: https://www.mdpi.com/2226-4310/7/8/108

[94] J. Y. Kim and J. G. Hong, "Effect of electrical conductivity on atomization characteristics of electrospray," *Journal of Applied Fluid Mechanics*, vol. 15, no. 5, pp. 1427–1436, 2022. [Online]. Available: https://www.jafmonline.net/article_2077.html

[95] N. Sochorakis, J. Grifoll, and J. Rosell-Llompart, "Scaling up of extractor-free electrosprays in linear arrays," *Chemical Engineering Science*, vol. 195, pp. 281–298, 2019. [Online]. Available: https://www.sciencedirect.com/science/article/pii/S0009250918306468

[96] J. Du, F. Fang, C. Pain, I. Navon, J. Zhu, and D. Ham, "Pod reduced-order unstructured mesh modeling applied to 2d and 3d fluid flow," *Computers Mathematics with Applications*, vol. 65, no. 3, pp. 362–379, 2013, efficient Numerical Methods for Scientific Applications. [Online]. Available: https://www.sciencedirect.com/science/article/pii/S0898122112004397

[97] D. J. Lucia, P. S. Beran, and W. A. Silva, "Reduced-order modeling: new approaches for computational physics," *Progress in Aerospace Sciences*, vol. 40, no. 1, pp. 51–117, 2004. [Online]. Available: https://www.sciencedirect.com/science/article/pii/S0376042103001131

[98] P. Astrid, S. Weiland, K. Willcox, and T. Backx, "Missing point estimation in models described by proper orthogonal decomposition," *IEEE Transactions on Automatic Control*, vol. 53, no. 10, pp. 2237–2251, 2008.

[99] G. Aversano, A. Bellemans, Z. Li, A. Coussement, O. Gicquel, and A. Parente, "Application of reduced-order models based on pca kriging for the development of digital twins of reacting flow applications," *Computers Chemical Engineering*, vol. 121, pp. 422–441, 2019. [Online]. Available: https://www.sciencedirect.com/science/article/pii/S0098135418305891